Oxygen Exchange Kinetics of the Potential Solid Oxide Fuel Cell Cathode Material (Bi,Sr)(Co,Fe)O$_{3-\delta}$

Von der Fakultät Chemie der Universität Stuttgart
zur Erlangung der Würde eines
Doktors der Naturwissenschaften (Dr. rer. nat.)
genehmigte Abhandlung

Vorgelegt von
Anja Wedig
aus Stuttgart

Hauptberichter: Prof. Dr. J. Maier
Mitberichter: Prof. Dr. J. Bill
Prüfungsvorsitzender: Prof. Dr. J. van Slageren
Tag der mündlichen Prüfung: 14. Mai 2013

Max-Planck-Institut für Festkörperforschung
Stuttgart
2013

Table of Contents

Abbreviations and Symbols

List of Abbreviations

ASR	area-specific resistance
BaSCF	$(Ba,Sr)(Co,Fe)O_{3-\delta}$
BiSCF	$(Bi,Sr)(Co,Fe)O_{3-\delta}$
CGO	Gd-doped CeO_2
DESY	Deutsches Elektronen-Synchrotron
DSC	differential scanning calorimetry
EDX	energy-dispersive X-ray spectroscopy
EIS	electrochemical impedance spectroscopy
ESRF	European Synchrotron Radiation Facility
EXAFS	extended X-ray absorption fine structure
FEM	finite element method
FIB	focused ion beam
FRM	Forschungs-Reaktor München
GI	grazing-incidence
ICP-OES	inductively-coupled plasma optical emission spectroscopy
LSCF	$(La,Sr)(Co,Fe)O_{3-\delta}$
LSM	$(La,Sr)MnO_{3\pm\delta}$
PLD	pulsed laser deposition
rds	rate-determining step
ScSZ	Sc_2O_3-doped ZrO_2
SEM	scanning electron microscopy
SIMS	secondary-ion mass spectrometry
SOFC	solid oxide fuel cell
SPS	spark plasma sintering
TEC	thermochemical expansion coefficient
TEM	transmission electron microscopy

TG	thermogravimetric
XPS	X-ray photoelectron spectroscopy
XRD	X-ray diffraction
YSZ	Y_2O_3-doped ZrO_2

List of Symbols

a	activity
a^0	standard activity
c_{ion}	concentration of ionic defects
c_O	concentration of lattice oxygen
$c_{V_O^{\cdot\cdot}}$	concentration of oxygen vacancies
C	electrical capacitance
C_{IF}	intermediate-frequency electrical capacitance
C_{LF}	low-frequency electrical capacitance
C^δ	chemical capacitance
d_{el}	electrode diameter
$D_{V_O^{\cdot\cdot}}$	oxygen vacancy diffusion coefficient
D^δ	chemical diffusion coefficient
D^*	oxygen tracer diffusion coefficient
e	elementary charge
E_a	(formal) activation energy
f	correlation factor
F	Faraday constant
ΔH_{ox}^0	standard oxidation enthalpy
i	total current density
I_d	depolarization current
$I_f(hkl)$	intensity of the (hkl) film diffraction peak
I_p	polarization current
$I_p(110)$	intensity of the (110) powder diffraction peak
$I_{p,inf}$	steady-state polarization current
$I_r(hkl)$	relative intensity of the (hkl) diffraction peak

$\vec{k}$	rate constant of the forward reaction
$\overleftarrow{k}$	rate constant of the backward reaction
k_B	Boltzmann constant
k^q	effective rate constant of the surface oxygen exchange reaction from electrical experiment
k^δ	effective rate constant of the surface oxygen exchange reaction from chemical experiment
k^*	effective rate constant of the surface oxygen exchange reaction from isotope exchange experiment
L	sample length
$p(O_2)$	oxygen partial pressure
$p^0(O_2)$	standard oxygen partial pressure
Q	constant phase element
Q_{IF}	intermediate-frequency constant phase element
Q_{LF}	low-frequency constant phase element
r_{YSZ}	radius of the YSZ cylinder
R	gas constant or electrical resistance
$\vec{\Re}$	reaction rate of the forward reaction
$\overleftarrow{\Re}$	reaction rate of the backward reaction
R_{HF}	high-frequency electrical resistance
R_{IF}	intermediate-frequency electrical resistance
R_{ion}	ion transport resistance of BiSCF
R_{LF}	low-frequency electrical resistance
R_s	electrical resistance of the surface oxygen exchange reaction
R_{ScSZ}	electrical resistance of ScSZ
$\Re_0$	equilibrium exchange rate
$\vec{\Re}_0$	equilibrium reaction rate of the forward reaction
$\overleftarrow{\Re}_0$	equilibrium reaction rate of the backward reaction
t	time
t_{eon}	electronic transference number
T	temperature

T_C	Curie temperature
T_N	Néel temperature
U	applied voltage
$V(hkl)$	volume fraction of the (hkl) crystal orientation
V_m	molar volume
z	charge number
z_{ion}	charge number of ionic defects
δ	oxygen nonstoichiometry
φ	electrical potential
$\tilde{\mu}$	electrochemical potential
$\tilde{\mu}_{eon}$	electrochemical potential of electrons
$\tilde{\mu}_{ion}$	electrochemical potential of ionic defects
μ_O	chemical potential of oxygen
μ^0	standard chemical potential
μ_O^0	standard chemical potential of oxygen
σ_{el}	electrical conductivity
σ_{eon}	electronic conductivity
σ_{ion}	ionic conductivity
σ_{YSZ}	ionic conductivity of YSZ
τ	relaxation time
ω_O	thermodynamic factor of oxygen

Zusammenfassung

Die vorliegende Arbeit befasst sich mit der Untersuchung der Kinetik des Sauerstoffaustauschs an gemischtleitenden Perowskiten der Zusammensetzung (Bi,Sr)(Co,Fe)$O_{3-\delta}$ (BiSCF) als potentiellen Kathodenmaterialien für Festoxidbrennstoffzellen (SOFCs). Die an der Oberfläche gemischtleitender Oxide ablaufende Sauerstoffaustauschreaktion ist nicht nur auf Grund ihrer technologischen Relevanz in SOFCs und einer Reihe weiterer (elektro)chemischer Anwendungen von Interesse. Vielmehr stellt sie einen grundlegenden Äquilibrierungsprozess von Festkörper und Gasphase dar, der oft eine Vielzahl an Eigenschaften fester Oxide bestimmt. Damit bietet sich die Sauerstoffaustauschreaktion in besonderem Maße als Modellreaktion zur Untersuchung des Mechanismus einer heterogenen katalytischen Reaktion zwischen Festkörper und Gasphase an. Wie in vorhergehenden Studien an Perowskiten mit gemischtvalenten Übergangsmetallkationen auf dem Perowskit-B-Platz (d. h. mit ausreichend hoher Konzentration an elektronischen Ladungsträgern) bewiesen, sind sowohl eine hohe Sauerstoffleerstellenkonzentration als auch eine hohe Sauerstoffleerstellenbeweglichkeit von Vorteil für eine schnelle Sauerstoffaustauschkinetik. Daher wurden als Untersuchungsgegenstand Bi-haltige Perowskite gewählt, für die eine hohe Beweglichkeit der Sauerstoffleerstellen zu erwarten ist auf Grund der hohen Polarisierbarkeit des Bi^{3+}-Kations. Weiterhin ist davon auszugehen, dass BiSCF-Perowskite eine geringere Neigung zur Carbonatbildung sowie zu strukturellen Phasenumwandlungen besitzen, die die Anwendbarkeit insbesondere von Ba-haltigen Perowskiten in SOFCs einschränken.

Eine Reihe repräsentativer BiSCF-Zusammensetzungen zumeist mit kubischer Perowskitstruktur wurde hergestellt. Während sich die Herstellung der phasenreinen Co-freien Zusammensetzungen als unkompliziert erwies, stellte sich die Synthese von Co-haltigen Perowskiten (z. B. zwei neuartigen Zusammensetzungen mit gemischter Co/Fe-Besetzung auf dem Perowskit-B-Platz) als schwieriger heraus möglicherweise auf Grund von Niedrigtemperaturphasenübergängen. Als Grundlage für die kinetischen Untersuchungen wurden zahlreiche Volumeneigenschaften insbesondere an den phasenreinen Co-freien Zusammensetzungen untersucht. Es wurde festgestellt, dass $Bi_{1-x}Sr_xFeO_{3-\delta}$ (x = 0.2, 0.5 und 0.8) gegenüber Y_2O_3-dotiertem ZrO_2 (YSZ) bis mindestens 800°C stabil ist, was auf eine höhere Kompatibilität mit dem gängigen SOFC-Elektrolyten hindeutet, als sie für (La,Sr)(Co,Fe)$O_{3-\delta}$ (LSCF) und (Ba,Sr)(Co,Fe)$O_{3-\delta}$ (BaSCF) beobachtet wurde. Cohaltiges BiSCF hingegen ging bereits bei 750°C eine Reaktion mit YSZ ein, was eine eher geringe chemische Stabilität nahelegt. Cerimetrische Titrationen der Pulver ergaben, dass Eisen in $Bi_{0.8}Sr_{0.2}FeO_{3-\delta}$ und $Bi_{0.5}Sr_{0.5}FeO_{3-\delta}$ beinahe ausschließlich die Oxidationszahl 3+ aufweist, während $Bi_{0.2}Sr_{0.8}FeO_{3-\delta}$ etwa 40% Fe^{4+} enthält. Die

hohe Konzentration an Fe^{3+} impliziert eine hohe Sauerstoffnichtstöchiometrie δ, die eine hohe ionische Leitfähigkeit erwarten lässt. Mittels thermogravimetrischer (TG-) Messungen wurde bewiesen, dass die Sauerstoffnichtstöchiometrie der beiden Zusammensetzungen mit geringerem Sr-Gehalt nahezu konstant bleibt beim Erhitzen bei unterschiedlichen Sauerstoffpartialdrücken, wohingegen für $Bi_{0.2}Sr_{0.8}FeO_{3-\delta}$ eine stärkere Variation von δ beobachtet wurde. TG-Analysen lieferten weiterhin Nachweise für eine vernachlässigbare Aufnahme von CO_2 durch Co-freies BiSCF, was auf eine geringe Tendenz zur Carbonatbildung hindeutet.

Mittels dynamischer Differenzkalorimetrie (DSC) wurde festgestellt, dass die temperaturunabhängige Oxidationsenthalpie von $Bi_{1-x}Sr_xFeO_{3-\delta}$ (x = 0.2, 0.5 und 0.8) mit zunehmendem Sr-Gehalt zunehmend negativ wird, aber in den meisten Fällen einen niedrigeren Absolutwert aufweist als diejenige der $(La,Ba,Sr)(Mn,Co,Fe)O_{3-\delta}$-Perowskite. Diese Beobachtung steht im Einklang mit den hohen δ-Werten aus TG-Messungen und legt eine geringe Bedeckung der Perowskitoberfläche mit adsorbierten Sauerstoffspezies nahe, da die Adsorptionsenthalpie proportional zur Oxidationsenthalpie ist. Die elektrische Leitfähigkeit im Bereich von 1-14 S cm^{-1} bei 750°C und einem $p(O_2)$ von 0.2 bar gemessen an gesinterten Keramiken und/oder Dünnfilmproben von BiSCF wies zumeist halbleiterartiges Verhalten auf mit Aktivierungsenergien von bis zu 0.45 eV für $Bi_{0.8}Sr_{0.2}FeO_{3-\delta}$ und ein Anstieg der Leitfähigkeit mit zunehmendem Sr- beziehungsweise Co-Gehalt wurde beobachtet. Die elektrische Leitfähigkeit Bi-haltiger Perowskite erwies sich zumeist als niedriger als diejenige der entsprechenden LSCF- und BaSCF-Zusammensetzungen wahrscheinlich auf Grund der niedrigen elektronischen Defektkonzentrationen und lokaler Gitterverzerrungen, die anhand von Messungen der erweiterten Röntgenabsorptionsfeinstruktur (EXAFS) nachgewiesen wurden. Wie $p(O_2)$-abhängige Messungen der elektrischen Leitfähigkeit ergaben, sind $Bi_{1-x}Sr_xFeO_{3-\delta}$-Perowskite Löcherleiter unter oxidierenden Bedingungen, und ein bei niedrigeren Sauerstoffpartialdrücken erreichtes Leitfähigkeitsplateau erlaubt die Bestimmung der ionischen Leitfähigkeit dieser Materialien. Messungen der thermochemischen Expansion zeigten, dass $Bi_{0.2}Sr_{0.8}FeO_{3-\delta}$ beim Erhitzen einer ähnlich starken Ausdehnung unterliegt wie (Ba-haltiges) Strontiumferrit, während für $Bi_{0.5}Sr_{0.5}FeO_{3-\delta}$ ein niedrigerer mittlerer thermochemischer Expansionskoeffizient (TEC) von beispielsweise 14×10^{-6} K^{-1} bei 750°C erhalten wurde vergleichbar demjenigen des La-haltigen Ferrits und gängiger Elektrolyte, was diese Zusammensetzung für Anwendungen in SOFCs eher geeignet erscheinen lässt.

Zur Untersuchung der Sauerstoffaustauschkinetik wurden porenfreie Dünnfilmmikroelektroden hergestellt. Im Gegensatz zu den üblicherweise in SOFCs verwendeten porösen Dickfilmelektroden besitzen sie eine klar definierte Morphologie, die detaillierte mechanistische Untersuchungen ohne eine Beeinflussung durch morphologische Effekte erlaubt. Für die Mikroelektrodenherstellung wurden typischerweise 150 nm dünne BiSCF-Filme mittels Laserstrahlverdampfens (PLD) auf (100)-orientierten YSZ-Einkristallsubstraten abgeschieden. Die erhalte-

nen Filme waren zumeist polykristallin gemäß Röntgenbeugung (XRD) mit Kristallorientierungsverteilungen, die nicht nur von der Gitterfehlanpassung von Film und Substrat, sondern auch von den jeweiligen Abscheidungsbedingungen (z. B. dem Hintergrundsauerstoffdruck und der Laserfluenz) abhingen. Untersuchungen mittels Rasterelektronenmikroskopie (SEM) und Transmissionselektronenmikroskopie (TEM) ergaben, dass die Filme trotz hoher Oberflächenrauigkeit im Filminneren porenfrei waren. Quantitative Analysen unter Verwendung von optischer Emissionsspektroskopie mit induktiv gekoppeltem Plasma (ICP-OES), energiedispersiver Röntgenspektroskopie (EDX) und Röntgenphotoelektronenspektroskopie (XPS) lieferten nahezu stöchiometrische Kationenzusammensetzungen für den gesamten Film und die Filmoberfläche, was darauf hindeutet, dass während der Filmabscheidung kein signifikanter Verlust an Bi stattfand. Für Untersuchungen unter Einsatz der elektrochemischen Impedanzspektroskopie (EIS) wurden die BiSCF-Filme mittels Fotolithographie und Inertgasionenstrahlätzens in ein Array runder Mikroelektroden strukturiert. Dies ermöglicht insbesondere die zuverlässige Unterscheidung von Prozessen, die an der Dreiphasengrenze beziehungsweise an der Elektrodenoberfläche ablaufen.

Anhand von EIS-Untersuchungen an BiSCF-Mikroelektroden wurde ein Oberflächenwiderstand der Sauerstoffaustauschreaktion erhalten, der höher als derjenige von BaSCF und niedriger als derjenige von LSCF ist (z. B. 3.5 Ω cm^2 für Bi$_{0.5}$Sr$_{0.5}$FeO$_{3-\delta}$ versus 1.1 Ω cm^2 für Ba$_{0.5}$Sr$_{0.5}$FeO$_{3-\delta}$ und 8.0 Ω cm^2 für La$_{0.6}$Sr$_{0.4}$FeO$_{3-\delta}$ bei 750°C und einem $p(O_2)$ von 0.2 bar) sowie mit zunehmendem Sr- und Co-Gehalt abnimmt. Zusätzlich zu dem dominierenden Halbkreis, der sich der Oberflächenreaktion zuordnen ließ, wurde in den Impedanzspektren ein zweiter Halbkreis beobachtet. Unter Anwendung des zweidimensionalen numerischen Modells von Lynch et al. konnten dieser zweite Halbkreis sowie der erhöhte Hochfrequenzachsenabschnitt auf eine signifikante Beeinflussung der Mikroelektrodenimpedanz durch einen hohen Flächenwiderstand zurückgeführt werden. Der hohe Flächenwiderstand resultiert aus der außergewöhnlich niedrigen elektronischen Leitfähigkeit der BiSCF-Perowskite, übte aber in den betrachteten Fällen keinen wesentlichen Einfluss auf den Oberflächenwiderstand aus. Eine erhebliche Diskrepanz ergab sich jedoch zwischen den an gesinterten Keramiken und Mikroelektroden gemessenen chemischen Kapazitäten und den mittels Simulation bestimmten Werten, deren Ursache unklar blieb.

Die anhand von Mikroelektrodenmessungen erhaltenen Werte für den Oberflächenwiderstand wurden durch EIS-Messungen an makroskopischen Proben verifiziert, die aus zwei mittels PLD auf beiden Seiten eines YSZ-Einkristallsubstrats abgeschiedenen Elektrodenfilmen bestanden. Messungen der Elektrodendurchmesserabhängigkeit bestätigten die oben aufgeführte Interpretation der Mikroelektrodenimpedanzspektren. Aus temperaturabhängigen Messungen wurde eine große Differenz abgeleitet zwischen den Aktivierungsenergien des inversen Oberflächenwiderstandes von Mikroelektroden (2.1-2.4 eV) und makroskopischen Proben

(1.1-1.2 eV), wobei letztere den für poröse Elektroden erhaltenen Literaturwerten nahekommen. EIS-Messungen bei unterschiedlichem Sauerstoffpartialdruck zeigten, dass der Oberflächenwiderstand der Beziehung $R_s \propto (p(O_2))^{-n}$ gehorcht mit einem Exponenten n zumeist größer als 0.5, was mit einer Teilnahme molekularer Sauerstoffspezies am ratenbestimmenden Schritt konsistent ist. In Übereinstimmung mit dem für LSCF und BaSCF berichteten Verhalten wurde eine Abnahme des Oberflächenwiderstandes bei Anlegen einer moderaten anodischen oder kathodischen Gleichspannung detektiert. Zusätzliche EIS-Messungen wurden an modifizierten Mikroelektroden durchgeführt, aber eine katalytische Wirkung von Oberflächenstufen und -ecken oder Co_3O_4-Verunreinigungen konnte nicht eindeutig festgestellt werden.

Zur Untersuchung der Beziehung zwischen der Sauerstoffaustauschrate und der ionischen Leitfähigkeit als typischerweise wichtigem Materialparameter wurden elektrochemische Polarisationsmessungen an elektrochemischen Polarisationszellen in Dünnfilmform durchgeführt. Ein neuer Zellaufbau wurde entwickelt bestehend aus einem typischerweise 80-170 nm dünnen BiSCF-Film, der mittels PLD auf einem (100)-orientierten MgO-Einkristallsubstrat abgeschieden wurde, einer elektronenblockierenden Elektrode aus Sc_2O_3-dotiertem ZrO_2 (ScSZ), einer reversiblen Pt-Elektrode und einer Al_2O_3-Schicht zur Abdichtung gegenüber der Gasatmosphäre. Die ionischen Leitfähigkeiten und chemischen Diffusionskoeffizienten von BiSCF wurden durch eine Kombination aus DC- und EIS-Messungen bestimmt. Eine gute Übereinstimmung wurde festgestellt zwischen der in dieser Studie erhaltenen ionischen Leitfähigkeit von $SrFeO_{3-\delta}$ und den in der Literatur angegebenen Werten. Weiterhin wurde sowohl an Dünnfilmen als auch an Pelletproben ein mit dem Einbau von Bi und eventuell Co einhergehender Anstieg der ionischen Leitfähigkeit beobachtet. Angesichts der Ergebnisse der TG-Messungen kann dies nicht mit einem Anstieg der Sauerstoffleerstellenkonzentration, sondern vielmehr mit einem Anstieg der Sauerstoffleerstellenbeweglichkeit (die proportional zum Sauerstoffleerstellendiffusionskoeffizienten ist) mit zunehmendem Bi- und Co-Gehalt erklärt werden. Eine signifikante Beeinflussung der Aktivierungsenergien der ionischen Leitfähigkeit und der Diffusionskoeffizienten durch Degradation wurde bemerkt. Gemäß den Erwartungen wiesen die Ergebnisse der elektrochemischen Polarisationsmessungen in den meisten Fällen keine starke Abhängigkeit vom Sauerstoffpartialdruck auf.

Folgende Schlüsse lassen sich anhand der Volumeneigenschaften, der aus Mikroelektroden-EIS-Messungen erhaltenen Oberflächenwiderstände des Sauerstoffaustauschs und der ionischen Leitfähigkeiten aus elektrochemischen Polarisationsmessungen an Dünnfilmen ziehen: Die Ersetzung von La^{3+} durch Bi^{3+} führt zu einer signifikanten Verbesserung der Sauerstoffaustauschkinetik, wenn auch die exzellente Performance der Ba-haltigen Perowskite nicht erreicht werden konnte. Die Ratenkonstante des Sauerstoffaustauschs steigt mit zunehmender elektronischer Leitfähigkeit linear an, entweder auf Grund der Teilnahme von adsorbiertem

Superoxid am ratenbestimmenden Schritt oder infolge eines sekundären Effekts wie dem gleichzeitigen Anstieg des Sr- oder Co-Gehalts. Die Ratenkonstante des Sauerstoffaustauschs weist keine klare Abhängigkeit von der Oxidationsenthalpie auf, da die Variation der Oxidationsenthalpie innerhalb der BiSCF-Materialklasse eher gering ist. Weiterhin geht die Zunahme der ionischen Leitfähigkeit offensichtlich mit einem linearen Anstieg der Ratenkonstante des Sauerstoffaustauschs einher ähnlich dem zuvor für BaSCF-Perowskite beobachteten Verhalten, was auf eine wichtige Rolle der Sauerstoffleerstellendiffusion bei der Oberflächen-Sauerstoffaustauschreaktion hindeutet. Schließlich machen, abgesehen von der niedrigen elektronischen Leitfähigkeit und eventueller Bi-Verdampfung, eine Vielzahl von günstigen Eigenschaften wie die hohe katalytische Aktivität, die hohe chemische und strukturelle Stabilität und die günstigen thermochemischen Expansionseigenschaften insbesondere Co-freie BiSCF-Perowskite zu vielversprechenden Kandidaten für Anwendungen als SOFC-Kathodenmaterialien.

Summary

The present study deals with the investigation of the kinetics of oxygen exchange on mixed-conducting (Bi,Sr)(Co,Fe)$O_{3-\delta}$ (BiSCF) perovskites as potential solid oxide fuel cell (SOFC) cathode materials. The oxygen exchange reaction on the surface of mixed-conducting oxides is not only of interest because of its technological relevance in SOFCs and a number of other (electro)chemical devices. Moreover, it represents a basic equilibration process between solid and gas phase often determining a variety of properties of solid oxides. Thus, the oxygen exchange reaction constitutes a highly attractive model reaction to approach a fundamental understanding of the mechanism of a heterogeneous catalytic reaction involving solid and gas phase. As proven in previous studies on perovskites with mixed-valence transition metal cations on the perovskite B site (i.e., with sufficiently high electronic charge carrier concentrations), both a high oxygen vacancy concentration and a high mobility of oxygen vacancies are beneficial for fast oxygen exchange kinetics. Therefore, Bi-containing perovskites were chosen as object of study, which are expected to exhibit a high mobility of oxygen vacancies due to the high polarizability of Bi^{3+}. Furthermore, BiSCF perovskites are supposed to be less prone to the formation of carbonates and structural phase transformations limiting the applicability in particular of Ba-containing perovskites in SOFCs.

A number of representative BiSCF compositions mostly with cubic perovskite structure were prepared. Whereas the preparation of the phase-pure Co-free compositions proved straightforward, the synthesis of Co-containing perovskites (e.g., two novel compositions with mixed Co/Fe occupation on the perovskite B site) turned out to be more challenging possibly due to low-temperature phase transitions. As a basis for the kinetic investigations, numerous bulk properties were studied in particular on the phase-pure Co-free compositions. $Bi_{1-x}Sr_xFeO_{3-\delta}$ (x = 0.2, 0.5, and 0.8) was found to be stable towards Y_2O_3-doped ZrO_2 (YSZ) until at least 800°C indicating a compatibility with the common SOFC electrolyte higher than that of (La,Sr)(Co,Fe)$O_{3-\delta}$ (LSCF) and (Ba,Sr)(Co,Fe)$O_{3-\delta}$ (BaSCF). Co-containing BiSCF, in contrast, underwent a reaction with YSZ already at 750°C suggesting a rather poor chemical stability. Cerimetric titrations on as-prepared powders revealed iron to exhibit almost exclusively the oxidation state 3+ in $Bi_{0.8}Sr_{0.2}FeO_{3-\delta}$ and $Bi_{0.5}Sr_{0.5}FeO_{3-\delta}$ whereas about 40% of Fe^{4+} is contained in $Bi_{0.2}Sr_{0.8}FeO_{3-\delta}$. The high concentration of Fe^{3+} implies a high oxygen nonstoichiometry δ expected to ensure a high ionic conductivity. Thermogravimetric (TG) measurements proved the oxygen nonstoichiometry to remain nearly constant upon heating at various oxygen partial pressures for the two compositions with lower Sr content, but a stronger variation of δ was

observed for $Bi_{0.2}Sr_{0.8}FeO_{3-\delta}$ TG analyses also yielded evidence for a negligible uptake of CO_2 by Co-free BiSCF indicative of a low tendency towards carbonate formation.

The temperature-independent oxidation enthalpy of $Bi_{1-x}Sr_xFeO_{3-\delta}$ (x = 0.2, 0.5, and 0.8) derived from differential scanning calorimetry (DSC) was found to become increasingly negative with increasing Sr content, but in most cases exhibit an absolute value lower than that of $(La,Ba,Sr)(Mn,Co,Fe)O_{3-\delta}$ perovskites. This observation is in line with the high δ values from TG measurements and suggests a low coverage of the perovskite surface with adsorbed oxygen species, since the adsorption enthalpy is proportional to the oxidation enthalpy. The electrical conductivity in the range of 1-14 S cm^{-1} at 750°C and a $p(O_2)$ of 0.2 bar measured on bulk and/or thin-film samples of BiSCF displayed mostly semiconductor-like behavior with activation energies of up to 0.45 eV for $Bi_{0.8}Sr_{0.2}FeO_{3-\delta}$ and was observed to increases with increasing Sr and Co content, respectively. The electrical conductivity of Bi-containing perovskites proved to be mostly lower than that of the corresponding LSCF and BaSCF compositions probably due to the low electronic defect concentrations and local lattice distortions evidenced by extended X-ray absorption fine structure (EXAFS) measurements. As revealed by $p(O_2)$-dependent measurements of the electrical conductivity, $Bi_{1-x}Sr_xFeO_{3-\delta}$ perovskites are p-type conductors under oxidizing conditions, and a conductivity plateau reached at lower oxygen partial pressures allows for the determination of the ionic conductivity of these materials. Thermochemical expansion measurements showed $Bi_{0.2}Sr_{0.8}FeO_{3-\delta}$ to undergo similarly strong expansion upon heating as (Ba-containing) strontium ferrite, whereas for $Bi_{0.5}Sr_{0.5}FeO_{3-\delta}$ a lower mean thermochemical expansion coefficient (TEC) of, for example, 14×10^{-6} K^{-1} at 750°C was obtained comparable to that of the La-containing ferrite and common electrolytes making this composition more suitable for applications in SOFCs.

To investigate the oxygen exchange kinetics, dense thin-film microelectrodes were prepared. As opposed to the porous thick film electrodes commonly used in SOFCs, they possess a well-defined morphology allowing for detailed mechanistic investigations without interference by morphological effects. For microelectrode preparation, typically 150 nm thin films of BiSCF were deposited by pulsed laser deposition (PLD) onto (100)-oriented YSZ single crystal substrates. The obtained films were mostly polycrystalline according to X-ray diffraction (XRD) with crystal orientation distributions depending not only on the lattice mismatch between film and substrate, but also on the applied deposition conditions (e.g., the background oxygen pressure and laser fluence). Scanning electron microscopy (SEM) and transmission electron microscopy (TEM) revealed the films to be dense throughout the film thickness despite a high surface roughness. Quantitative analyses by means of inductively-coupled plasma optical emission spectroscopy (ICP-OES), energy-dispersive X-ray spectroscopy (EDX), and X-ray photoelectron spectroscopy (XPS) yielded nearly stoichiometric cation compositions in the bulk

of the films and on the film surface indicating no significant loss of Bi during the film deposition. For investigations via electrochemical impedance spectroscopy (EIS), the BiSCF films were structured into arrays of circular microelectrodes using photolithography and inert gas ion beam etching. This in particular enables the reliable distinction of processes occurring at the three-phase boundary and on the electrode surface, respectively.

From EIS investigations on BiSCF microelectrodes, a surface resistance of the oxygen exchange reaction was obtained higher than that of BaSCF and lower than that of LSCF (e.g., 3.5 Ω cm^2 for $Bi_{0.5}Sr_{0.5}FeO_{3-\delta}$ versus 1.1 Ω cm^2 for $Ba_{0.5}Sr_{0.5}FeO_{3-\delta}$ and 8.0 Ω cm^2 for $La_{0.6}Sr_{0.4}FeO_{3-\delta}$ at 750°C and a $p(O_2)$ of 0.2 bar), and decreasing with increasing Sr and Co content. In addition to the dominating semicircle attributable to the surface reaction, a second semicircle was observed in the impedance spectra. Applying the 2D numerical model of Lynch et al., this second semicircle as well as the increased high-frequency axis intercept could be ascribed to a significant impact of high sheet resistance on the microelectrode impedance. The high sheet resistance results from the exceptionally low electronic conductivity of BiSCF perovskites, but was not found to exert a substantial influence on the surface resistance in the considered cases. A considerable discrepancy was, however, revealed between the chemical capacitances from bulk samples, microelectrodes, and simulations, the reason of which remained unclear.

The surface resistance values from microelectrode measurements were verified by EIS measurements on macroscopic samples consisting of two electrode films deposited by PLD onto both sides of a YSZ single crystal substrate. Electrode-diameter-dependent measurements confirmed the interpretation of microelectrode impedance spectra provided above. From temperature-dependent measurements, a large difference was derived between the activation energies of the inverse surface resistance from microelectrodes (2.1-2.4 eV) and macroscopic samples (1.1-1.2 eV) the latter being close to literature values obtained on porous electrodes. EIS measurements at varying oxygen partial pressure showed the surface resistance to obey $R_s \propto (p(O_2))^{-n}$ with an exponent n mostly larger than 0.5, which is consistent with molecular oxygen species being involved in the rate-determining step. In accordance with the behavior reported for LSCF and BaSCF, a decrease in the surface resistance was detected upon application of a moderate anodic or cathodic bias. Additional EIS measurements were performed on modified microelectrodes, but the catalytic impact of surface steps and kinks or Co_3O_4 impurities could not be definitely clarified.

To study the interrelation between the oxygen exchange rate and the ionic conductivity as typically important material parameter, electrochemical polarization measurements were conducted on thin-film electrochemical polarization cells. A new cell setup was developed consisting of a typically 80-170 nm thin BiSCF film deposited by PLD onto a (100)-oriented MgO single

crystal substrate, an electron-blocking Sc_2O_3-doped ZrO_2 (ScSZ) electrode, a reversible Pt electrode, and an Al_2O_3 layer as gas-tight sealing. The ionic conductivities and chemical diffusion coefficients of BiSCF were determined via a combination of DC and EIS measurements. Good agreement was found between the ionic conductivity of $SrFeO_{3-\delta}$ obtained in this study and the values reported in literature. The ionic conductivity from both thin films and pellet samples was observed to increase upon introduction of Bi and possibly Co. In view of the results from TG measurements, this can not be explained by an increase in the oxygen vacancy concentration, but rather be attributed to an increase in the oxygen vacancy mobility (which is proportional to the oxygen vacancy diffusion coefficient) with increasing Bi and Co content. A significant effect of degradation on the activation energies of the ionic conductivity and the diffusion coefficients was noticed. Finally, the results from electrochemical polarization measurements in most cases did not exhibit a strong dependence on the oxygen partial pressure in accordance with expectations.

From the obtained bulk properties, the surface oxygen exchange resistances from microelectrode EIS measurements, and the ionic conductivities from thin-film electrochemical polarization measurements, the following conclusions can be drawn: The substitution of La^{3+} by Bi^{3+} leads to a significant improvement of the oxygen exchange kinetics, although the excellent performance of Ba-containing perovskites could not be reached. The oxygen exchange rate constant increases linearly with increasing electronic conductivity, which is either due to adsorbed superoxide being involved in the rate-determining step or the consequence of a secondary effect such as the concomitant increase in the Sr or Co content. The oxygen exchange rate constant does not display a clear dependence on the oxidation enthalpy, as the variation of the oxidation enthalpy is rather small within the BiSCF material class. Furthermore, the increase in the ionic conductivity apparently coincides with a linear increase in the oxygen exchange rate constant similar to the behavior observed previously for BaSCF perovskites and suggestive of an important role of oxygen vacancy diffusion in the surface oxygen exchange reaction. Finally, apart from the low electronic conductivity and possible Bi evaporation, a variety of favorable properties such as the high catalytic activity, the high chemical and structural stability, and the favorable thermochemical expansion characteristics render in particular Co-free BiSCF perovskites promising candidates for applications as SOFC cathode materials.

1   Introduction

According to the decisions of the Federal Government,[1] the German energy supply system will be subjected to fundamental reorganization in the coming years. The fast depletion of resources and the release of environmentally harmful greenhouse gases during combustion necessitate significant reduction in the use of fossil fuels (coal, oil, and natural gas) as well as nuclear fuels as primary energy carriers. By 2050, these conventional fuels are intended to be largely substituted by renewable energy sources. Furthermore, the implementation of measures to increase energy efficiency is another key aim of the "Energiewende". Though at present it remains unclear whether the aspired goals can be fully achieved, one thing appears certain: To enable the successful reorganization of our energy system, the extensive investigation of all aspects of sustainable and efficient energy supply is indispensable. This includes not only the exploration of various methods of "energy generation" (the development of primary energy sources), energy transport, and energy storage, but also the investigation of systems which allow for a highly efficient conversion of different types of energy into one another.

One such device for the efficient conversion of energy is the fuel cell. A fuel cell directly converts the chemical energy of the fuel via electrochemical reaction into electrical energy. Since an intermediary conversion of chemical energy into thermal energy and, thereafter, mechanical energy (as in the case of the conventional methods of electricity generation) is not necessary, Carnot's limit does not apply to fuel cells and hence much higher efficiencies may be achieved. In its original form first constructed by Sir William Robert Grove in 1839,[2] a fuel cell uses continuously supplied gaseous hydrogen and oxygen for the electrochemical production of water combined with the generation of DC electricity and heat. In fuel cell systems operating at high temperatures and, therefore, capable of internal fuel reforming or the direct electrocatalytic oxidation of complex gases, also gaseous hydrocarbons and alcohols such as methanol might be utilized as fuels. Compared to the conventional ways of electricity production, fuel cells offer high efficiency particularly also in the low-power-output range or in partial-load operation, straightforward adjustment of the power output due to the modular construction mode, and low to virtually no emission of pollutants.

Classified by the sort of electrolyte applied (e.g., ion-permeable polymer foils, molten carbonate or oxide ceramics), different types of fuel cells are currently under investigation. Fuel cells consisting of an ion-conducting oxide ceramic membrane as electrolyte are typically referred to as solid oxide fuel cells (SOFCs). As they only operate at high temperatures, SOFCs are also denoted as high-temperature fuel cells. In today's technologically most relevant version of a SOFC,

the ionic species diffusing through the membrane are oxide ions. The oxide ions are created at the cathode side via electrochemical reduction of gaseous oxygen in the presence of an electrocatalytically active ceramic oxide (e.g., mixed ion-electron-conducting perovskites such as $(La,Sr)(Mn,Co,Fe)O_{3-\delta}$) according to

$$\tfrac{1}{2}O_2(gas)+2e^-(cathode) \rightleftharpoons O^{2-}(electrolyte) \qquad (1.1)$$

The formed oxide ions diffuse, driven by a gradient in the electrochemical potential, through the electrolyte membrane (for example, Y_2O_3-doped ZrO_2 (YSZ)) and react mostly with syngas from internal reforming of the H-containing fuel supplied at the anode side (e.g., a Ni/YSZ cermet) under formation of water and carbon dioxide following

$$H_2(gas)+CO(gas)+2O^{2-}(electrolyte) \rightleftharpoons H_2O(gas)+CO_2(gas)+4e^-(anode) \quad (1.2)$$
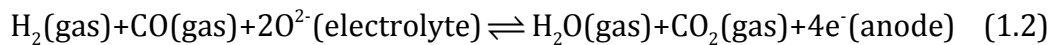
At the same time, a flow of electrons through the outer electrical circuit is generated, and a certain amount of heat is released. Unlike other types of fuel cells operated at lower temperatures, SOFCs exhibit a high tolerance towards CO and also sufficiently fast electrode kinetics to directly oxidize complex gases. Therefore, natural gas can directly be used as fuel without any further elaborate purification steps. SOFCs are in particular intended for the on-site cogeneration of heat and power on a small scale (1-5 kW electrical power output) and as auxiliary power units in motor vehicles running on the respective vehicle fuel.

As already mentioned, the transport and reaction processes occurring in a SOFC require thermal activation to proceed at a noticeable rate. For this reason, SOFCs are operated at temperatures as high as 800-1000°C. At these temperatures, however, undesired reactivity of the individual cell components towards each other is significantly increased. In addition, thermochemical expansion mismatch can cause cracks and sealing leaks upon (intended or unintended) thermal cycling further reducing the lifetime of the cell. Consequently, one main aim of current SOFC research lies in lowering the operating temperature to the intermediate range of 600-800°C. This makes a further optimization of the different components necessary. Regarding the electrolyte, ohmic losses might be lowered to a reasonable degree by reducing its thickness. The greater challenge resides in the reduction of polarization losses at the cathode, since the cathode reaction typically exhibits a higher activation energy than the electrolyte conductivity and anode reaction.[3-14] Here, also the application of new materials has to be taken under consideration, most ideally based on a profound understanding of the kinetics underlying the oxygen reduction reaction.

The catalytic reduction of gas-phase oxygen on the surface of a mixed-conducting solid oxide is a rather complex reaction the mechanism of which has to date not been elucidated unequivocally. A number of reaction steps need to be taken into account, and the reaction step proceeding at the lowest rate and, therefore, determining the overall reaction rate might be different for different materials. Interest in understanding the oxygen reduction mechanism has not only been triggered by its direct technological relevance in SOFCs and a number of other (electro)chemical devices (e.g., oxygen permeation membranes and resistive oxygen sensors). The exchange of oxygen with the surrounding gas atmosphere is a basic equilibration step every solid oxide undergoes to a varying degree at elevated temperature upon changing oxygen chemical potential. Elucidating the kinetics of oxygen exchange can hence be expected to lead to a better understanding of a variety of properties of solid oxides which are largely influenced by the process of equilibration and the resulting point defect concentrations.

The oxygen exchange kinetics of mixed-conducting SOFC cathode materials is preferably investigated for simplified model systems. In a conventional SOFC, the cathode material is deposited, for example, via screen printing to obtain a porous electrode morphology. Such a porous electrode morphology is favorable for applications since it provides a large three-phase boundary (the area where gas phase, electrode, and electrolyte are in direct contact with each other) representing the reactive region for certain electrode materials. For mechanistic investigations, however, dense electrodes are preferred. They possess a well-defined morphology, which is independent of the type of material or processing. To study the oxygen exchange reaction by an electrical experiment, the electrode material is, for instance, incorporated into an electrochemical cell. Electrochemical cells are most suitably fabricated in thin-film form if the focus of investigation lies on an interfacial process such as the surface reaction. In practice, thin-film electrodes are typically deposited onto electrolyte substrates by pulsed laser or sputter deposition, often followed by structuring of the electrode film into various shapes, for example, using photolithography.

Numerous studies on thin-film electrochemical cells of the most commonly used SOFC cathode materials, the mixed-conducting perovskites $(La,Sr)MnO_{3\pm\delta}$ (LSM) and $(La,Sr)(Co,Fe)O_{3-\delta}$ (LSCF) with mixed cation occupation on the perovskite A and/or B site, are reported in literature.[3-4, 7-8, 10-12, 15-45] The related composition $(Ba,Sr)(Co,Fe)O_{3-\delta}$ (BaSCF) has attracted much attention due to its, among perovskites, unsurpassed oxygen exchange kinetics.[14, 46-49] Detailed mechanistic investigations revealed that within the BaSCF solid solution series, not only a high oxygen vacancy concentration, but also a high mobility of oxygen vacancies are beneficial for fast oxygen exchange.[14] This implies that one important requirement on a potential SOFC cathode material is a high ionic conductivity (which is directly proportional to the product of oxygen vacancy concentration and

oxygen vacancy mobility). A high oxygen vacancy concentration is usually achieved by Sr^{2+} acceptor doping, whereas a high oxygen vacancy mobility can be provided by a highly polarizable A cation such as Ba^{2+}. The presence of Ba^{2+} is, however, considered responsible for many of the effects limiting the applicability of BaSCF in SOFCs (e.g., the detrimental structural transformation into a hexagonal perovskite phase between 850°C and 900°C[50-51] and the high reactivity towards common SOFC electrolytes[48, 52-53] and CO_2[54-55]). Perovskites accommodating Bi^{3+} on the A site have been proposed as novel SOFC cathode materials recently.[56] Bi^{3+}, highly polarizable owing to its 6s lone pair, is expected to offer a high mobility of oxygen vacancies. In addition, the low basicity of Bi^{3+} might help to avoid the stability problems observed for Ba-containing perovskites.

In this thesis, the oxygen exchange kinetics of several representative $(Bi,Sr)(Co,Fe)O_{3-\delta}$ (BiSCF) compositions was investigated. The investigations were conducted on morphologically well-defined thin-film model electrodes by means of electrochemical impedance spectroscopy (EIS). Alongside, a range of other methods was applied to further characterize the structural and transport properties of BiSCF which possibly influence the oxygen exchange performance. In particular, electrochemical polarization experiments were carried out to examine the supposed strong correlation between ionic conductivity and oxygen exchange rate. Thus, it was aimed to gain a deeper understanding of the mechanistic principles governing the oxygen exchange reaction on mixed-conducting perovskite-type oxides.

2 Theory

2.1 Surface Oxygen Exchange on Mixed-Conducting Oxides

When dealing with the reduction of oxygen on SOFC cathodes (equation (1.1)), two cases have to be distinguished: (i) In a conventional SOFC, the cathode consists of a porous layer of a (predominantly) electron-conducting material such as Pt or LSM, and the so-called "surface path" (Fig. 2.1, left-hand side) is the only possible or dominating way of oxygen reduction: The incorporation of (gaseous or adsorbed) oxygen species into the solid phase occurs at the three-phase boundary, where the respective species (and electrons) encounter oxygen vacancies provided by the electrolyte. (ii) In more recent versions of a SOFC, mixed-conducting transition metal oxides with considerable oxide ion conductivity are used as cathodes, and the "bulk path"[29] (Fig. 2.1, right-hand side) as alternative reduction pathway becomes significant: Oxygen is incorporated into the electrode on the whole electrode surface, transported through the bulk of the electrode, and finally incorporated into the electrolyte on a much larger area increasing the rate of the overall oxygen reduction. Typical (potential) electrode materials with considerable ionic conductivity favoring oxygen reduction via the bulk path are perovskite-type LSCF and BaSCF, but also BiSCF investigated in this study. Therefore, the focus of the current study lies on the investigation of oxygen reduction following the bulk path.
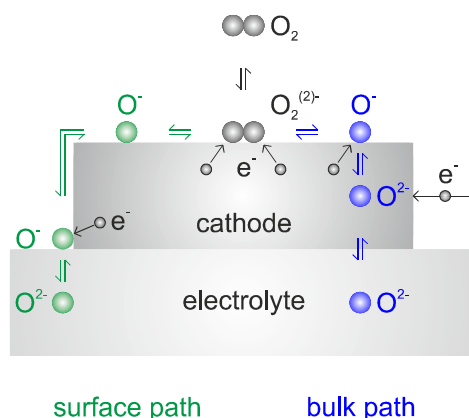

Fig. 2.1. Schematic depiction of two possible oxygen reduction pathways on SOFC cathodes: the surface path (left-hand side) and the bulk path (right-hand side).

Among the different processes involved in the bulk path, the exchange of oxygen on the electrode surface is of particular interest as it is typically slower than, for

example, the subsequent transport of oxide ions through the mixed conductor, and to date rather poorly understood. Based on the experimental findings and hypotheses presented in literature, the exchange of oxygen on the surface of a mixed-conducting oxide can be divided tentatively into a number of elementary steps according to the following scheme depicted in Kröger-Vink notation:[57]

$$O_2 + M_M^x \rightleftharpoons O_{2,ad}^- + M_M^\bullet \qquad (2.1)$$

$$O_{2,ad}^- + M_M^x \rightleftharpoons O_{2,ad}^{2-} + M_M^\bullet \qquad (2.2)$$

$$O_{2,ad}^{2-} \rightleftharpoons 2O_{ad}^- \qquad (2.3)$$

$$O_{ad}^- + V_O^{\bullet\bullet} \rightleftharpoons O_O^\bullet \qquad (2.4)$$

$$O_O^\bullet + M_M^x \rightleftharpoons O_O^x + M_M^\bullet \qquad (2.5)$$

(the subscript "ad" refers to "adsorbed"). Here, electronic defects are supposed to be localized on the transition metal M on the perovskite B site in accordance with small polaron hopping being the dominant conduction mechanism in most mixed-conducting perovskites in the relevant temperature and oxygen partial pressure range.[58-62] The scheme comprises the adsorption, dissociation, and incorporation of oxygen species as well as charge transfer steps from the solid oxide to the respective species. In order to create a starting point for any investigation of the actual oxygen exchange mechanism, it is commonly assumed that one of the above-mentioned steps is significantly slower than the other steps and hence determining the rate of the overall reaction.

To gather information about this rate-determining step (rds), attempts have been made to identify and quantify the oxygen species and crystal defects such as oxygen vacancies present on the electrode surface using in situ surface analytical techniques. However, up to date many of the available surface analytical tools are applied successfully only to systems under vacuum conditions, which are far apart from the conditions typically prevailing in a SOFC. A phenomenological approach to an elucidation of the rds consists in determining the effective rate constant of surface oxygen exchange. In fact, three different rate constants need to be distinguished depending on the applied experimental technique: k^q from electrical measurements, k^δ from chemical experiments, and k^* from isotope exchange experiments with

$$k^q \approx k^* \qquad (2.6)$$

and

$$k^{\delta} = \omega_0 k^* \tag{2.7}$$

($\omega_0 = (c_0/RT)(\partial\mu_0/\partial c_0) = (1/2)(\partial\ln p(O_2)/\partial\ln c_0)$, ω: thermodynamic factor, c: concentration, R: gas constant, T: temperature, μ: chemical potential, $p(O_2)$: oxygen partial pressure; the subscript "O" refers to regular oxide ions "O_O^x").[63] In the present study, k^q was calculated from the resistance of the surface oxygen exchange reaction R_s deduced via EIS measurements according to

$$k^q = \frac{k_B T}{4e^2 R_s c_O} \tag{2.8}$$

(k_B: Boltzmann constant, e: elementary charge).[64] The effective rate constant k^q is directly proportional to the equilibrium exchange rate $\Re_0$ of the surface reaction, that is,[63]

$$k^q \propto \Re_0 \tag{2.9}$$

$\Re_0$, in turn, is related to the reaction rates $\vec{\Re}$ and $\overleftarrow{\Re}$ of the forward and backward reaction and hence the rate constants $\vec{k}$ and $\overleftarrow{k}$ of the forward/backward reaction at equilibrium according to

$$\Re_0 = \sqrt{\vec{\Re}\overleftarrow{\Re}} = \sqrt{\vec{k}[\widehat{A}]^a[\widehat{B}]^b...\overleftarrow{k}[\widehat{U}]^u[\widehat{V}]^v} \tag{2.10}$$

where the (equilibrium) concentrations of the involved species A, ..., U, ... are denoted by square brackets (and arcs), and the reaction orders a, ..., u, ... depend on the rds.[63, 65] As evident from equation (2.9)-(2.10), the $p(O_2)$ dependence of k^q can provide information about the rds if the $p(O_2)$ dependence of the point defect concentrations is known.

For a wide range of mixed-conducting perovskites with considerable electronic conductivity σ_{eon}, the effective rate constant of surface oxygen exchange was found to increase with increasing ionic conductivity σ_{ion} (or oxygen tracer diffusivity $\propto \sigma_{ion}$) (Fig. 2.2).[14, 66-68] The correlation between the oxygen exchange rate constant and σ_{ion} is nearly perfectly linear within the series $SrFeO_{3-\delta}$ - $Ba_{0.5}Sr_{0.5}FeO_{3-\delta}$ -

$Ba_{0.5}Sr_{0.5}Co_{0.8}Fe_{0.2}O_{3-\delta}$ (Fig. 2.2b).[14] Within the group of $(Ln,Sr)(Mn,Co,Fe)O_{3-\delta}$ (Ln = La and Sm) perovskites, in contrast, a deviation from this straightforward behavior was observed (Fig. 2.2a)[66-68] and assigned to changes in the oxidation enthalpy altering not only the oxygen vacancy concentration, but also the chemisorption enthalpy and thus the concentration of adsorbed oxygen species on the oxide surface.[69] Based on these findings as well as quantum chemical calculations,[70-71] a model of the oxygen exchange mechanism was proposed:[68] For materials with a low concentration of surface oxygen vacancies (e.g., LSM), either the dissociation of adsorbed peroxide $O_{2,ad}^{2-}$ (without participation of an oxygen vacancy) or the approach of an oxygen vacancy to O_{ad}^- was suggested to be rate-determining. For materials with a high concentration of oxygen vacancies at the surface (e.g., LSCF and BaSCF), it might rather be the approach of an oxygen vacancy to $O_{2,ad}^{2-}$ which is determining the overall oxygen exchange rate. The proposed model is also in agreement with the strong $p(O_2)$ dependence of the oxygen exchange rate constant detected for LSCF[72] and BaSCF[14] (see also chapter 4.3.6).
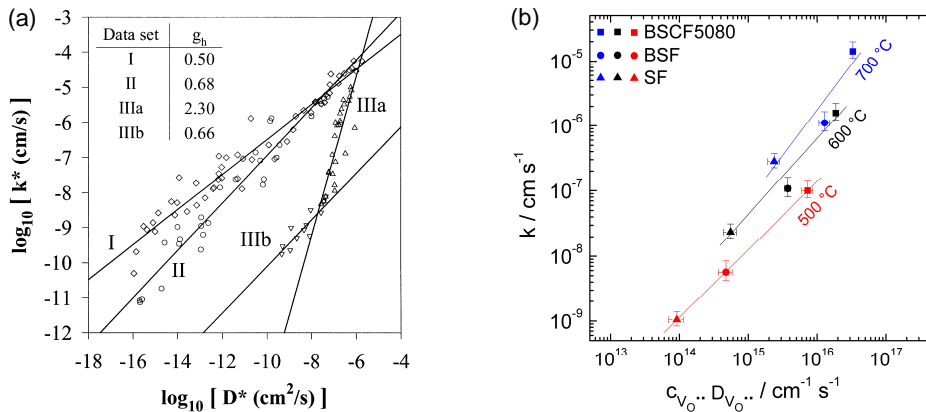

Fig. 2.2. (a) Effective surface oxygen exchange rate constants k^* measured on dense ceramics plotted versus the oxygen tracer diffusion coefficient for mixed-conducting (group I: $La_{1-x}Sr_xMn_{1-y}Co_yO_{3\pm\delta}$, $Sm_{1-x}Sr_xCoO_{3-\delta}$ and $La_{0.6}Sr_{0.4}Fe_{0.8}Co_{0.2}O_{3-\delta}$), mainly ion-conducting (group II: $CaZr_{0.9}In_{0.1}O_{2.95}$, $SrCe_{0.95}Yb_{0.05}O_{2.975}$, and $La_{1-x}Sr_xYO_{3-x/2}$), and almost exclusively ion-conducting (group IIIa: fluorite-type oxides at high temperature plus $La_{0.9}Sr_{0.1}Ga_{0.8}Mg_{0.2}O_{2.85}$ and group IIIb: fluorite-type oxides at low temperature) materials at $p(O_2) = 1$ bar. Graph taken from ref. [67]. (b) Effective surface oxygen exchange rate constants k^q measured on dense PLD films on YSZ plotted versus the product of bulk oxygen vacancy concentration and oxygen vacancy diffusion coefficient for $Ba_{0.5}Sr_{0.5}Co_{0.8}Fe_{0.2}O_{3-\delta}$ (BSCF5080), $Ba_{0.5}Sr_{0.5}FeO_{3-\delta}$ (BSF), and $SrFeO_{3-\delta}$ (SF) at $p(O_2) = 0.2\text{-}0.5$ bar and different temperatures. Graph taken from ref. [14].

The changes in the ionic conductivity and hence the changes in the oxygen exchange rate constant of $(La,Sr,Ba)(Mn,Co,Fe)O_{3-\delta}$ can be related to changes in the two factors determining the ionic conductivity (equation (2.16)): the concentration of oxygen vacancies $c_{V_O^{\bullet\bullet}}$ and their mobility assessed via the oxygen vacancy diffusion coefficient $D_{V_O^{\bullet\bullet}}$. As illustrated in Fig. 2.3, the increase in k^q from LSM to

LSCF can be attributed to an increase in the oxygen vacancy concentration, since the oxygen vacancy mobility stays nearly constant.[73-74] The increase in the oxygen exchange rate constant from LSCF to BaSCF as well as within the group of BaSCF perovskites, on the other hand, is caused not only by the (comparatively moderate) increase in the oxygen vacancy concentration, but also by an increase in the oxygen vacancy mobility[14] resulting mainly from the high polarizability of Ba^{2+} and Co^{2+}, respectively.[75] The recognition of the importance of both a high concentration and mobility of oxygen vacancies for fast oxygen exchange kinetics inspired the present investigation of Bi-containing perovskites expected to possess in particular also the desired high oxygen vacancy mobility.
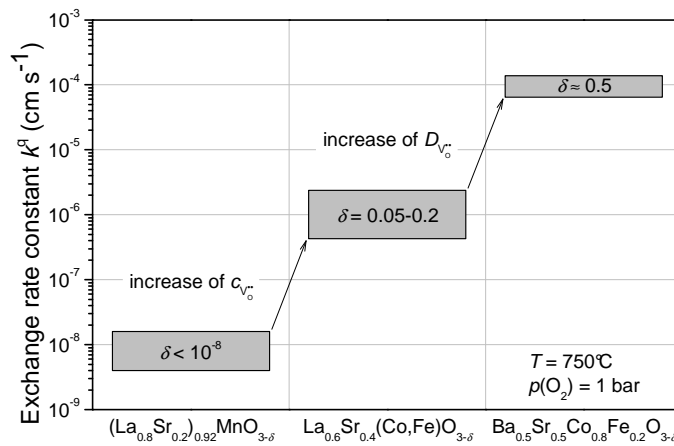

Fig. 2.3. Comparison of the effective surface oxygen exchange rate constants k^q of LSM,[11] LSCF,[10] and BaSCF[14] measured on dense PLD films on YSZ. After ref. [68].

2.2   Bulk Oxygen Transport in Mixed-Conducting Oxides

The partial ionic or partial electronic conductivity of a mixed-conducting material can be determined by an electrochemical polarization experiment using one or two electrodes selectively blocking the flux of one type of charge carrier. For example, to measure the partial ionic conductivity, the sample is placed between one or two electron-blocking electrodes (Fig. 2.4a). When a voltage is applied to this arrangement, the flux of electrons, generally driven by a gradient in the electrochemical potential, is suppressed at steady state yielding for the mixed conductor

$$\nabla \tilde{\mu}_{\text{eon}} = 0 \qquad\qquad (2.11)$$

($\tilde{\mu} = \mu^0 + RT\ln(a/a^0) + ze\varphi$: electrochemical potential, a: activity, z: charge number, φ: electrical potential; the subscript "eon" refers to "electron", and the superscript "0" denotes standard conditions). The total current density i is then given by the flux of ions following for dilute situations

$$i = -\frac{\sigma_{ion}}{z_{ion}F}\nabla\tilde{\mu}_{ion} = -\frac{\sigma_{ion}RT}{z_{ion}F}\nabla\ln c_{ion} - \frac{\sigma_{ion}e}{F}\nabla\varphi \qquad (2.12)$$

(F: Faraday constant; the subscript "ion" refers to "ionic defect"), where the relative contributions of the two terms on the right-hand side depend on the detailed defect chemistry of the material. In general, however, the blocking of the electronic charge carriers leads to the build-up of a stoichiometry polarization within the sample.
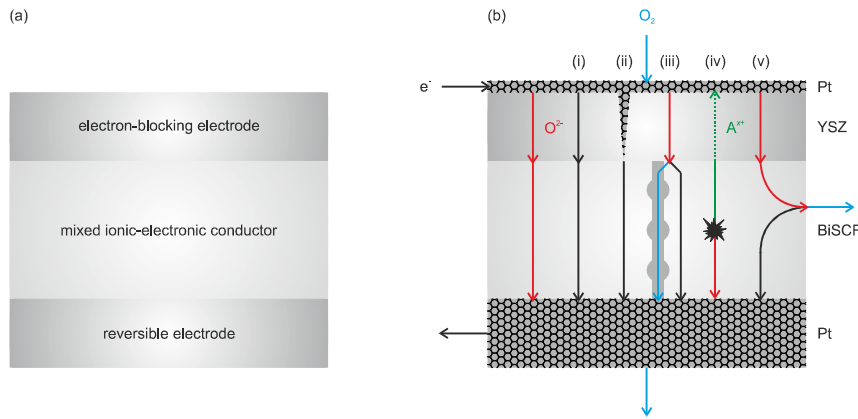

Fig. 2.4. (a) Schematic depiction of an electrochemical polarization cell. (b) Possible transport processes occurring in the cell upon application of a voltage. Red arrows indicate oxide ion transport, black arrows electron transport, blue arrows the transport of gaseous oxygen and the green arrow cation transport. The indices (i)-(v) refer to processes described in the text.

The time dependence of the polarization current I_p detected after a stepwise increase of the applied voltage is expressed at long times as[76]

$$I_p(t) = I_{p,inf} + const\exp\left(-\frac{t}{\tau}\right) \qquad (2.13)$$

(t: time, $I_{p,inf}$: steady-state polarization current, τ: relaxation time), and the time dependence of the depolarization current I_d measured after switching off the voltage is given at long times by

$$I_d(t) = const \exp\left(-\frac{t}{\tau}\right) \tag{2.14}$$

If the electrochemical polarization cell comprises one electron-blocking and one reversible electrode, the relaxation time of the mixed conductor depends on the chemical diffusion coefficient D^δ according to[77]

$$\tau = \frac{L^2}{\pi^2 D^\delta} \tag{2.15}$$

(L: sample length) assuming an electronic transference number t_{eon} close to 1 and negligible interfacial resistances; the relaxation time is four times smaller for a cell with two electron-blocking electrodes and four times larger if one electron-blocking and one ion-blocking electrode are used.[76]

As evident from equation (2.13), the ionic conductivity can be calculated from the polarization current at steady state, whereas D^δ is obtained from the slope of a plot of $\ln((I_p - I_{p,inf})/A)$ versus time and $\ln(I_d/A)$ versus time, respectively. The ionic conductivity of an oxide ion conductor is related to the oxygen vacancy diffusion coefficient via the Nernst-Einstein equation[78] yielding

$$\sigma_{ion} = \frac{4F^2 c_{V_O^{\cdot\cdot}} D_{V_O^{\cdot\cdot}}}{RT} \tag{2.16}$$

(T: temperature), and, for $\sigma_{eon} \gg \sigma_{ion}$, the chemical diffusion coefficient is coupled to $D_{V_O^{\cdot\cdot}}$ by the thermodynamic factor ω_0 according to[79]

$$D^\delta \approx \frac{\omega_0 c_{V_O^{\cdot\cdot}}}{c_O} D_{V_O^{\cdot\cdot}} \tag{2.17}$$

The oxygen vacancy diffusion coefficient, in turn, can be related to the oxygen tracer diffusion coefficient D^* using

$$D_{V_O^{\bullet\bullet}} = \frac{c_O}{fc_{V_O^{\bullet\bullet}}} D^*$$

(2.18)

(f: correlation factor, f = 0.69 for perovskite-type oxides[73]).[79]

In an electrochemical polarization experiment, a number of requirements have to be fulfilled in order to suppress possible parallel processes leading to erroneous results for the conductivity (Fig. 2.4b).[80] In case the ionic conductivity of a mixed electron-oxide-ion conductor is to be measured, the requirements are:

(i)   an electron transport resistance of the electron-blocking electrode significantly higher than the ion transport resistance of the mixed conductor,

(ii)   the absence of cracks in the electron-blocking electrode,

(iii) the absence of open pores in the mixed conductor,

(iv)   a decomposition voltage of the mixed conductor well above the applied voltage, and

(v)   inherently slow oxygen exchange kinetics or efficient sealing of the free surfaces of the mixed conductor to avoid significant oxygen exchange with the surrounding gas atmosphere.

If one or several of these requirements are not fulfilled, an electronic leakage current (cases (i), (ii), and (v)), ionic leakage current (case (iv)) or the transport of gaseous oxygen through the mixed conductor (case (iii)) might result in erroneous conductivity values. The numerous potential error sources as well as the typically large relaxation times make electrochemical polarization experiments a measuring technique not always straightforward to apply.

2.3   Mixed-Conducting (Bi,Sr)(Co,Fe)O$_{3-\delta}$ in Literature

Bi$_{1-x}$Sr$_x$FeO$_{3-\delta}$ is known to form a continuous series of solid solutions between bismuth ferrite (BiFeO$_{3-\delta}$) and strontium ferrite (SrFeO$_{3-\delta}$) over the entire compositional range ($0 < x < 1$).[81-82] The end member BiFeO$_{3-\delta}$ crystallizes with a rhombohedrally distorted perovskite structure (space group $R3c$); the wide-band-gap semiconductor (band gap ca. 2.3 eV to ca. 2.8 eV at room temperature) has attracted enormous interest in recent years as it is one of the very few materials exhibiting both magnetic (T_N = 370°C) and ferroelectric (T_C = 825-840°C) ordering at room temperature and, therefore, being potentially exploitable in various devices based on magnetoelectric coupling.[83] SrFeO$_{3-\delta}$ possesses an oxygen-vacancy-ordered tetragonal perovskite structure (SrFeO$_{2.86}$, space group $I4/mmm$)

at room temperature if synthesized under ambient conditions and a disordered cubic perovskite structure (space group $Pm\bar{3}m$) at temperatures above 850°C inducing a high electronic ($\sim$ 240 S cm^{-1} at 900°C and a $p(O_2)$ of 0.2 bar)[61] and ionic ($\sim$ 0.2 S cm^{-1} at 900°C)[61] conductivity. Below 850°C, this cubic phase, however, transforms at a $p(O_2)$-dependent temperature into an ordered brownmillerite phase (SrFeO$_{2.5}$, space group $Icmm$) with low ionic conductivity making SrFeO$_{3-\delta}$ unsuitable for applications, for example, in SOFCs or as oxygen permeation membranes.[84-87] The Bi$_{1-x}$Sr$_x$FeO$_{3-\delta}$ members with mixed A site occupation mostly crystallize with a cubic perovskite structure (space group $Pm\bar{3}m$),[82] although a certain degree of rhombohedral or tetragonal distortion has been reported by some authors for compositions with low ($x \leq 0.3$) or high ($x \geq 0.9$) Sr content, respectively.[82, 88-89]

Co-containing LSCF or BaSCF perovskites typically show a higher electrical conductivity and a higher catalytic activity for oxygen exchange than the pure ferrites, but also a higher thermochemical expansion coefficient (TEC) and a lower chemical stability towards common electrolytes, such as YSZ and Gd-doped CeO$_2$ (CGO).[90-92] Attempts were made to prepare Bi$_{1-x}$Sr$_x$CoO$_{3-\delta}$ ($0.1 \leq x \leq 1.0$), but essentially phase-pure perovskite-related compounds were identified only for $0.8 \leq x \leq 0.9$, and a vacancy-ordered tetragonal supercell structure (space group $I4/mmm$) was attributed to the as-prepared materials.[93-94] The only report existing about BiSCF containing both Co and Fe on the B site mainly focuses on structural investigations on the Sr-rich compositions Bi$_{0.15}$Sr$_{0.85}$Co$_{1-y}$Fe$_y$O$_{3-\delta}$ with $0 \leq y \leq 1$.[95] No detailed literature reports, on the other hand, are available dealing with Bi-richer ($x \approx 0.5$) Co- and Fe-containing BiSCF exhibiting a composition close to that of the LSCF and BaSCF perovskites studied previously.

The substitution of Bi^{3+} by Sr^{2+} in the BiSCF perovskites introduces a charge imbalance with respect to the reference perovskite A^{3+}B^{3+}O$_3$, which is compensated by the formation of electronic defects and/or oxygen vacancies giving rise to significant electronic and/or ionic conductivity. Oxygen permeation measurements on Bi$_{1-x}$Sr$_x$FeO$_{3-\delta}$ ($0.05 \leq x \leq 0.9$) confirmed the materials to be mixed conductors,[88, 96-98] and the oxygen permeation flux of Bi$_{0.3}$Sr$_{0.7}$FeO$_{3-\delta}$ was found to increase by up to a factor of 4 by introduction of 20 mol% of Co on the perovskite B site.[99] From the oxygen permeation flux, ionic conductivity values of 0.004-0.035 S cm^{-1} at 800°C were calculated for Bi$_{1-x}$Sr$_x$FeO$_{3-\delta}$ with $0.05 \leq x \leq 0.8$.[88, 100] BiSCF was, furthermore, proposed as SOFC cathode material.[56, 101] Recent electrical conductivity relaxation measurements on Bi$_{0.5}$Sr$_{0.5}$FeO$_{3-\delta}$ pellets yielded an oxygen exchange rate constant k^δ of 5.4 $\times$ 10^{-3} cm s^{-1} at 750°C about 20 times higher than k^δ of La$_{0.6}$Sr$_{0.4}$FeO$_{3-\delta}$ under the same conditions.[100] An area-specific resistance (ASR) of 0.06 Ω cm^2 at 750°C was obtained by EIS for a porous Bi$_{0.5}$Sr$_{0.5}$FeO$_{3-\delta}$ electrode on a Sm-doped CeO$_2$ electrolyte almost one order of magnitude lower than the ASR determined for a porous La$_{0.6}$Sr$_{0.4}$FeO$_{3-\delta}$ electrode prepared in a similar way.[102] The ASR of porous Bi$_{0.3}$Sr$_{0.7}$FeO$_{3-\delta}$ and Bi$_{0.8}$Sr$_{0.2}$FeO$_{3-\delta}$

electrodes was revealed to exceed that of $Bi_{0.5}Sr_{0.5}FeO_{3-\delta}$ by a factor of 1.1 and 3.9, respectively, at 700°C making the intermediate composition the most promising candidate for SOFC applications.[103] However, a reliable attribution of the individual features observed in the impedance spectra of porous electrodes was not possible emphasizing the importance of morphologically well-defined dense model electrodes for detailed investigations of the oxygen exchange kinetics.

3 Experimental

3.1 Preparation of Bulk Samples

Most of the powder samples were prepared by solid state reaction from Bi_2O_3, $SrCO_3$, CoO, and Fe_2O_3. Stoichiometric amounts of the respective starting materials were ground together in a mortar. The resulting mixtures were calcined for 2 h at 770°C, ball-milled for 1 h in a zirconia ball mill (Fritsch, Germany), and then heat-treated under the conditions listed in Table 3.1. After each heating step, the reaction mixtures were ball-milled for 1 h. The final heating step carried out for $Bi_{0.2}Sr_{0.8}FeO_{3-\delta}$ was intended to ensure full equilibration of this composition showing particularly strong changes in the oxygen nonstoichiometry δ upon changing temperature (chapter 4.1.3). Following the preparation method described in literature for $Bi_{0.2}Sr_{0.8}CoO_{3-\delta}$[93] Co-containing samples were isostatically cold-pressed into pellets prior to each heating step ($Bi_{0.2}Sr_{0.8}CoO_{3-\delta}$ and $Bi_{0.5}Sr_{0.5}Co_{0.4}Fe_{0.6}O_{3-\delta}$) or before the last heating step ($Bi_{0.5}Sr_{0.5}Co_{0.2}Fe_{0.8}O_{3-\delta}$) and in some cases quenched to room temperature.

Table 3.1. Preparation and sintering conditions for BiSCF powders synthesized via the glycine-nitrate process ($BiFeO_{3-\delta}$) or solid state reaction (others). The samples were heated and cooled at rates of 10 K min^{-1} and 20 K min^{-1} or quenched to room temperature (indicated by "q"). Final average pellet densities are given in brackets.

	Preparation conditions (°C/h)	Sintering conditions (°C/h)
$BiFeO_{3-\delta}$	700/2	870/8 (81%)
$Bi_{0.8}Sr_{0.2}FeO_{3-\delta}$	950/8 (2×)	1050/8 (88%)
$Bi_{0.5}Sr_{0.5}FeO_{3-\delta}$	1050/8 (2×)	1100/8 (86%)
$Bi_{0.2}Sr_{0.8}FeO_{3-\delta}$	1100/8 (2×) - 300/120/q	1100/8 (84%)
$Bi_{0.5}Sr_{0.5}Co_{0.2}Fe_{0.8}O_{3-\delta}$	1050/8 (2×) - 1100/8 - 1050/24/q	-
$Bi_{0.5}Sr_{0.5}Co_{0.4}Fe_{0.6}O_{3-\delta}$	950/24/q (2×) (89%)	-
$Bi_{0.2}Sr_{0.8}CoO_{3-\delta}$	900/20/q - 950/20/q (2×) (84%)	-

For $BiFeO_{3-\delta}$ powder, the highest phase purity was achieved via the glycine-nitrate process[104] starting from a solution of about 0.2 mol l^{-1} of Bi_2O_3 in a 3:2 volume mixture of double-distilled water and 65% nitric acid (added to increase the solubility of the metal oxide) and a solution of about 1 mol l^{-1} of $Fe(NO_3)_3$ in double-distilled water, respectively. The exact concentrations of the metal cations were determined by inductively-coupled plasma optical emission spectroscopy (ICP-OES). A mixture of both solutions corresponding to a 1:1 mol ratio of the metal cations and a total volume of about 70 ml was heated together with 25 g of

glycine per 40 g of the final reaction product in a 2-l beaker covered by a watch glass until the water was evaporated and combustion of the residue completed. The combustion products from two different runs were ground together in a mortar, heat-treated under the conditions given in Table 3.1, and finally ball-milled for 1 h.

To produce targets for pulsed laser deposition (PLD), the prepared Co-free powders were isostatically cold-pressed into cylindrical pellets with about 1 cm in diameter and the pellets sintered in air under the conditions depicted in Table 3.1. For each of the Co-containing compositions, one of the pellets obtained after the final heating step (see above) was used as target. The average density of the pellets (Table 3.1) ranged from 81% to 89% of the theoretical density calculated from the lattice constant from X-ray diffraction (XRD) which was considered to be sufficient for PLD. For electrical conductivity and thermochemical expansion measurements, however, $Bi_{1-x}Sr_xFeO_{3-\delta}$ (x = 0.2, 0.5, and 0.8) pellets with a higher density were prepared by spark plasma sintering (SPS). Cylindrical pellets with about 5 mm in diameter were sintered for 2.5 min at 650°C (x = 0.2) or for 5 min at 800°C (others) under a pressure of 350 MPa in graphite dies in a HP D 5 SPS furnace (FCT Systeme, Germany). After reoxidation in air at the preparation temperature of the respective composition for 12 h in a conventional furnace, average pellet densities of 94% (x = 0.2), 96% (x = 0.5), and 88% (x = 0.8) of the theoretical density were reached. SPS was performed by the former and current PhD students at the department of Professor Maier at the Max Planck Institute for Solid State Research, Dr. Piero Lupetin and Kiran K. Adepalli.

3.2   Characterization of Bulk Samples

3.2.1   General Characterization

The powder and pellet samples were analyzed by X-ray diffraction after preparation as well as after subsequent measuring steps to identify the present phases. XRD analyses were carried out on a PW 3710 X-ray diffractometer (Philips, Netherlands) at room temperature using Cu K_α radiation in Bragg-Brentano geometry. Standard XRD measurements were performed with a resolution of $\Delta 2\theta$ = 0.02° and a detection time of 1 s per step. The X-ray diffractograms in Fig. 4.1 were recorded with an increased detection time of 15 s per step to improve the signal-to-noise ratio. The lattice constants of powders were calculated via the Rietveld method using Topas version 4.2. Raman spectroscopy measurements on as-prepared powders were conducted by means of a V 010 LabRAM spectrometer (Jobin Yvon, Germany). The Raman spectra with a resolution of 1 cm^{-1} were acquired in quasi-backscattering geometry using linearly polarized radiation with a wavelength of 633 nm provided by a He-Ne gas laser with a power of less than 1 mW and focused to a spot with 10 μm in diameter on the sample surface. XRD

measurements and the calculation of the lattice parameters was done by Gabi Götz from the department of Professor Maier, and Raman spectroscopy measurements were carried out by Armin Schulz from the Spectroscopy Service Lab at the Max Planck Institute for Solid State Research.

3.2.2   Determination of the Oxygen Nonstoichiometry

The absolute oxygen nonstoichiometry of as-prepared powders was determined by cerimetric titration. About 100 mg of the sample powder and about 100 mg of $FeCl_2 \cdot 4H_2O$ (Acros Organics, Belgium) were transferred into a Schlenk flask and the flask flushed thoroughly with N_2. Approximately 100 ml of 6 mol l^{-1} HCl solution, previously flushed with N_2, were added under a N_2 flow and the flask sealed immediately. The resulting mixture was stirred for about 1 h at 80°C in an ultrasonic bath until the sample powder was completely dissolved and all Fe^{4+} and Co^{3+} present in the oxide reduced by the Fe^{2+} in $FeCl_2 \cdot 4H_2O$ following

$$Fe^{4+} + Fe^{2+} \rightarrow 2Fe^{3+} \tag{3.1}$$

$$Co^{3+} + Fe^{2+} \rightarrow Co^{2+} + Fe^{3+} \tag{3.2}$$

Thereafter, the reaction mixture was cooled in a cold water bath, 1-2 drops of 1/40 mol l^{-1} 1,10-phenanthroline iron(II) sulfate (ferroin) solution (Merck, Germany) were added as indicator, and the titration performed under a flow of N_2 with 0.05 mol l^{-1} $Ce(SO_4)_2$ solution (Riedel-de Haën, Germany) oxidizing the remaining Fe^{2+} according to

$$Fe^{2+} + Ce^{4+} \rightarrow Fe^{3+} + Ce^{3+} \tag{3.3}$$

The $Ce(SO_4)_2$ solution was standardized using Oesper's salt $FeC_2H_4(NH_3)_2(SO_4)_2 \cdot 4H_2O$ (Alfa Aesar, Germany) and the purity of the $FeCl_2 \cdot 4H_2O$ checked by blind titration. For each investigated composition, three titrations were carried out and the reproducibility of the obtained δ values calculated to ±0.001.

Thermogravimetric (TG) analyses of δ changes were conducted using a STA 449 C Jupiter thermobalance (Netzsch-Gerätebau, Germany) in N_2/O_2 mixtures at a total gas flow rate of 50 ml min^{-1}. About 300 mg of the sample powder were first heated to 850°C and kept at this temperature for 1 h to remove possible impurities such as water or carbonate. Subsequently, the sample was cooled down to 300°C with cooling rates of 3 K min^{-1} (850-600°C), 1.5 K min^{-1} (600-450°C), and 0.7 K min^{-1} (450-300°C) and again heated to 850°C with the same rates in order to check if full equilibration had been reached at any temperature. For $Bi_{0.2}Sr_{0.8}FeO_{3-\delta}$

the mass change curve showed hysteresis at low temperatures, and the cooling/heating rates were decreased for this composition to 1 K min^{-1} (850-600°C), 0.5 K min^{-1} (600-450°C), and 0.2 K min^{-1} (450-300°C). To adjust the curves obtained at different oxygen partial pressures with respect to each other, the mass changes resulting from stepwise changes in the $p(O_2)$ were recorded at 700°C. Buoyancy effects were accounted for by subtraction of the mass changes detected for an empty alumina crucible (quartz glass was found not to be suitable as crucible material as it underwent a reaction with the BiSCF perovskite under the described conditions).

3.2.3   Determination of the Oxidation Enthalpy

The oxidation enthalpy was measured by differential scanning calorimetry (DSC). Approximately 300 mg of the sample powder were heated in a DSC 121 Tian-Calvet calorimeter (Setaram Instrumentation, France) to the desired temperature at a $p(O_2)$ of 10^{-3} bar adjusted via a N_2/O_2 mixture at a total gas flow rate of 10 ml min^{-1}. Then, the $p(O_2)$ was changed stepwise in the order 10^{-3}→0.03→1→0.03→10^{-3}→1→10^{-3} bar and the heat flow recorded associated with oxidation/reduction of the sample. From the heat flow and the oxygen nonstoichiometry data from TG analyses, the molar oxidation enthalpy was calculated. To calibrate the oxidation enthalpy, an Al and a Pb reference sample were heated at a $p(O_2)$ of 10^{-3} bar with different heating rates (10, 5, 2, 1, and 0.5 K min^{-1}) and the enthalpy determined associated with melting of the sample at around 660°C (Al) and 327°C (Pb). The correction factors deduced by comparison of the measured melting enthalpies extrapolated to a heating rate of 0 K min^{-1} with literature values were used to adjust the oxidation enthalpies obtained at 450°C (Pb correction factor) and higher temperatures (Al correction factor). A DSC measurement on an empty alumina crucible at 650°C did not yield any peaks of the heat flow upon changing $p(O_2)$. During all DSC experiments, the $p(O_2)$ was monitored using a lambda probe made in-house.

3.2.4   Determination of the Electrical Conductivity

Electrical conductivity measurements were carried out on bars with about $3.5 \times 3.5 \times 1.5$ mm^3 in size cut from the pellets prepared by SPS and subsequent annealing (chapter 3.1). Pt electrodes with a thickness of about 200 nm were sputtered onto both small sample faces using an Auto 306 sputtering system (Edwards, UK), and two pieces from Pt foil were attached via spring load to the sputtered electrodes. Each of these pieces was contacted by two Pt wires to build a simplified four-probe measuring setup. A real four-probe arrangement appeared not to be realizable due to the small sample size. Possible contributions from the electrode-sample contact resistance to the overall measured resistance were assumed to be negligible. The sample was heated in a quartz tube flushed with appropriate mixtures of N_2 and O_2 or CO (100 ppm in N_2) and CO_2 at a total gas

flow rate of 50 ml min^{-1}. The actual $p(O_2)$ was monitored by a ZR5 oxygen measuring module (Zirox, Germany) connected to the gas outlet. Impedance spectra were recorded with an Alpha-A high performance frequency analyzer version 6.2ANB equipped with a ZG4 4 wire impedance test interface (both Novocontrol Technologies, Germany) applying an AC voltage amplitude of 10 mV. Temperature-dependent conductivity measurements were first conducted in the direction of decreasing temperature and then, with larger step size, in the direction of increasing temperature. Except for $Bi_{0.2}Sr_{0.8}FeO_{3-\delta}$ the electrical conductivity did not show significant hysteresis upon heating. Finally, $p(O_2)$-dependent measurements were performed typically in the direction of increasing $p(O_2)$ starting at the highest temperature (only the $Bi_{0.8}Sr_{0.2}FeO_{3-\delta}$ sample was measured in the order 750°C at $p(O_2) > 10^{-4}$ bar $\rightarrow$ 500°C at $p(O_2) > 10^{-4}$ bar $\rightarrow$ 600°C $\rightarrow$ 700°C $\rightarrow$ 550°C $\rightarrow$ 750°C at $p(O_2) < 10^{-4}$ bar $\rightarrow$ 500°C at $p(O_2) < 10^{-4}$ bar).

3.2.5   Determination of the Thermochemical Expansion Coefficient

Measurements of the thermochemical expansion coefficient were performed on bars with a size of about $3.5 \times 3.5 \times 1.5$ mm^3 cut from the pellets produced by SPS and subsequent annealing (chapter 3.1). The bars were heated to 800°C in a DIL 802 dilatometer (Bähr Thermoanalyse, Germany) flushed with a mixture of O_2 and inert gas at a total gas flow rate of 50 ml min^{-1} with a Rapidox 2100 oxygen analyzer (Cambridge Sensotec, UK) attached to the gas outlet and kept at this temperature for 30 min to remove possible impurities. Then, the samples were cooled to room temperature with a rate of 1 K min^{-1}, equilibrated for 1 h, and again heated to 800°C with the same rate in order to check the reproducibility of the detected length changes. The mean coefficient of linear thermochemical expansion was calculated to $(1/L_0)(\Delta L/\Delta T)$ (L_0: initial sample length at the temperature T_0, T_0: reference temperature 20°C, $\Delta L = L_i - L_0$, $\Delta T = T_i - T_0$). As mentioned in chapter 4.1.6, the mean TEC needs to be distinguished from the instantaneous TEC defined as $(1/L_0)(dL/dT)$. All TEC measurements were corrected against the thermochemical expansion recorded for a sapphire standard sample with comparable dimensions.

3.3   Preparation of Thin-Film Samples

To perform PLD of thin films, the targets obtained by conventional sintering (chapter 3.1) were attached to the target holder by silver epoxy (H31D, Epoxy Technology, USA), the paste allowed to harden for 1 h at 140°C, and the target surface polished with SiC polishing paper (P 280 and P 800, Leco Instrumente, Germany). Thin films were deposited on polished 9.5 mol% Y_2O_3-doped ZrO_2 single crystal substrates with (100) orientation and dimensions $5 \times 5 \times 0.5$ mm^3 as well as on polished MgO single crystal substrates with the same orientation and dimensions $10 \times 5 \times 0.5$ mm^3 (both CrysTec, Germany). Prior to PLD, the

substrates were cleaned in acetone in an ultrasonic bath. The MgO single crystals were covered in some cases by a shadow mask cut out from sapphire to produce BiSCF stripes with a length of 9 mm and a width of 2 mm used for electrochemical polarization measurements. The substrates were heated to the desired temperature in a PLD chamber built in-house at the background oxygen pressure specified in Table 3.2. Calibration of the substrate temperature had been carried out previously by measuring the actual temperature of a $SrTiO_{3-\delta}$ substrate and a 250 nm thin layer of $La_{0.7}Sr_{0.3}MnO_{3\pm\delta}$ on $SrTiO_{3-\delta}$ with known emissivity upon heating at a $p(O_2)$ of 0.4 mbar and 1 bar via a KT 19.99 infrared pyrometer (Heimann Sensor, Germany).

Table 3.2. Substrate temperature and background oxygen pressure for PLD of BiSCF thin films on (100)-oriented YSZ and MgO single crystal substrates.

	Deposition temperature (°C)	Deposition pressure (mbar)
$BiFeO_{3-\delta}$*	650	0.01
$Bi_{0.8}Sr_{0.2}FeO_{3-\delta}$	700/650**	0.4/0.01**
$Bi_{0.5}Sr_{0.5}FeO_{3-\delta}$	650	0.4
$Bi_{0.2}Sr_{0.8}FeO_{3-\delta}$	650	0.4
$SrFeO_{3-\delta}$***	770	0.4
$Bi_{0.5}Sr_{0.5}Co_{0.2}Fe_{0.8}O_{3-\delta}$	650	0.1
$Bi_{0.5}Sr_{0.5}Co_{0.4}Fe_{0.6}O_{3-\delta}$	650	0.001
$Bi_{0.2}Sr_{0.8}CoO_{3-\delta}$	600	0.4

*deposited at a repetition frequency of 10 Hz
**conditions for the deposition on MgO (100)
***annealed at 650°C

Then, the film deposition was performed by means of a KrF excimer laser (LPX 200, Lambda Physik, Germany) with a wavelength of 248 nm typically at a repetition frequency of 5 Hz, an energy density of 1.6 J cm^{-2} per pulse, and a target-to-substrate distance of 30 mm or 40 mm. Prior to the actual film deposition, the target was ablated with closed shutter for 3 min to clean the target surface. A film deposition rate of 0.27 Å per pulse was assumed corresponding to the deposition rate determined previously for 20 mol% Y_2O_3-doped ZrO_2. The films were deposited with a nominal thickness of 200 nm if not indicated otherwise. According to the results from scanning electron microscopy (SEM) analyses of thin-film cross sections (chapter 4.2.2), the actual film thickness can amount to less than half of the nominal one. For the present evaluation, a film thickness of 150 nm obtained for a nominally 200 nm thin $Bi_{0.5}Sr_{0.5}FeO_{3-\delta}$ film on YSZ was used to normalize the chemical capacitance of all compositions from microelectrode EIS measurements (chapter 4.3), and a film thickness of 80-170 nm deduced for nominally 200 nm thin BiSCF films on MgO was applied to derive the ionic conductivity from thin-film electrochemical polarization measurements

(chapter 4.4). After the deposition, the oxygen pressure was increased to 1 bar and the films annealed at the respective deposition temperature for 20 min. A part of the PLD runs were carried out by Georg Christiani and Benjamin Stuhlhofer from the Scientific Service Group Technology at the Max Planck Institute for Solid State Research.

3.4 Characterization of Thin-Film Samples

3.4.1 General Characterization

XRD analyses of thin films after preparation and, if not structured into microelectrodes, subsequent measuring steps were conducted as described for powder samples (chapter 3.2.1) with a detection time of 1 s per step. Additional grazing-incidence (GI-) XRD measurements were performed for an annealed $Bi_{0.5}Sr_{0.5}Co_{0.4}Fe_{0.6}O_{3-\delta}$ film using a MRD Eulerian cradle (Philips, Netherlands). Scanning electron microscopy was carried out on a Merlin and a CrossBeam 1540 EsB scanning electron microscope (both Carl Zeiss, Germany). To reduce electrostatical charging resulting from the low electrical conductivity of film and/or substrate, the films were fixed with a metal clamp and the measurements conducted in the vicinity of the clamp. Transmission electron microscopy (TEM) was performed on a JEM-4000FX transmission electron microscope (Jeol, Japan) at an acceleration voltage of 400 kV and a spatial resolution of 0.2 nm. For TEM analyses, a lamella was cut out from the film surface by a focused ion beam (FIB) consisting of gallium ions at an acceleration voltage of 30 kV after deposition of a layer of amorphous carbon to minimize electrostatical charging.

Inductively-coupled plasma optical emission spectroscopy was carried out on a Ciros CCD spectrometer (Spectro Analytical Instruments, Germany) following dissolution of the powders or two film samples with a nominal thickness of 600 nm per composition in a 2:3 volume mixture of concentrated hydrochloric acid and concentrated nitric acid. Energy-dispersive X-ray spectroscopy (EDX) was accomplished on a Vega TS 5130 mm scanning electron microscope (Tescan, Czech Republic) again fixing the film samples via a metal clamp. Finally, an Axis Ultra instrument (Kratos Analytical, UK) operating with Al K_α radiation was used for X-ray photoelectron spectroscopy (XPS). The general film characterization was done by Gabi Götz (XRD), Annette Fuchs (SEM), Bernhard Fenk (SEM and FIB etching), Christof Busch (EDX), and Dr. Mitsuharu Konuma (XPS) from the Max Planck Institute for Solid State Research and Gerd Maier (GI-XRD), Dr. Fritz Phillipp (TEM) as well as Albrecht Meyer and Gerhard Werner (ICP-OES) from the Max Planck Institute for Intelligent Systems.

3.4.2 Microelectrode EIS Measurements

For EIS investigations of the oxygen exchange kinetics, thin films on YSZ were structured into arrays of circular microelectrodes with 20-100 µm in diameter by photolithography and inert gas ion beam etching. First, the film was covered with a 1.0-1.5 µm thin layer of positive photoresist (ma-P 1215, micro resist technology, Germany) by spin coating. A photomask was placed on top of the photoresist layer consisting of a transparent sheet from fused silica with photolithographically produced Cr spots defining the desired microelectrode shapes (see also ref. [72]). The sample was exposed to broadband UV radiation from a high-pressure Hg lamp and the parts of the light-sensitive photoresist not covered by the Cr spots dissolved in developer solution (ma-D 531, micro resist technology, Germany) leaving behind columns of photoresist on the BiSCF film. The remaining photoresist was hard-baked for about 1 h at 110°C to ensure sufficient stability for the subsequent etching step. Then, the sample was etched using a beam of neutralized Ar ions in a UniLab ion beam etching system (Roth & Rau, Germany) until the free BiSCF film as well as a large part of the photoresist columns was ablated. The leftover photoresist served to protect the microelectrode surface from damage by the Ar beam and was finally removed with acetone. Photolithography and inert gas ion beam etching was carried out by Stephan Schmid and Benjamin Stuhlhofer from the Scientific Service Group Technology at the Max Planck Institute for Solid State Research.

The obtained microelectrode samples were processed further to generate the desired electrochemical cells: A sheet of Ag foil was attached to the back side of the sample via Ag paste (Leitsilber 6200/0007, Oegussa, Austria) providing an extended porous counter electrode with low impedance.[72] For sample support, the whole cell was fixed on a piece of sapphire with dimensions $6 \times 6 \times 0.53$ mm^3 (CrysTec, Germany) again using Ag paste. The sample was heated in a vacuum chamber (Vacom, Germany) evacuated and then flushed with a N_2/O_2 mixture at a total gas flow rate of 200 ml min^{-1}. The actual $p(O_2)$ in the chamber was monitored by a Rapidox 2100 oxygen analyzer (Cambridge Sensotec, UK) at the gas outlet. Temperature calibration was done before via measuring the actual temperature of a YSZ substrate supported by Ag foil and sapphire by means of a thermocouple with only 0.002 inch in diameter (Omega Engineering, USA) glued to the sample surface with Ag paste. To record impedance spectra, a microelectrode and the Ag counter electrode were contacted by needles of a Pt/Ir alloy with a nominal tip radius of 2.5 µm (Moser Company, USA) (Fig. 3.1). The spectra were recorded using an Alpha high resolution dielectric analyzer version 1.06 (Novocontrol Technologies, Germany) with an AC voltage amplitude of 10 mV in the frequency range from 10 mHz to 1 MHz. Details about the measuring routine and possible degradation phenomena will be given in chapter 4.3. For the evaluation of impedance spectra, capacitive contributions were represented in the applied

equivalent circuit (Fig. 4.18) by constant phase elements Q and the respective capacitances C calculated via[105]

$$C = (R^{1-n}Q)^{1/n} \tag{3.4}$$

where the parameter n accounts for the typically observed depression of the semicircles.
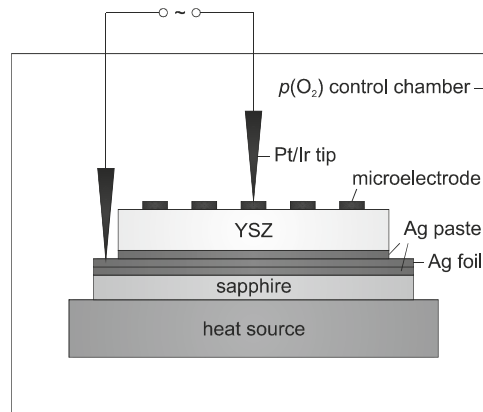

Fig. 3.1. Schematic depiction of the setup for EIS measurements on microelectrode samples.

3.4.3   Macroscopic EIS Measurements

An alternative set of samples for EIS investigations of the oxygen exchange kinetics, due to the comparably large electrode size in the following referred to as "macroscopic samples", was prepared by PLD of BiSCF layers onto both sides of a YSZ substrate. A very fine Au mesh (1000 wires/inch, Precision Eforming, USA) produced by electroplating was attached to both large sample surfaces to minimize sheet resistance. Two additional electrodes from Au foil were fixed via spring load on top of the electroplated mesh as the latter proved to be too fragile to be contacted by wires for current collection. The sample was placed in a quartz tube flushed with 50 ml min^{-1} of a mixture of N_2 and O_2 with the $p(O_2)$ being monitored by a Rapidox 2100 oxygen analyzer (Cambridge Sensotec, UK) connected to the gas outlet. An Alpha high resolution dielectric analyzer version 1.06 (Novocontrol Technologies, Germany) was used to record impedance spectra with an AC voltage amplitude of 10 mV covering the frequency range from 10 mHz to 1 MHz. Temperature and $p(O_2)$-dependent measurements were conducted following the routine applied for the investigation of microelectrode samples.

3.4.4   Electrochemical Polarization Measurements

To produce thin-film electrochemical polarization cells for ionic conductivity measurements, first an electron-blocking electrode from 10 mol% Sc_2O_3-doped ZrO_2 (ScSZ) was deposited by PLD onto one end of the 2 mm broad stripes of BiSCF on MgO. A cylindrical pellet with about 1.5 cm in diameter was prepared from ScSZ powder (Fuelcellmaterials, USA) by SPS for 5 min at 1200°C under a pressure of 50 MPa. The obtained target was polished with SiC polishing paper (P 280 and P 800, Leco Instrumente, Germany) and fixed by a target holder made in-house.[106] The BiSCF stripes were covered by a suitable sapphire shadow mask and heated to 500°C at a background oxygen pressure of 0.01 mbar in a PLD chamber (MDC Vacuum Products, USA) equipped with a KT 19.99 infrared pyrometer (Heimann Sensor, Germany) for in-situ temperature calibration. Then, the deposition of a nominally 1000 nm thin and 2 mm wide ScSZ layer was carried out using a COMPexPro 102 KrF excimer laser (Coherent, USA) with a wavelength of 248 nm at a repetition frequency of 5 Hz, an energy density of 1.5 J cm^{-2} per pulse, and a target-to-substrate distance of 43 mm after preablation of the target for 3 min. The deposition duration was calculated based on the deposition rate of YSZ of 0.26 Å per pulse yielding ScSZ films with an actual thickness used for quantitative evaluations of about 760 nm as deduced from SEM images of a fractured sample. After the deposition, the films were annealed for 30 min at 500°C and an oxygen pressure of 1 bar.

In the next step, an Al_2O_3 sealing layer with a nominal thickness of 300 nm was deposited by electron beam evaporation in a Univex 450 deposition unit (Oerlikon Leybold Vacuum, Germany) onto a large part of the sample, whereas the sample ends were left unsealed by using a suitable sapphire shadow mask. The deposition of the Al_2O_3 layers was performed by Yvonne Link from the Scientific Service Group Technology at the Max Planck Institute for Solid State Research. Finally, two Pt electrodes with a thickness of about 200 nm and a width of 0.7 mm and 1 mm were sputtered onto the ScSZ-covered and free sample end by means of an Auto 306 sputtering system (Edwards, UK). A schematic depiction of a thin-film electrochemical polarization cell and more details about the cell setup will be given in chapter 4.4.1. The sputtered Pt electrodes were electrically contacted via a contact piece consisting of two stripes of Pt foil glued (Ultra-Temp 516, T-E-Klebetechnik, Germany) to a piece of sintered Al_2O_3. The Al_2O_3 piece was designed according to the model described in ref. [106], that is, with a 7 mm deep gap between the two stripes preventing a significant leakage current through the contact piece. An identical arrangement of sputtered Pt electrodes and contact piece was used for measurements of the electrical conductivity on thin films deposited on MgO.

The electrochemical polarization cells were heated in a quartz tube under a flow of 50 ml min^{-1} of a N_2/O_2 mixture. The actual $p(O_2)$ was monitored by a ZR5 oxygen

measuring module (Zirox, Germany) attached to the gas outlet. EIS measurements were conducted using an Alpha high resolution dielectric analyzer version 1.06 (Novocontrol Technologies, Germany) with an AC voltage amplitude of 100 mV in the frequency range from 10 mHz to 1 MHz. DC measurements were performed by means of a 2400 SourceMeter (Keithley Instruments, USA) recording the current response to a stepwise change of the applied DC voltage typically from 0 mV to 100 mV. The typical measuring routine consisted in determining the temperature dependence of the current response in the temperature range from 650°C to 500°C in the direction of decreasing temperature at a $p(O_2)$ of 10^{-3} bar. Subsequently, a DC curve was acquired at 600°C and the same $p(O_2)$ on one sample of each composition in order to account for possible degradation phenomena. Thereafter, the $p(O_2)$ dependence was examined via a DC measurement at 600°C and a $p(O_2)$ of 1 bar. A final DC measurement was carried out again at 600°C and a $p(O_2)$ of 1 bar with a higher applied DC voltage of 150 mV to probe the linearity of the current-voltage relationship.

3.5   Numerical Modeling

The two-dimensional empirical numerical model applied to simulate the effect of high sheet resistance on the impedance of thin-film microelectrodes is described in detail in ref. [107]. Numerical simulations were conducted based on the finite element method (FEM) using the adapted routine implemented by Lynch et al.[108] in Comsol Multiphysics without scaling factors on the simulation domain shown in Fig. 3.2. Assuming uniformity of the electrochemical potential of electrons throughout the film thickness, the 3D microelectrode was converted into a 2D circular shape serving as boundary of the cylindrical electrolyte as defined in the "weak form, boundary" mode of the software. The radius r_{YSZ} of the electrolyte cylinder was set sufficiently large (r_{YSZ} = 500 μm) not to exhibit any influence on the simulation results. The experimentally derived microelectrode impedance spectra are typically dominated by one semicircle, which might be represented by a (globally valid) parallel connection of a resistance attributed to the surface reaction and a capacitance interpreted as "chemical capacitance" (chapter 4.3.1). Consequently, the electrode kinetics was also represented by (locally valid) parallel connections of surface resistance and chemical capacitance in the simulations. The area-normalized chemical capacitance values used as input values
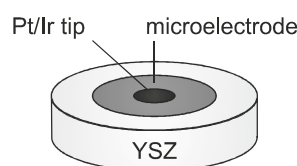
Fig. 3.2. Schematic depiction of the simulation domain covered in FEM simulations.

for the simulations were later on normalized to the electrode volume by dividing
through the actual electrode thickness.

4 Results

4.1 Characterization of Bulk Samples

4.1.1 Structure

The powder XRD patterns of Co-free $Bi_{1-x}Sr_xFeO_{3-\delta}$ (x = 0.2, 0.5, and 0.8) (Fig. 4.1) are consistent with the formation of single-phase reaction products with undistorted cubic perovskite structure (space group $Pm\overline{3}m$). To the composition with x = 0.8, a tetragonally distorted perovskite structure (space group $P4/mmm$) might be assigned as well. The lattice constants (Table 4.1) are in good agreement with literature values (Fig. 4.2) and were found to decrease upon increasing Sr content. The decrease in the lattice constant is typically more pronounced for $Bi_{1-x}Sr_xFeO_{3-\delta}$ compositions with higher Sr content (x > 0.5) as indicated by the steeper slope of the corresponding line of best fit in Fig. 4.2. For the Sr-rich perovskites, the lattice constant decrease can mainly be explained by the increase in the average oxidation state of Fe with increasing Sr content (chapter 4.1.3), since the ionic radius of Sr^{2+} (1.44 Å in 12-fold coordination)[109] is comparable to or larger than that of Bi^{3+} (increasing from $\sim$ 1.30 Å to $\sim$ 1.45 Å upon increasing lone-pair character of the 6s electrons in 12-fold coordination).[109] The reason for the large lattice constants reported for some of the Bi-rich perovskites is not clear.

The powder XRD pattern of the intermediate composition $Bi_{0.5}Sr_{0.5}FeO_{3-\delta}$ shows additional weak reflections in particular also at low Bragg angle (2θ = 15.9°) indicating a large lattice constant. These reflections were first supposed to result from a superstructure in the form of an ordered arrangement of oxygen vacancies. Ordering of oxygen vacancies is known to occur in a large number of perovskites particularly at low temperature and can lead to a significant drop in the ionic conductivity of these materials.[110-111] In neutron diffraction patterns of $Bi_{0.5}Sr_{0.5}FeO_{3-\delta}$ powder recorded at temperatures up to 600°C, the superstructure peaks are visible as weak reflections with large peak width (Fig. 4.3). The appearance of the superstructure peaks even at a temperature as high as 600°C and the low peak intensity (not expected from the high neutron scattering cross section of oxygen) are inconsistent with oxygen vacancy ordering being their origin. The low-2θ reflections might, therefore, rather be caused by superstructure formation in the A-cation sublattice. Attempts to deduce a possible supercell symmetry did, however, not yield an unambiguous result due to the large peak width and low peak intensity.

No indications of distortion from the ideal cubic perovskite structure were found in powder XRD patterns of $Bi_{1-x}Sr_xFeO_{3-\delta}$ with x = 0.2 and 0.5. However,
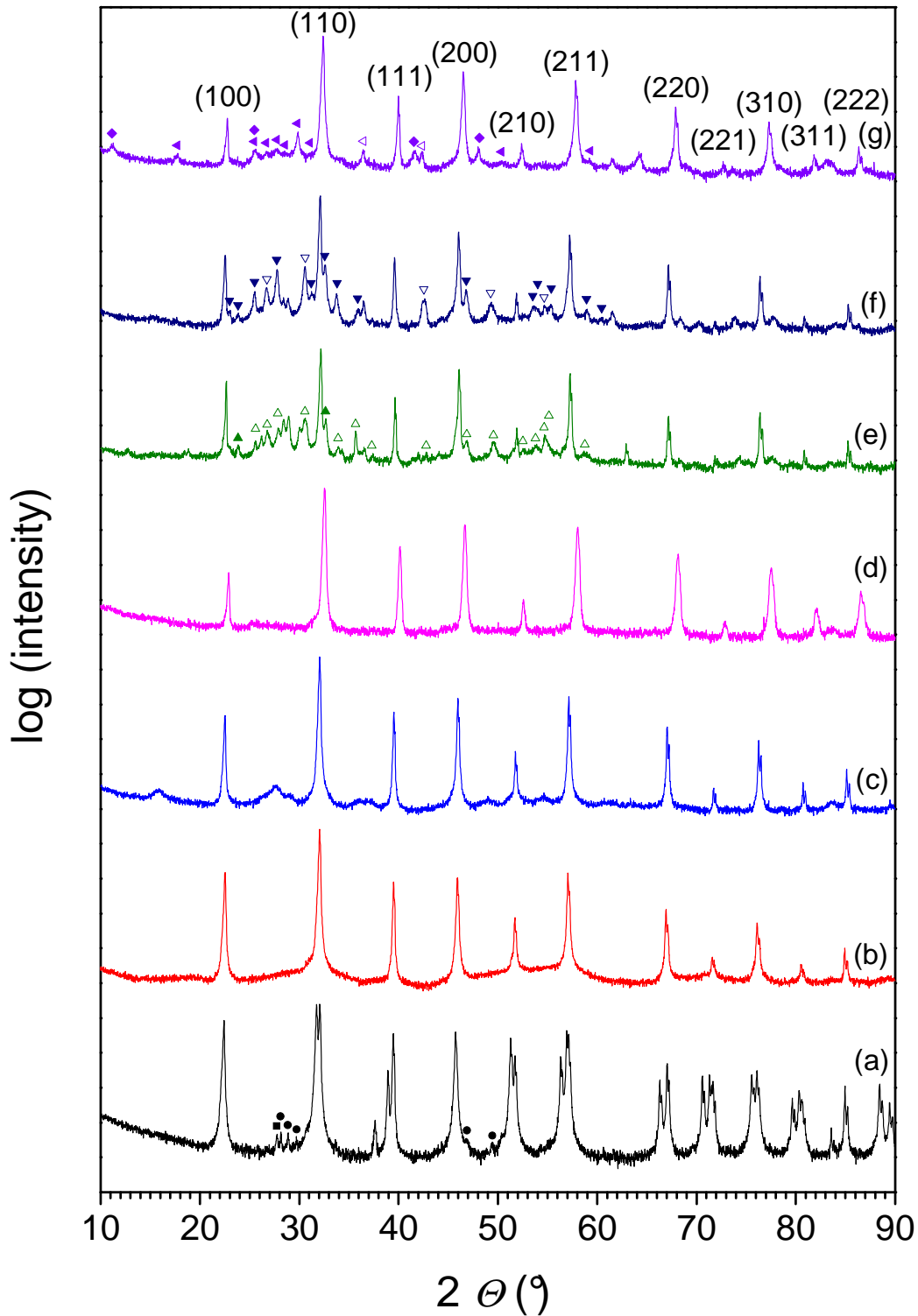
Fig. 4.1. Powder X-ray diffractograms of (a) $BiFeO_{3-\delta}$ (containing small amounts of $Bi_{25}FeO_{39}$ (■) and $Bi_2Fe_4O_9$ (●)), (b) $Bi_{0.8}Sr_{0.2}FeO_{3-\delta}$ (c) $Bi_{0.5}Sr_{0.5}FeO_{3-\delta}$ (d) $Bi_{0.2}Sr_{0.8}FeO_{3-\delta}$ (e) $Bi_{0.5}Sr_{0.5}Co_{0.2}Fe_{0.8}O_{3-\delta}$ (containing a layered perovskite phase (▲), $Bi_6Sr_2O_{11}$, and $Bi_{0.75}Sr_{0.25}O_{1.37}$ (not marked)), (f) $Bi_{0.5}Sr_{0.5}Co_{0.4}Fe_{0.6}O_{3-\delta}$ (containing a layered perovskite phase (▼), $Bi_6Sr_2O_{11}$, and CoO (not marked)), and (g) $Bi_{0.2}Sr_{0.8}CoO_{3-\delta}$ (containing $Sr_2Co_2O_5$ (◆), $Bi_2Sr_3Co_2O_y$ (◀), and CoO (not marked)). Open symbols indicate peaks possibly containing contributions from the respective unmarked impurity phase(s).

Table 4.1. Space group and lattice constants of BiSCF perovskites deduced from the powder X-ray diffractograms in Fig. 4.1. The superscript "p" refers to the pseudocubic lattice constant calculated from the unit cell volume, and "q" indicates samples quenched to room temperature.

	Space group	Lattice constant a (Å)	c (Å)
$BiFeO_{3-\delta}$	$R3c$	5.581 or 3.966[p]	13.874
$Bi_{0.8}Sr_{0.2}FeO_{3-\delta}$	$Pm\overline{3}m$	3.955	
$Bi_{0.5}Sr_{0.5}FeO_{3-\delta}$	$Pm\overline{3}m$	3.946	
$Bi_{0.2}Sr_{0.8}FeO_{3-\delta}$	$Pm\overline{3}m$ or $P4/mmm$	3.896 or 3.898	3.891
$Bi_{0.5}Sr_{0.5}Co_{0.2}Fe_{0.8}O_{3-\delta}$[q]	$Pm\overline{3}m$	3.944	
$Bi_{0.5}Sr_{0.5}Co_{0.4}Fe_{0.6}O_{3-\delta}$[q]	$Pm\overline{3}m$	3.940	
$Bi_{0.2}Sr_{0.8}CoO_{3-\delta}$[q]	$Pm\overline{3}m$	3.900	

supplementary structural investigations by means of extended X-ray absorption fine structure (EXAFS) and Raman spectroscopy yielded evidence for a certain degree of structural distortion. In EXAFS measurements at the Fe K edge of $Bi_{1-x}Sr_xFeO_{3-\delta}$ (x = 0.2, 0.5, and 0.8), only little contribution to the EXAFS function due to atoms beyond the first coordination shell of iron was obtained for the samples with x = 0.2 and 0.5 both as-prepared and annealed under high oxygen pressure;[112] a similar behavior was revealed for $LaFeO_{3-\delta}$, $Bi_{0.8}Ca_{0.2}FeO_{3-\delta}$, and brownmillerite-type $SrFeO_{2.5}$. In Raman spectra measured on as-prepared powders of the three Co-free perovskites (Fig. 4.4), peaks were observed for the two Bi-rich compositions corresponding to the first-order Raman peaks detected previously on apparently cubic $BaZrO_3$,[113] but symmetry-forbidden for materials
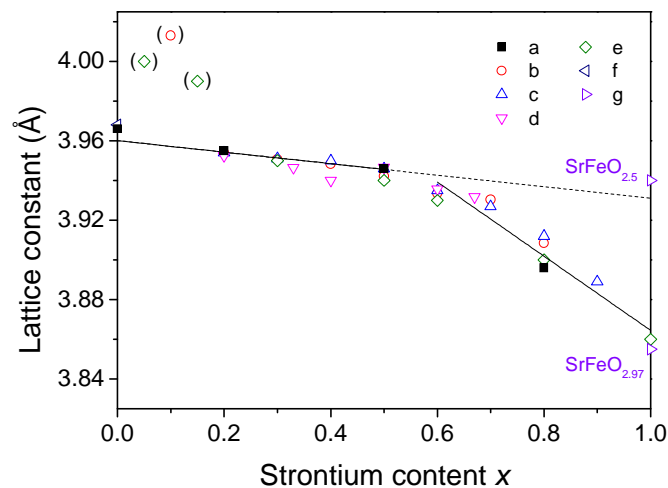
Fig. 4.2. (Pseudo)cubic lattice constants of $Bi_{1-x}Sr_xFeO_{3-\delta}$ perovskites from Table 4.1 (a) and literature (b,[82] c,[98] d,[114] e,[88] f,[83] and g[84]) plotted versus the Sr content. The solid lines represent the best fits obtained for the compositions containing almost exclusively Fe^{3+} ($x \leq 0.5$ and $SrFeO_{2.5}$) and the compositions containing also Fe^{4+} (others), respectively.
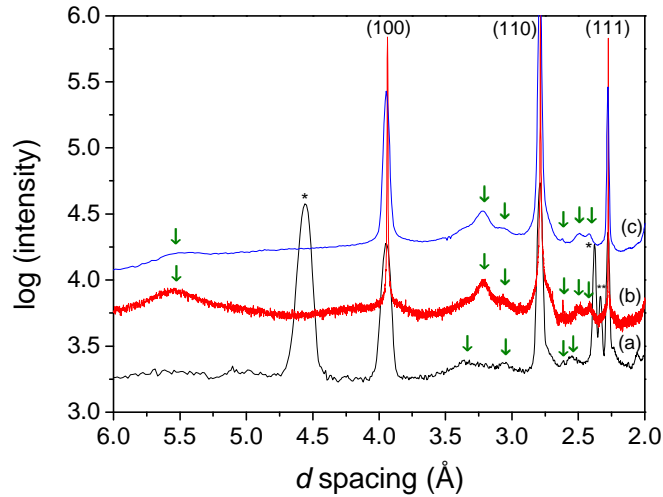
Fig. 4.3. (a) Room-temperature neutron diffractogram of $Bi_{0.5}Sr_{0.5}FeO_{3-\delta}$ powder recorded at the Forschungs-Reaktor München (FRM) II. For comparison, synchrotron X-ray diffractograms obtained for the same sample at the European Synchrotron Radiation Facility (ESRF) (b) and the Deutsches Elektronen-Synchrotron (DESY) (c) are shown. Possible superstructure peaks are indicated by green arrows. Magnetic peaks (*) and peaks originating from the Nb capillary (**) are marked.

with space group $Pm\overline{3}m$. Both effects might be caused by tilting distortions of the FeO_6 octahedra. Such distortions from the aristotype structure occur in 80-90% of the perovskites and can be expected to have great impact on the structure and physical properties, for example, stabilize A-cation ordering and decrease the electronic conductivity.[115]

The synthesis of phase-pure $BiFeO_{3-\delta}$, one end member of the $Bi_{1-x}Sr_xFeO_{3-\delta}$ solid solution series, is reported to be challenging mainly due to the thermodynamically favored structural phase separation into $Bi_{25}FeO_{39}$ and $Bi_2Fe_4O_9$ between 447°C
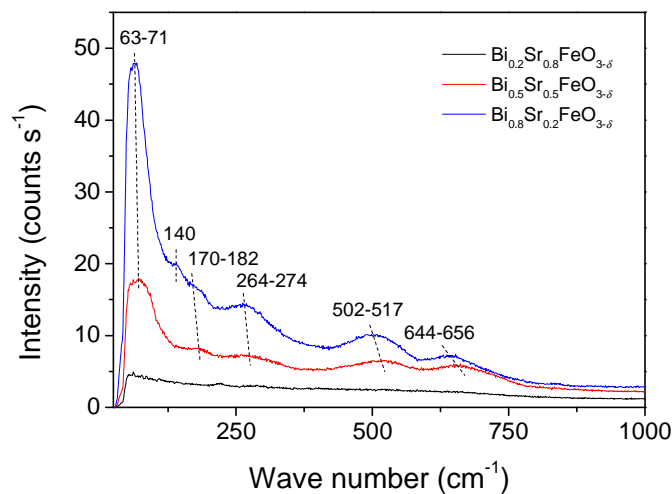
Fig. 4.4. Raman spectra of $Bi_{1-x}Sr_xFeO_{3-\delta}$ powders.

and 767°C.[116] Several synthesis methods described in literature were tried (including rapid liquid-phase synthesis[117] and different wet chemical protocols[104, 116, 118-119]). The best result was achieved with the glycine-nitrate process[104] yielding a rhombohedrally distorted perovskite with space group $R3c$ and lattice parameters (Table 4.1) in good agreement with literature values.[83] Only small amounts of $Bi_{25}FeO_{39}$ and $Bi_2Fe_4O_9$ were detected by XRD in the final powder and target for PLD. Since the target material completely decomposes into its atomic constituents during laser ablation, minor fractions of secondary phases are, however, assumed not to inhibit the single-phase film growth.

Fe-free $Bi_{0.2}Sr_{0.8}CoO_{3-\delta}$ was prepared by a procedure similar to that described by Tolochko et al.[93] including quenching of the sample from the final synthesis temperature. A cubic perovskite phase with space group $Pm\overline{3}m$ was obtained according to powder XRD (Fig. 4.1). In addition, small amounts of a layered perovskite-like phase $Bi_2Sr_3Co_2O_y$,[120] brownmillerite-type $Sr_2Co_2O_5$,[121] and CoO were detected, which are known to be (closely related to) the main reaction products in samples slowly cooled to room temperature.[93] No superstructure reflections or peak splitting indicative of the formation of the tetragonal $I4/mmm$ supercell reported previously[94] were observed possibly due to the low sensitivity of powder XRD to oxygen and the low degree of tetragonal distortion, respectively. A lattice constant of quenched $Bi_{0.2}Sr_{0.8}CoO_{3-\delta}$ (Table 4.1) slightly larger than that of slowly cooled $Bi_{0.2}Sr_{0.8}FeO_{3-\delta}$ was determined from the powder XRD pattern, but the equilibrium room-temperature lattice constant of the Co-containing perovskite is expected to be significantly smaller owing to the increase in oxygen/Co^{3+} content upon equilibration at low temperature. Therefore, the substitution of Fe by Co leads to a decrease in the lattice constant consistent with the smaller size of Co^{3+} in 6-fold coordination compared to Fe^{3+} with the same coordination number and identical spin state.[109]

For the two compositions containing both Co and Fe on the B site, $Bi_{0.5}Sr_{0.5}Co_{0.2}Fe_{0.8}O_{3-\delta}$ and $Bi_{0.5}Sr_{0.5}Co_{0.4}Fe_{0.6}O_{3-\delta}$ the best result was again achieved by quenching the samples from the synthesis temperature. The formed cubic perovskites (space group $Pm\overline{3}m$) were accompanied by small amounts of a layered perovskite phase isostructural to $((Bi,Pb)O)_2Sr_2Bi_2Fe_3O_{10+\delta}$[122] (consisting of perovskite-like slabs alternating with (Bi,Pb)O double sheets) as well as minor amounts of $Bi_6Sr_2O_{11}$ and $Bi_{0.75}Sr_{0.25}O_{1.37}$ or CoO as revealed by powder XRD (Fig. 4.1). The fraction of the layered perovskite phase was significantly larger in samples slowly cooled to room temperature, and strongly decreased during a subsequent heating-quenching cycle. This suggests the formation of the layered perovskite to occur reversibly at lower temperature for this type of compounds. The lattice constants within the series $Bi_{0.5}Sr_{0.5}Co_{1-y}Fe_yO_{3-\delta}$ (y = 0, 0.2, and 0.4) (Table 4.1) were found to decrease with increasing Co content in accordance with the trend observed for the compositions with lower Bi content.

4.1.2   Chemical Compatibility with YSZ

To investigate the compatibility of BiSCF with YSZ as potential electrolyte and substrate material for thin-film measurements, powder mixtures of equal volume fractions of BiSCF and 9.5 mol% Y_2O_3-doped ZrO_2 were ground together in a mortar, annealed for 12 h at different temperatures and then analyzed by XRD. As shown, for example, in Fig. 4.5, Co-free $Bi_{1-x}Sr_xFeO_{3-\delta}$ (x = 0, 0.2, 0.5, and 0.8) proved to be stable towards YSZ until at least 800°C. Upon annealing at 900°C and 1000°C, significant amounts of a phase isostructural to monoclinic ZrO_2 (see, e.g., ref. [123]) (for x = 0.8 only at 1000°C), a new perovskite phase with a lattice constant comparable to that of $SrZrO_3$[124] ($x \geq 0.5$) and a phase isostructural to hexagonal $SrFe_{12}O_{19}$[125] (x = 0.8) were formed. The compatibility of Co-free $Bi_{1-x}Sr_xFeO_{3-\delta}$ with YSZ was revealed to be higher than that of $La_{0.6}Sr_{0.4}Co_{0.8}Fe_{0.2}O_{3-\delta}$ and $Ba_{0.5}Sr_{0.5}Co_{0.8}Fe_{0.2}O_{3-\delta}$ for which the formation of impurity phases ($SrZrO_3$ or a new perovskite phase with large lattice constant) was reported to occur at 800°C and 750°C, respectively.[48] For Co-containing $Bi_{0.5}Sr_{0.5}Co_{1-y}Fe_yO_{3-\delta}$ (y = 0.2 and 0.4), on the other hand, significant amounts of the new perovskite phase were already detected in powder mixtures annealed at 750°C. Considering the relatively short period of time the samples are kept at 750°C, it is, however, not assumed that a certain degree of interfacial reactivity strongly influences the surface resistances measured on thin films of these compositions on YSZ. Finally, $Bi_{0.2}Sr_{0.8}CoO_{3-\delta}$ was found to be decomposed completely after annealing at 750°C and slow cooling to room temperature even in the absence of YSZ into, for instance, rhombohedral $Sr_6Co_5O_{15}$,[126] which was also observed to form from cubic $Bi_{0.15}Sr_{0.85}CoO_{3-\delta}$ upon heating to 590-880°C.[127]

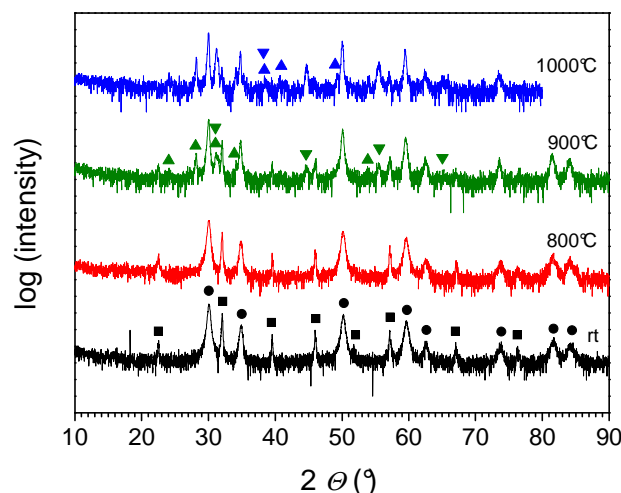*Fig. 4.5. X-ray diffractograms of powder mixtures of $Bi_{0.5}Sr_{0.5}FeO_{3-\delta}$ (■) and cubic YSZ (◆) annealed for 12 h at different temperatures. The mixtures annealed at temperatures higher than 800°C contain a phase isostructural to monoclinic ZrO_2 (▲) and a cubic perovskite phase with a large lattice constant (▼).*

The compatibility of BiSCF with MgO, used as substrate material for thin-film electrical conductivity and electrochemical polarization measurements, was investigated by annealing powder mixtures of equal volume fractions of the respective BiSCF compositions and fused MgO at 750°C for 20 h. Only in the annealed mixture containing $Bi_{0.8}Sr_{0.2}FeO_{3-\delta}$ small amounts of $Bi_{0.76}Sr_{0.23}O_{1.11}$, $BiO_{1.5}$, and probably $MgFe_2O_4$ were detected by XRD. However, electrical conductivity measurements on thin-film $Bi_{0.8}Sr_{0.2}FeO_{3-\delta}$ on MgO performed starting from 750°C and 700°C, respectively, yielded almost identical σ_{el} values proving the formation of the impurity phases to be irrelevant under the applied conditions.

4.1.3   Oxygen Nonstoichiometry

A variety of methods are described in literature which allow for a more or less reliable determination of the absolute oxygen nonstoichiometry δ of solid oxides, and several of them were tried in the present study. The reduction of BiSCF at 750°C in an atmosphere containing about 4% of hydrogen resulted in a massive mass loss suggesting evaporation of a significant amount of elemental Bi to occur, whereas reduction at lower temperatures did not yield a clear mass plateau. The determination of δ by direct or indirect iodometric titration proved not reliable due to difficulties in recognizing the titration end point in the presence of the strongly colored $[BiI_4]^-$ complex and difficulties in transferring the chlorine released upon dissolution of BiSCF in concentrated hydrochloric acid quantitatively into a separate vessel containing the KI solution, respectively. On the other hand, cerimetric titration yielded δ values for $SrFeO_{3-\delta}$ annealed under high oxygen pressure as well as $Ba_{0.5}Sr_{0.5}Co_{0.4}Fe_{0.6}O_{3-\delta}$ in good agreement with literature values. The results for the oxygen nonstoichiometry of as-prepared $Bi_{1-x}Sr_xFeO_{3-\delta}$ (x = 0.2, 0.5, and 0.8) obtained by this method are shown in Fig. 4.6 together with the δ values from neutron diffraction experiments and data taken from literature. As evident from Fig. 4.6, a significant amount of Fe^{4+} ($\sim$ 40% according to the results from cerimetric titrations) is found only in the Sr-rich composition, whereas in the other compositions, Fe exhibits almost exclusively the oxidation state 3+. The scattering of the δ values in Fig. 4.6 deduced by different authors might at least partly be due to differences in the preparation conditions.

The variation of the oxygen nonstoichiometry with temperature and oxygen partial pressure determined by thermogravimetric analyses is depicted in Fig. 4.7a for $Bi_{1-x}Sr_xFeO_{3-\delta}$ with x = 0.2, 0.5, and 0.8 together with literature data for $SrFeO_{3-\delta}$. For the two compositions with higher Bi content (x = 0.2 and 0.5), δ basically remains unchanged reflecting the low tendency of Fe to assume the oxidation state 2+. For $Bi_{0.2}Sr_{0.8}FeO_{3-\delta}$ and $SrFeO_{3-\delta}$, on the other hand, the oxygen nonstoichiometry and hence the concentration of Fe^{3+} increases upon increasing temperature and decreasing oxygen partial pressure, respectively, and $c_{V_O^{\cdot\cdot}} \propto (p(O_2))^{-n}$ with n = 0.02-0.06. The low tendency of Fe in the Bi-richer compositions to undergo a change in its oxidation state might have implications
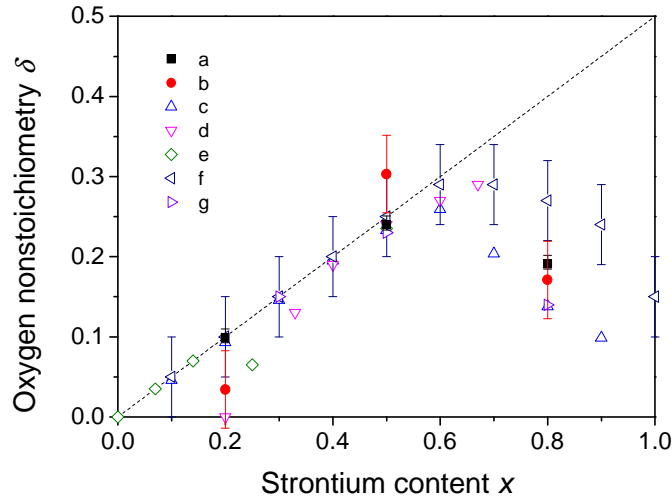
Fig. 4.6. Oxygen nonstoichiometry of as-prepared $Bi_{1-x}Sr_xFeO_{3-\delta}$ from cerimetric titration (a), neutron diffraction (b), and literature values from oxygen temperature-programmed desorption (c),[98] Mössbauer spectroscopy (d,[114] e,[128] and f[89]), and iodometric titration (g)[103] plotted versus the Sr content. The dashed line refers to δ expected if Fe exhibits exclusively the oxidation state 3+.

such as a low electronic conductivity (chapter 4.1.5), whereas the high δ values are expected to ensure a high ionic conductivity (chapter 4.4.4). From the results of TG measurements, the thermodynamic factor ω_O (chapter 2.1) can be calculated relating ionic quantities ($c_{V_O^{\cdot\cdot}}$ or c_O, $D_{V_O^{\cdot\cdot}}$) to chemical ones (C^δ, D^δ) (equation (2.17) and (4.4)). As recognizable from Fig. 4.7b, the thermodynamic factors for $Bi_{0.5}Sr_{0.5}FeO_{3-\delta}$ are approximately constant in the oxygen partial pressure range from 0.8 bar to 10^{-2} bar, but increasing at lower $p(O_2)$. Compared to the composition with intermediate Bi content, the variation of ω_O with $p(O_2)$ is more pronounced for $Bi_{0.8}Sr_{0.2}FeO_{3-\delta}$, but less distinct for $Bi_{0.2}Sr_{0.8}FeO_{3-\delta}$ and $SrFeO_{3-\delta}$
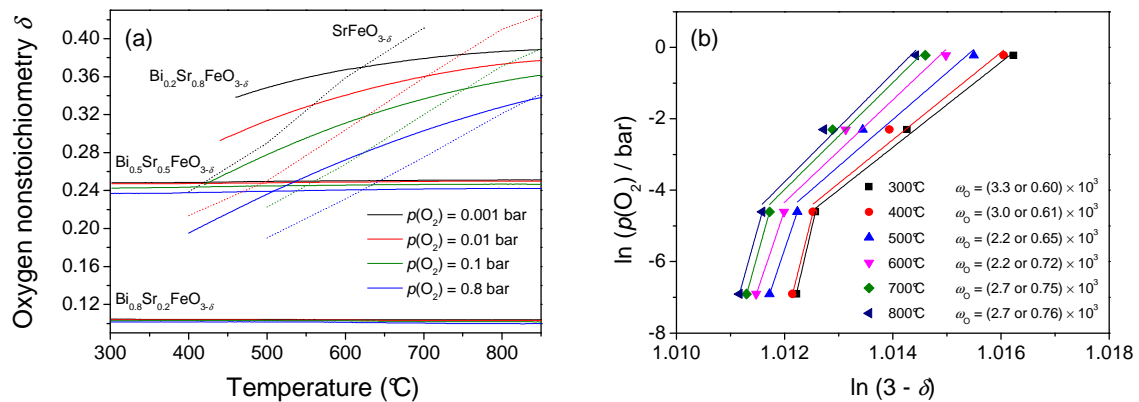
Fig. 4.7. (a) Temperature dependence of the oxygen nonstoichiometry of $Bi_{1-x}Sr_xFeO_{3-\delta}$ powders at different oxygen partial pressures. The dotted lines represent literature data for $SrFeO_{3-\delta}$[85] (b) Thermodynamic factors for powder $Bi_{0.5}Sr_{0.5}FeO_{3-\delta}$ at different temperatures calculated from the oxygen nonstoichiometry data in (a).

In the course of thermogravimetric investigations, also the stability of BiSCF in a CO_2-containing atmosphere was tested. Ba-containing perovskites are known to be susceptible to the formation of carbonates in the presence of CO_2 leading to a severe degradation of the oxygen exchange performance.[54-55] For $Bi_{1-x}Sr_xFeO_{3-\delta}$ (x = 0.2, 0.5, and 0.8), however, a maximum weight gain due to adsorption of CO_2 and/or carbonate formation of only 0.03% was observed for the composition with x = 0.8 upon heating to 850°C in a mixture of each 10 volume% of CO_2 and O_2 in N_2. This is considerably lower than the maximum weight gain of about 10% detected if $Ba_{0.5}Sr_{0.5}Co_{0.8}Fe_{0.2}O_{3-\delta}$ is heated to 1000°C in the same atmosphere.[56] Therefore, Bi-containing perovskites exhibit a lower tendency towards a formation of carbonates in agreement with the basicity of Bi^{3+} being lower than that of Ba^{2+}.

4.1.4   Oxidation Enthalpy

A factor intimately connected with the oxygen nonstoichiometry is the (standard) oxidation enthalpy ΔH_{ox}^0, that is, the enthalpy associated with the reaction

$$\tfrac{1}{2}O_2 + V_O^{\bullet\bullet} + 2M_M^x \rightleftharpoons O_O^x + 2M_M^{\bullet} \tag{4.1}$$

In the present study, the oxidation enthalpy was determined via DSC by recording the heat flow resulting from a change of the $p(O_2)$ (Fig. 4.8). The oxidation enthalpy of $Bi_{1-x}Sr_xFeO_{3-\delta}$ (x = 0.2, 0.5, and 0.8) (Fig. 4.9a) was found to increase with increasing Bi content and even exhibits a positive value for the composition with x = 0.2 (the low absolute heat flow accompanying the oxidation/reduction of this composition allowed for a reliable determination of ΔH_{ox}^0 only for an intermediate temperature of 600°C). Furthermore, the oxidation enthalpy shows no clear dependence on the temperature. The absolute value of the oxidation enthalpy of
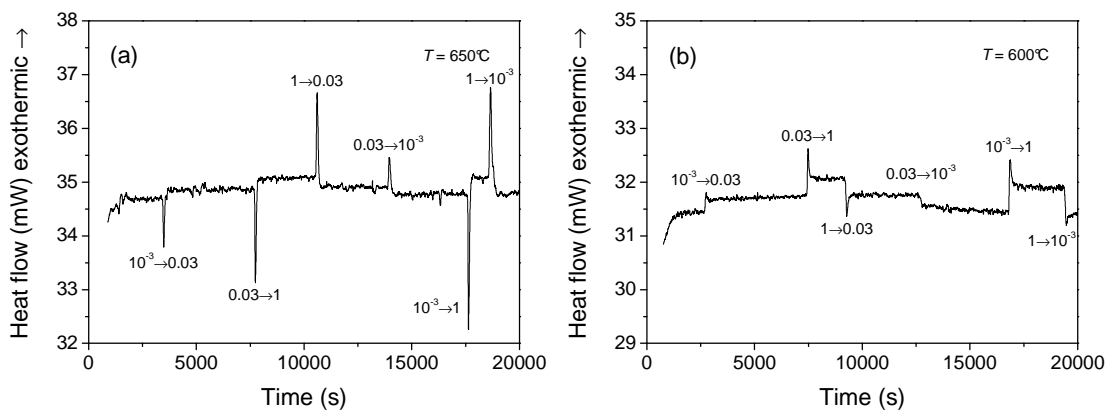

Fig. 4.8. Heat flow recorded for (a) $Bi_{0.5}Sr_{0.5}FeO_{3-\delta}$ and (b) $Bi_{0.8}Sr_{0.2}FeO_{3-\delta}$ powder upon stepwise changing the oxygen partial pressure (p(O₂) values given in bar).

BiSCF is mostly lower than that of $(La,Ba,Sr)(Mn,Co,Fe)O_{3-\delta}$ perovskites.[69, 129] The low absolute values obtained for ΔH_{ox}^0 are in line with the high δ values from TG analyses and also suggest a low coverage of the BiSCF surface with adsorbed oxygen species. Typically, the adsorption enthalpy is closely related to the oxidation enthalpy, since both processes involve the transfer of electrons from the transition metal to the respective oxygen species.[130] In alternative to DSC measurements, ΔH_{ox}^0 can also be calculated from the nonstoichiometry data according to[131]

$$\Delta H_{ox}^0 = \frac{\partial((\mu_0 - \mu_0^0)/T)}{\partial(1/T)}\bigg|_{\delta} = \frac{R\partial \ln(p(O_2)/p^0(O_2))}{2\partial(1/T)}\bigg|_{\delta} \qquad (4.2)$$

The values deduced for $Bi_{0.2}Sr_{0.8}FeO_{3-\delta}$ are presented in Fig. 4.9b; they are in good to perfect agreement with the results from DSC analyses.
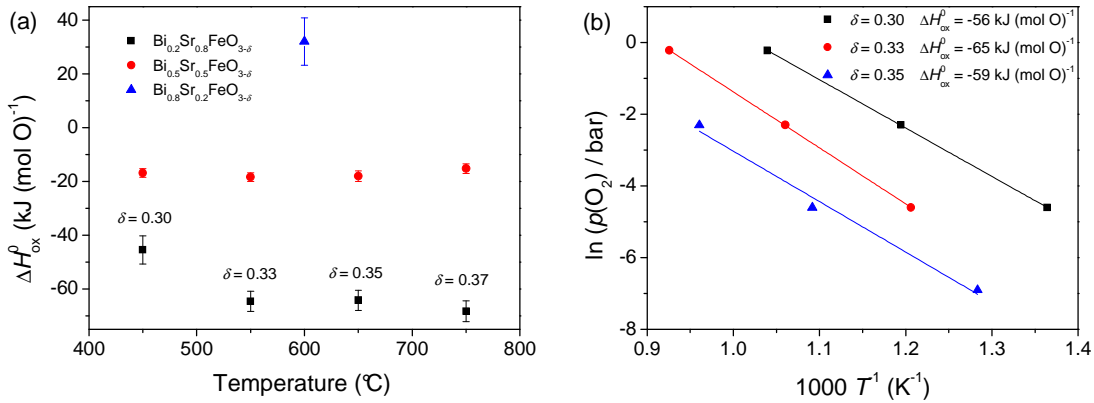
Fig. 4.9. (a) Temperature dependence of the oxidation enthalpy of $Bi_{1-x}Sr_xFeO_{3-\delta}$ powders from DSC. The δ values are given for $p(O_2) = 0.03$ bar. (b) Oxidation enthalpies of powder $Bi_{0.2}Sr_{0.8}FeO_{3-\delta}$ with different δ values calculated via equation (4.2) from the oxygen nonstoichiometry data in Fig. 4.7a.

4.1.5   Electrical Conductivity

The impedance spectra recorded on bulk samples of BiSCF basically consisted of an intercept with the real axis attributable to the electrical bulk (plus potential electrode-sample contact) resistance, which was used to calculate the electrical conductivity. The absence of a semicircle assignable to a grain boundary contribution indicates that the grain boundaries in BiSCF perovskites do not exhibit a current-blocking effect. The impedance spectra obtained for thin-film samples typically showed one semicircle, which can be represented by a parallel *RQ* circuit (with *Q* being defined by equation (3.4)). In accordance with the

simplified equivalent circuit given in ref. [132], the associated capacitance in the order of 1 pF was interpreted as a stray capacitance and the corresponding resistance ascribed to the electrical bulk resistance yielding the electrical conductivity.

Fig. 4.10 shows the temperature dependence of the electrical ($\approx$ electronic) conductivity σ_{el} measured on bulk as well as thin-film samples of BiSCF together with literature data for $SrFeO_{3-\delta}$ (due to the low phase purity of the bulk specimens (chapter 4.1.1), electrical conductivity measurements for Co-containing BiSCF were carried out solely on thin-film samples). The electrical conductivity increases with increasing Sr and Co content, respectively. Assuming electronic charge transport to happen via small polaron hopping as in many other potential SOFC cathode materials,[58-60, 62] this tendency might be ascribed to an increased concentration of Fe^{4+} and possibly Co^{2+} representing the respective electronic charge carriers. In addition, the mobility of electronic charge carriers might be decreased by the local lattice distortions observed for the Bi-rich compositions (chapter 4.1.1) leading to a smaller overlap of the oxygen 2p and iron 3d orbitals. The assumption of a thermally activated hopping conduction mechanism is consistent with the semiconductor-like behavior of the electrical conductivity found for all compositions except $Bi_{0.2}Sr_{0.8}FeO_{3-\delta}$ and $SrFeO_{3-\delta}$, where a transition from semi- to metallic conduction occurs at around 400-500°C. The activation energies deduced from the temperature dependence of σ_{el} range up to 0.45 eV for $Bi_{0.8}Sr_{0.2}FeO_{3-\delta}$ The conductivity values obtained in the present study are in acceptable to good agreement with literature values[103] and, except for $Bi_{0.2}Sr_{0.8}FeO_{3-\delta}$ lower than those of the related LSCF and BaSCF perovskites
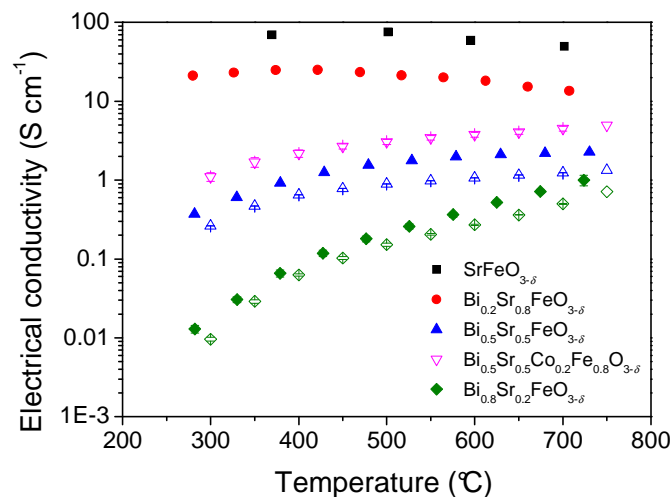

Fig. 4.10. Temperature dependence of the electrical conductivity of bulk (closed symbols) and thin-film (open symbols) BiSCF obtained in the present study and literature values for bulk $SrFeO_{3-\delta}$[133] at $p(O_2)$ = 0.2 bar. For thin films and bulk $Bi_{0.8}Sr_{0.2}FeO_{3-\delta}$ average values from two different samples are shown.

(chapter 4.5.2). Possible reasons might again be the low electronic defect concentrations and local lattice distortions in BiSCF, respectively.

The $p(O_2)$ dependence of the electrical conductivity of bulk $Bi_{1-x}Sr_xFeO_{3-\delta}$ (x = 0.2, 0.5, and 0.8) under oxidizing conditions (Fig. 4.11) is indicative of predominant p-type electronic conduction, that is, $\sigma_{el} \propto (p(O_2))^n$ with n = 0.13-0.23 ≈ ¼ in the temperature range between 500°C and 750°C. The decrease of n from 0.23 to 0.13 with increasing temperature observed for $Bi_{0.8}Sr_{0.52}FeO_{3-\delta}$, however, indicates the ionic and electronic conductivity of this composition to become increasingly similar in magnitude. At lower oxygen partial pressures, typically a conductivity plateau is reached designating the region where ionic conduction is predominant. A further discussion of the ionic conductivity values extracted from conductivity plateaus will be given in chapter 4.4.4. After ionic conductivity measurements, small amounts of a phase isostructural to tetragonal $YSr_2Cu_{2.75}Fe_{0.25}O_{6.9}$[134] were detected by XRD in the $Bi_{0.5}Sr_{0.5}FeO_{3-\delta}$ sample, which is, however, considered to exhibit an ionic conductivity similar to that of the perovskite phase (the phase decomposition is possibly reflected by the continuous linear increase of the conductivity by about 60% over a period of 3.5 days at a $p(O_2)$ of 10^{-15} bar and 750°C or the subsequent conductivity decrease upon stepwise increasing the $p(O_2)$ to 10^{-9} bar at the same temperature (see also Fig. 4.11)). On the other hand, no phase decomposition was evident for $Bi_{0.8}Sr_{0.2}FeO_{3-\delta}$ from XRD. A determination of the ionic conductivity of $Bi_{0.5}Sr_{0.5}Co_{0.2}Fe_{0.8}O_{3-\delta}$ thin-film samples appeared not to be possible due to a strong continuous (irreversible) conductivity decrease upon equilibration at 600°C in 10^{-20} bar O_2. Finally, switching from a dry to a wet measuring atmosphere of 100 ppm O_2 in N_2 did not lead to a change in the electrical conductivity of
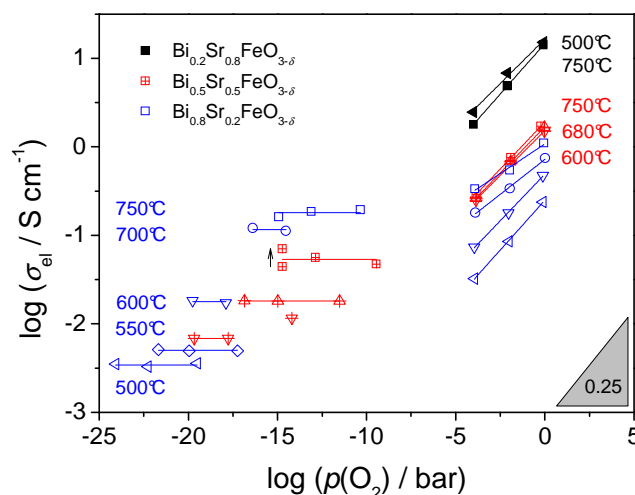

Fig. 4.11. Oxygen partial pressure dependence of the electrical conductivity of bulk $Bi_{1-x}Sr_xFeO_{3-\delta}$ at different temperatures. The arrow refers to the conductivity increase described in the text.

$Bi_{0.5}Sr_{0.5}FeO_{3-\delta}$ at 600°C indicating proton conduction to be negligible compared to the oxide ion or hole conduction in BiSCF perovskites.

4.1.6   Thermochemical Expansion Coefficient

In order to avoid the formation of cracks and sealing leaks upon thermal cycling, a SOFC needs to be built up of materials with comparable thermochemical expansion coefficient. The mean linear TEC of two representative $Bi_{1-x}Sr_xFeO_{3-\delta}$ (x = 0.5 and 0.8) compositions measured by mechanical dilatometry at two different oxygen partial pressures is depicted in Fig. 4.12 (the mean TEC has to be distinguished from the instantaneous TEC (definitions see chapter 3.2.5) the latter being significantly larger in the presence of strong chemical expansion at high temperature; the large scattering of TEC data from literature was found in many cases to be due to a lack of distinction between these two quantities). For the composition with higher Sr content, an increase in the slope of the mean-TEC curve at around 300-400°C indicates the transition from mainly thermal to thermochemical expansion corresponding to the onset of oxygen vacancy formation in accordance with the results from TG measurements (chapter 4.1.3). The mean TEC of $Bi_{0.2}Sr_{0.8}FeO_{3-\delta}$ at high temperatures, therefore, exhibits high values comparable to that of (Ba-containing) strontium ferrite (Table 4.2). The mean TEC of $Bi_{0.5}Sr_{0.5}FeO_{3-\delta}$ with nearly constant oxygen vacancy concentration is, however, close to that of the La-containing ferrite and common electrolyte materials (e.g., 10.8×10^{-6} K^{-1} for YSZ and 13.5×10^{-6} K^{-1} for CGO)[135] rendering this composition more suitable for SOFC applications.
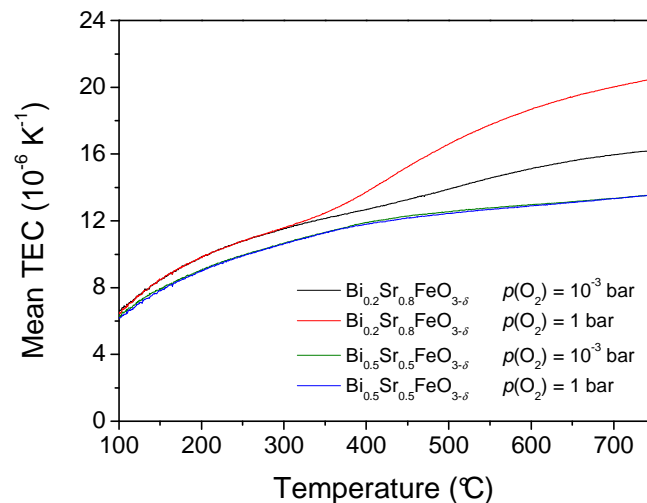

Fig. 4.12. Temperature dependence of the mean thermochemical expansion coefficient of bulk $Bi_{1-x}Sr_xFeO_{3-\delta}$ measured upon cooling at a rate of 1 K min^{-1} at different oxygen partial pressures.

Table 4.2. Mean thermochemical expansion coefficients of bulk $Bi_{1-x}Sr_xFeO_{3-\delta}$ at $p(O_2) = 10^{-3}$ bar* and 1 bar** and literature values for related perovskites at $p(O_2) = 0.2$ bar and 750°C.

	Mean TEC (10^{-6} K^{-1})
$La_{0.6}Sr_{0.4}FeO_{3-\delta}$	13[136]
$Bi_{0.5}Sr_{0.5}FeO_{3-\delta}$	14*,**
$Bi_{0.2}Sr_{0.8}FeO_{3-\delta}$	16*-21**
$SrFeO_{3-\delta}$	$\sim$ 21[137]
$Ba_{0.5}Sr_{0.5}FeO_{3-\delta}$	$\sim$ 22[138]

4.2   Characterization of Thin-Film Samples

4.2.1   Structure

Pulsed laser deposition of single-phase thin films is known to pose a great challenge if the target material contains elements with a high vapor pressure such as Bi (vapor pressure, e.g., 0.2 mbar at 650°C).[139] The evaporation of Bi from the growing film is expected to make control of the film stoichiometry difficult, and the results often strongly depend on the applied deposition conditions.[140-141] In the present study, the reproducible production of phase-pure thin films turned out to be rather demanding for some of the BiSCF compositions. Only for the Bi-poor $Bi_{0.2}Sr_{0.8}FeO_{3-\delta}$ $Bi_{0.5}Sr_{0.5}FeO_{3-\delta}$ as well as $Bi_{0.5}Sr_{0.5}Co_{0.2}Fe_{0.8}O_{3-\delta}$ exclusively single-phase perovskite films were obtained in a large number of PLD runs carried out under (near-) standard conditions (defined here as a substrate temperature of 650°C and a background oxygen pressure of 0.4 mbar) according to XRD. For the other compositions, the deposition conditions had to be adjusted carefully to avoid the formation of impurity phases, and the results were not always reproducible (which might partly be due to modifications of the technical setup over time, e.g., the exchange of heating wires and laser tube). Particularly for $BiFeO_{3-\delta}$ Volmer-Weber growth of separated islands occurred under conditions close to the standard conditions as evident from SEM and XPS analyses, and the deposition rate as an additional variable had to be modified to counter this effect.

Fig. 4.13 shows the XRD patterns of nominally 200 nm thin BiSCF films deposited on (100)-oriented YSZ single crystal substrates under the conditions listed in Table 3.2. The X-ray diffractogram of a bare YSZ substrate is displayed for comparison. Besides the main K_α and the weaker K_β reflections of (100)-oriented fluorite-type YSZ, it also contains four small peaks (at 2θ = 33.4°, 33.6°, 70.0°, and 70.6°) previously identified as artefacts from the monochromator.[129] The reflections attributable to BiSCF are consistent with the formation of phase-pure rhombohedrally distorted ($BiFeO_{3-\delta}$) or cubic (others) perovskite films. The lattice constants deducible from some of the thin-film XRD patterns are at most by 0.2% smaller than those calculated for powder samples.

The films were found to be polycrystalline except for $Bi_{0.2}Sr_{0.8}CoO_{3-\delta}$ for which only the reflection attributable to the (110) crystallographic orientation appears in the X-ray diffractogram. For polycrystalline films, the volume fractions of the different crystal orientations can be estimated from the height of the diffraction peaks after normalization to the peak intensity from powder diffraction using

$$V(hkl) = \frac{I_f(hkl)}{I_r(hkl)} \left[\sum \frac{I_f(hkl)}{I_r(hkl)} \right]^{-1} \qquad (4.3)$$
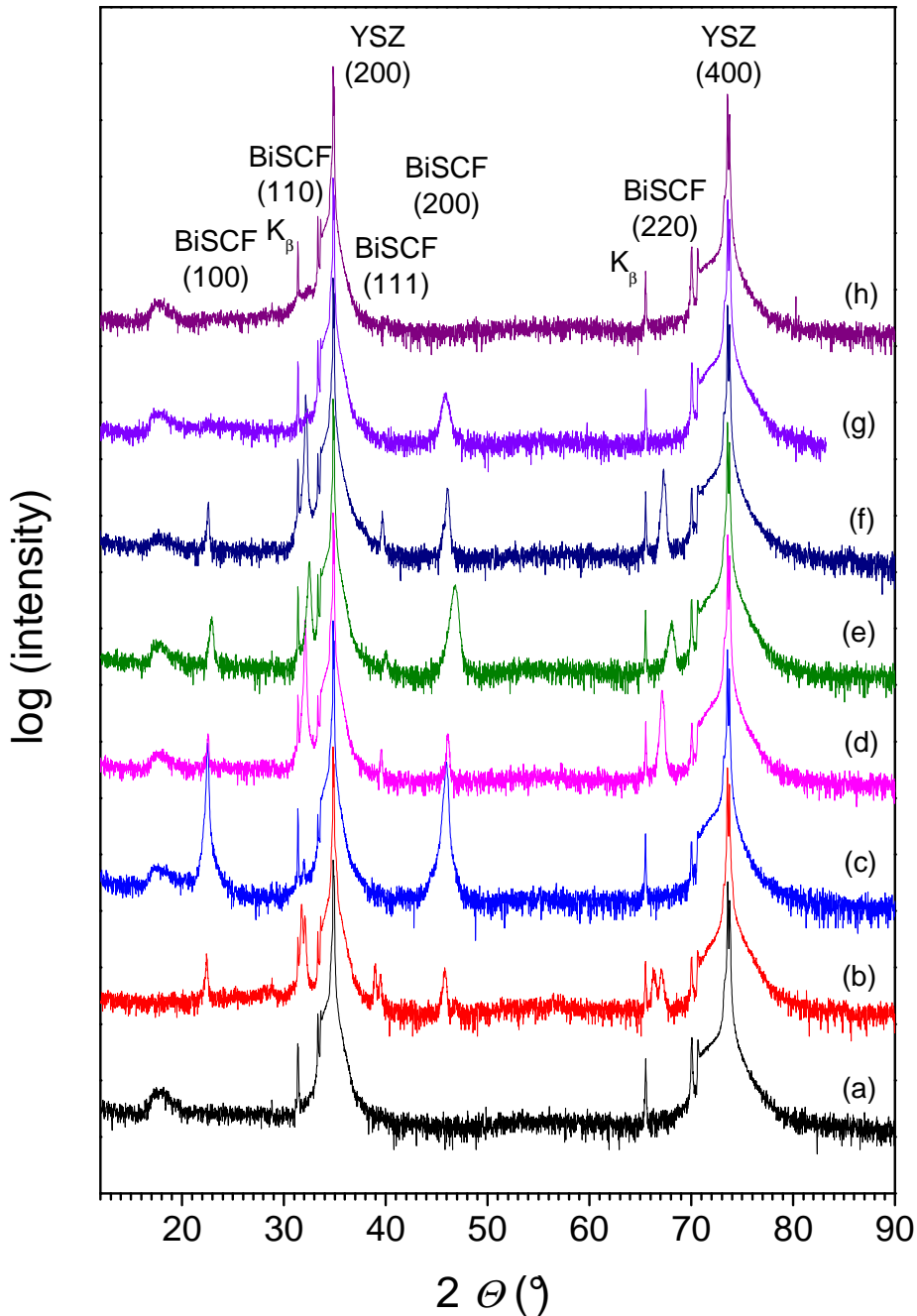
Fig. 4.13. X-ray diffractograms of nominally 200 nm thin films of (b) $BiFeO_{3-\delta}$ (c) $Bi_{0.8}Sr_{0.2}FeO_{3-\delta}$ (d) $Bi_{0.5}Sr_{0.5}FeO_{3-\delta}$ (e) $Bi_{0.2}Sr_{0.8}FeO_{3-\delta}$ (f) $Bi_{0.5}Sr_{0.5}Co_{0.2}Fe_{0.8}O_{3-\delta}$ (g) $Bi_{0.5}Sr_{0.5}Co_{0.4}Fe_{0.6}O_{3-\delta}$ and (h) $Bi_{0.2}Sr_{0.8}CoO_{3-\delta}$ on (100)-oriented YSZ single crystal substrates. The X-ray diffractogram of (a) a bare YSZ substrate is shown for comparison.

$(I_r(hkl) = I_p(hkl) / I_p(110)$, I: intensity of the (hkl) diffraction peak approximated by the peak height; the indices "f", "r", and "p" refer to "film", "relative", and "powder", respectively). From the XRD patterns in Fig. 4.13, the following crystal orientation distributions are obtained: In many cases, either the (100) orientation ($Bi_{0.8}Sr_{0.2}FeO_{3-\delta}$ and $Bi_{0.5}Sr_{0.5}Co_{0.4}Fe_{0.6}O_{3-\delta}$) or the (110) orientation ($Bi_{0.5}Sr_{0.5}FeO_{3-\delta}$

and $Bi_{0.5}Sr_{0.5}Co_{0.2}Fe_{0.8}O_{3-\delta}$) is strongly preferred and present in 93% to approximately 100% of the film. Nearly equal volume fractions of several crystal orientations are found in thin-film $BiFeO_{3-\delta}$ (39% (104), 23% (110), and 25% (006)) and $Bi_{0.2}Sr_{0.8}FeO_{3-\delta}$ (57% (100) and 39% (110)). As reported in literature, thin films of LSCF and BaSCF preferentially grow with (110) orientation if the lattice constant of YSZ of 5.14 Å deviates by about -5.6% from the face diagonal of the (pseudo)cubic perovskite unit cell.[129] If the lattice mismatch is more negative than -7.4%, the (111) orientation typically prevails. The lattice mismatch was determined to be more negative than -7.4% for all cubic BiSCF perovskites studied here except those with 20% of Bi on the A site. Therefore, preference of the (100) or (110) crystal orientation in most of the BiSCF thin films departs from the observations made for LSCF and BaSCF.

The crystal orientation distributions calculated from the diffractograms in Fig. 4.13 proved to be well reproducible in a number of PLD runs for $Bi_{1-x}Sr_{x}FeO_{3-\delta}$ (x = 0.2 and 0.5) films of the same thickness on YSZ. For $Bi_{0.2}Sr_{0.8}FeO_{3-\delta}$ and $Bi_{0.5}Sr_{0.5}Co_{0.2}Fe_{0.8}O_{3-\delta}$ also predominantly (100)-oriented films were obtained in some of the runs. Furthermore, preferential occurrence of the (110) crystal orientation was observed in two nominally 100 nm thin $Bi_{0.5}Sr_{0.5}FeO_{3-\delta}$ films from different PLD batches. In two nominally 600 nm thin films of the same composition produced in separate PLD runs, the preferred orientations are (110) and (100), respectively. A similar inconsistency has been mentioned previously for nominally 300 nm thin films of BaSCF.[129] The reason for the poor reproducibility of the film texture in some cases is not yet clear.

To investigate the influence of the deposition conditions, thin films of $Bi_{0.5}Sr_{0.5}FeO_{3-\delta}$ were deposited on (100)-oriented YSZ single crystal substrates at four different combinations of substrate temperature and background oxygen pressure. Fig. 4.14 shows that the preferred crystal orientation mainly depends on the $p(O_2)$. For films deposited at a $p(O_2)$ lower than the standard $p(O_2)$, only diffraction peaks attributed to the (100) crystallographic orientation were detected. Increasing the laser fluence (without exceeding the threshold above which damage is induced to substrate and film) also increases the volume fraction of the (100) orientation. A change of the substrate orientation from (100) to (111) (the thermodynamically stable surface orientation yielding a facet-free surface) has no significant influence on the film texture, whereas a change to the (110) substrate orientation results in a slight preference of the (111) film orientation.

The strong dependence of the film texture on $p(O_2)$ and laser fluence again indicates that the preferred crystal orientation is not solely determined by the lattice mismatch between BiSCF perovskite and substrate (which is not expected to vary significantly upon changing deposition conditions). Instead, several kinetic and thermodynamic effects have to be considered as well. On the one hand, the number of collisions between particles in the plasma plume and the background
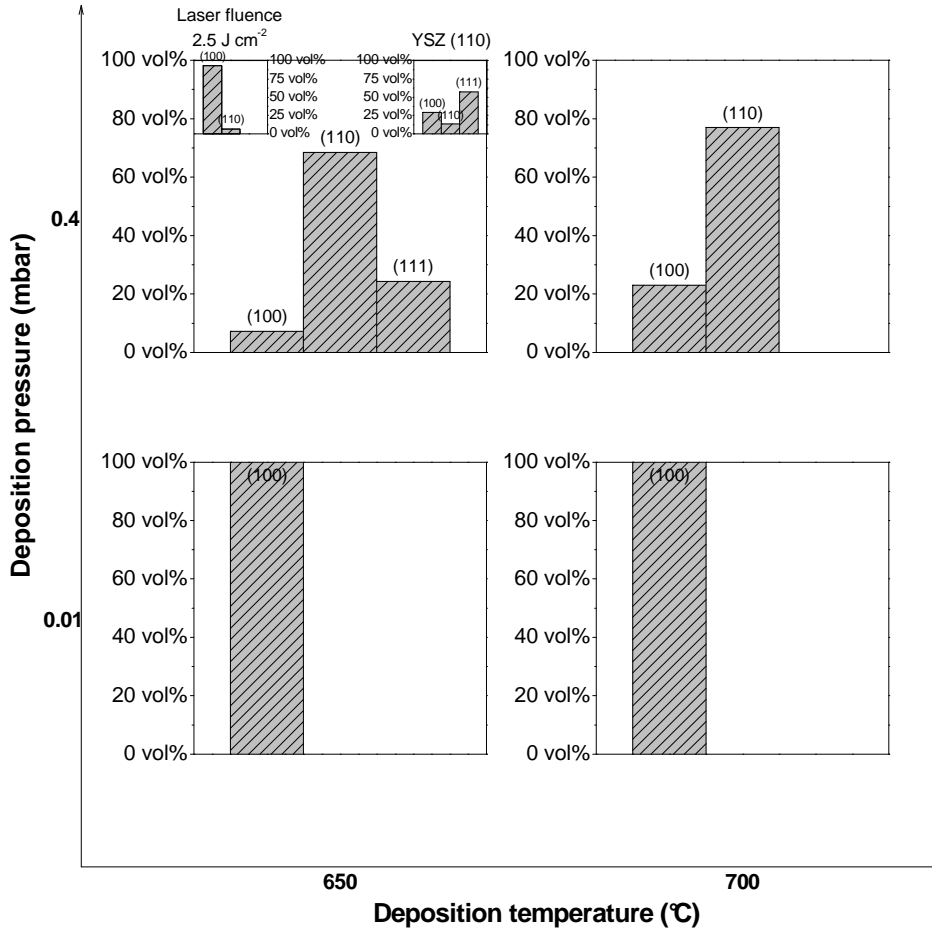
Fig. 4.14. Crystal orientation distributions deduced from the X-ray diffractograms of nominally 200 nm thin films of $Bi_{0.5}Sr_{0.5}FeO_{3-\delta}$ deposited by PLD under varying deposition conditions. The films were deposited onto (100)-oriented YSZ single crystal substrates at a laser fluence of 1.6 J cm^{-2} if not indicated otherwise.

gas is decreased at lower $p(O_2)$. This leads to an increase in the degree of ionization and the kinetic energy of the plasma particles, respectively, changing both the reactivity (in the plasma and on the substrate surface) and the diffusivity of adatoms on the substrate surface. On the other hand, lowering the $p(O_2)$ modifies thermodynamic parameters such as the surface free energies of the different crystal faces of film and substrate and the film-substrate interface free energy. The laser fluence affects the degree of plasma supersaturation and thus the instantaneous deposition rate, both coupled to numerous kinetic and thermodynamic parameters. Finally, a change of the substrate orientation might impact the growth process not only via a modification of the lattice mismatch, but also through a change of the density of steps and kinks on the substrate surface acting as thermodynamically preferred nucleation sites. A complete discussion of the complex interplay between deposition conditions and growth mode is beyond the scope of this study, and it is concentrated here on the effect of the film texture on the oxygen exchange kinetics.

A thin-film sample of each composition was annealed under EIS measurement conditions in order to test the stability inherent to the (YSZ-supported) perovskite phase as well as the stability of the perovskite film towards the YSZ substrate. XRD analyses revealed the following changes after annealing of the films for 12-20 h at 750°C in air: In the former $BiFeO_{3-\delta}$ film, only $Bi_2Fe_4O_9$ was detected. This suggests that the phase separation into $Bi_{25}FeO_{39}$ and $Bi_2Fe_4O_9$ could not be prevented via stabilization of the perovskite phase by the substrate. The absence of $Bi_{25}FeO_{39}$ might result from its low melting point of 785°C[142] causing significant evaporation from the $BiFeO_{3-\delta}$ film under the applied annealing conditions. $BiFeO_{3-\delta}$ was, therefore, found not to be suitable for thin-film electrochemical investigations (the composition is yet not assumed to exhibit fast oxygen exchange kinetics due to its low electronic conductivity of 0.64 S cm^{-1} at 870°C[143] and the presumably low ionic conductivity). In the X-ray diffractogram of thin-film $Bi_{0.8}Sr_{0.2}FeO_{3-\delta}$ recorded after annealing, two additional small peaks emerged possibly attributable to Bi_2O_3. This impurity phase is, however, not expected to alter the electrocatalytic activity of $Bi_{0.8}Sr_{0.2}FeO_{3-\delta}$ films considerably.

In the XRD pattern of an annealed $Bi_{0.5}Sr_{0.5}Co_{0.4}Fe_{0.6}O_{3-\delta}$ film, an additional reflection appeared that was not visible in the X-ray diffractogram of the as-prepared film. To identify the respective compound, grazing-incidence XRD was performed. The obtained XRD pattern revealed the presence of a considerable amount of Co_3O_4 in the film, whereas no evidence was found for the formation of the layered perovskite phase received as side product in the powder synthesis. It can not be excluded that the as-prepared film also contained a certain amount of Co_3O_4 (smaller than the XRD detection limit or present as nanocrystalline to amorphous phase) possibly resulting from sample decomposition at the particularly low deposition $p(O_2)$ (Table 3.2). Moreover, the overall catalytic activity of the film might be altered by the presence of this impurity phase.[144-146] In order to investigate this effect, thin films for EIS were prepared from a $Bi_{0.5}Sr_{0.5}FeO_{3-\delta}$ target deliberately produced to contain 20 mol% of Co_3O_4, and the formation of a two-phase film consisting of the perovskite and Co_3O_4 was confirmed by XRD. For the $Bi_{1-x}Sr_xFeO_{3-\delta}$ (x = 0.5 and 0.8) perovskites and $Bi_{0.2}Sr_{0.8}CoO_{3-\delta}$ no significant changes in film texture or composition after annealing were evident from the X-ray diffractograms. Furthermore, no XRD reflections were observed for any of the annealed films indicating that a reaction had occurred between film and substrate.

The texture of nominally 200 nm thin BiSCF perovskite films deposited on (100)-oriented MgO single crystal substrates largely differs from that of the YSZ-supported films discussed above. For most of the studied compositions, including $SrFeO_{3-\delta}$ the (100) orientation is the preferred or even exclusive crystal orientation in the films. The $Bi_{0.5}Sr_{0.5}Co_{0.4}Fe_{0.6}O_{3-\delta}$ films, however, contained a significant amount of Co_3O_4 in addition to the (100)-oriented perovskite. Furthermore, phase-pure $Bi_{0.8}Sr_{0.2}FeO_{3-\delta}$ films were received only under modified

deposition conditions (Table 3.2) and showed preference of the (110) orientation (eventually, the (100) reflection was buried by the bump shifted to slightly higher Bragg angles for MgO). Previously, the (100) crystal orientation has been identified as the preferred orientation of BaSCF thin films on (100)-oriented MgO single crystal substrates.[56, 147] This was suggested to be due to the similar magnitude of the lattice constants of halite-type MgO (4.21 Å)[148] and BaSCF. The above-mentioned results, nevertheless, imply that the true situation might be more complex. X-ray analyses of the thin films on MgO after the electrical conductivity and electrochemical polarization measurements (with suitable sealing layer, see chapter 4.4.1) did not reveal any significant changes.

4.2.2   Morphology

As revealed by SEM, the surface of thin films deposited on YSZ is in most cases composed of small crystallites (average size $\sim$ 200 nm) with faceted surface and apparently random orientation (Fig. 4.15). The surface of Bi-poor $Bi_{0.2}Sr_{0.8}FeO_{3-\delta}$ thin films also exhibits smoother areas in between the crystallite regions containing small cracks (barely visible at the resolution given in Fig. 4.15). These cracks might be caused by the strong thermochemical expansion of this composition (chapter 4.1.6), but are not likely to extend through the entire film thickness and should, therefore, not influence the surface reaction to a large extent. It is not clear whether the blurred surface morphology of $Bi_{0.8}Sr_{0.2}FeO_{3-\delta}$ films (Fig. 4.15) is intrinsic or rather a measurement artifact resulting from strong electrostatic charging of the material with particularly low electronic conductivity (chapter 4.1.5). The grains detected on the surface of $Bi_{0.5}Sr_{0.5}Co_{0.4}Fe_{0.6}O_{3-\delta}$ films (Fig. 4.15e) are comparatively small ($\sim$ 30 nm size on average). This might be due to the lower deposition oxygen pressure (Table 3.2). Thin films, for example, of LSCF were found to be pore-free only if deposited at low $p(O_2)$.[149] It was suggested that, at low $p(O_2)$, the particles in the plasma plume are not sufficiently decelerated or scattered to form stable nanoclusters which lead to a porous film morphology or high surface roughness.[149] A definite explanation can, however, not be given due to the various implications of any change of the PLD parameters (chapter 4.2.1). The surface of $Bi_{0.2}Sr_{0.8}CoO_{3-\delta}$ films (Fig. 4.15f), deposited at a comparatively low substrate temperature (Table 3.2), shows a more lamellar morphology giving rise to a high surface roughness. It has to be noted that thin films of this composition possess only low adherence to the substrate and can be removed easily, for instance, by wiping with cotton swabs. A low adherence was reported previously for porous LSCF films deposited at high $p(O_2)$ and low temperature.[149] Thin films of $BiFeO_{3-\delta}$ (SEM images not shown) display a slightly perforated morphology indicating that even after extensive variation of PLD parameters, Volmer-Weber-type growth could not fully be prevented.

No pores were detected in the bulk of a $Bi_{0.5}Sr_{0.5}FeO_{3-\delta}$ film by SEM of a thin-film cross section (Fig. 4.16a). Thus, the bulk of BiSCF films is expected to be dense

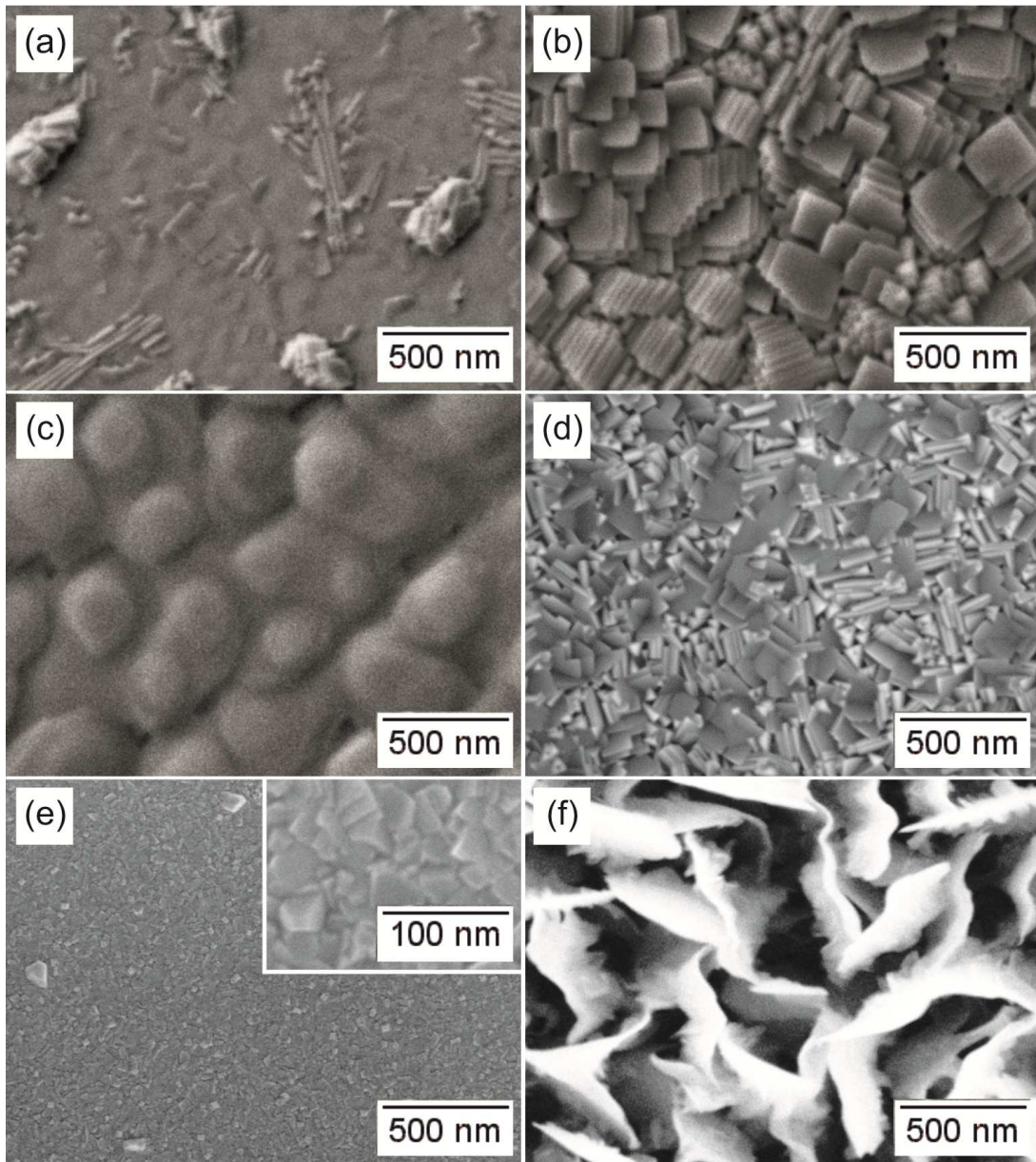Fig. 4.15. Typical SEM images of the surface of nominally 200 nm thin films of (a) $Bi_{0.2}Sr_{0.8}FeO_{3-\delta}$ (b) $Bi_{0.5}Sr_{0.5}FeO_{3-\delta}$ (c) $Bi_{0.8}Sr_{0.2}FeO_{3-\delta}$ (d) $Bi_{0.5}Sr_{0.5}Co_{0.2}Fe_{0.8}O_{3-\delta}$ (e) $Bi_{0.5}Sr_{0.5}Co_{0.4}Fe_{0.6}O_{3-\delta}$ and (f) $Bi_{0.2}Sr_{0.8}CoO_{3-\delta}$ on (100)-oriented YSZ single crystal substrates.

(except for $BiFeO_{3-\delta}$ and possibly $Bi_{0.2}Sr_{0.8}CoO_{3-\delta}$) despite the pronounced surface roughness. TEM analyses performed on another $Bi_{0.5}Sr_{0.5}FeO_{3-\delta}$ thin film (Fig. 4.16b) confirmed the investigated cross-sectional area to be dense and well-crystallized, and no indications for the presence of an amorphous surface layer were found. To generate Fig. 4.16, a lamella was cut out from the samples using a focused ion beam. FIB etching is the method of choice to study film cross sections, whereas fracturing of thin films mostly results in a coarse breaking edge creating misleading contrast in the SEM images.[149] A number of fractured samples was investigated, nevertheless, by SEM to determine the actual film thickness.

Thickness values of about 170 nm ($SrFeO_{3-\delta}$), 80 nm ($Bi_{0.5}Sr_{0.5}FeO_{3-\delta}$), and 90 nm ($Bi_{0.5}Sr_{0.5}Co_{0.2}Fe_{0.8}O_{3-\delta}$) were obtained for films deposited with a nominal thickness of 200 nm onto MgO single crystal substrates. The thickness of the $Bi_{0.5}Sr_{0.5}FeO_{3-\delta}$ film on MgO deduced from the fractured sample is considerably lower than the thickness of 150 nm derived via FIB etching from a film of the same composition with nominally identical thickness on YSZ (Fig. 4.16a). A certain fluctuation of the actual film thickness was also evident from the variations in the XRD peak intensity observed for films with nominally identical thickness and composition. Possible reasons might be changes in the laser plume shape or target-to-substrate distance or thin material layers deposited on the inside of the PLD chamber window.
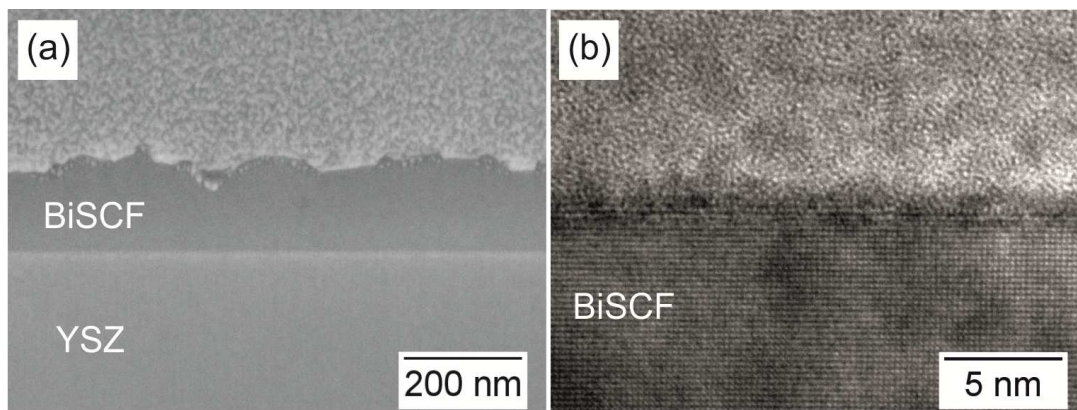

Fig. 4.16. (a) SEM image of a cross section of a nominally 200 nm thin film of $Bi_{0.5}Sr_{0.5}FeO_{3-\delta}$ deposited under standard conditions onto a (100)-oriented YSZ single crystal substrate. (b) TEM image of a cross section of another nominally 200 nm thin film of $Bi_{0.5}Sr_{0.5}FeO_{3-\delta}$ deposited at 650°C and a background oxygen pressure of 0.01 mbar onto a (100)-oriented YSZ single crystal substrate. The surface of the films in (a) and (b) was covered by a layer of Pt and amorphous C, respectively.

The increase in surface area due to surface roughening is considered negligible as opposed to the increase in surface area caused by the porosity extending through the film thickness deliberately induced in the conventional screen-printed electrodes. However, the question arises whether the presence of a large number of low-coordinated surface sites such as steps and kinks visible in some of the SEM images affects the surface oxygen exchange kinetics. It is well known that such defects can have strong, albeit not necessarily favorable, influence on adsorption processes and catalytic reactions on metal surfaces.[150] For example, the dissociative adsorption of oxygen on stepped Pt surfaces (typically surfaces with high Miller indices) preferentially occurs at surface steps. This might either decelerate the overall oxygen reduction due to the strong bonding of oxygen at these sites or, in the case of a sufficiently large terrace width providing a large enough reactive area, not cause any noticeable effect.

The surface of $Bi_{0.5}Sr_{0.5}FeO_{3-\delta}$ films deposited at low $p(O_2)$ shows a comparatively smooth morphology disturbed only by a small number of cracks (e.g., Fig. 4.17a) (the reason for the lower surface roughness might be the same as discussed before for $Bi_{0.5}Sr_{0.5}Co_{0.4}Fe_{0.6}O_{3-\delta}$ films deposited at low $p(O_2)$). EIS measurements on these films are, therefore, suited to elucidate the role of surface defects related to the morphology of the film surface. The modification of deposition temperature or substrate orientation, on the other hand, does not change the grain size or surface roughness significantly, whereas an increase of the laser fluence results in a slightly smoother surface morphology. Thin films of $Bi_{0.5}Sr_{0.5}FeO_{3-\delta}$ deliberately produced to contain 20 mol% of Co_3O_4 also display smoother surface areas in between the crystallite regions (Fig. 4.17b), but a clear distinction of the different phases is not possible from the SEM images.
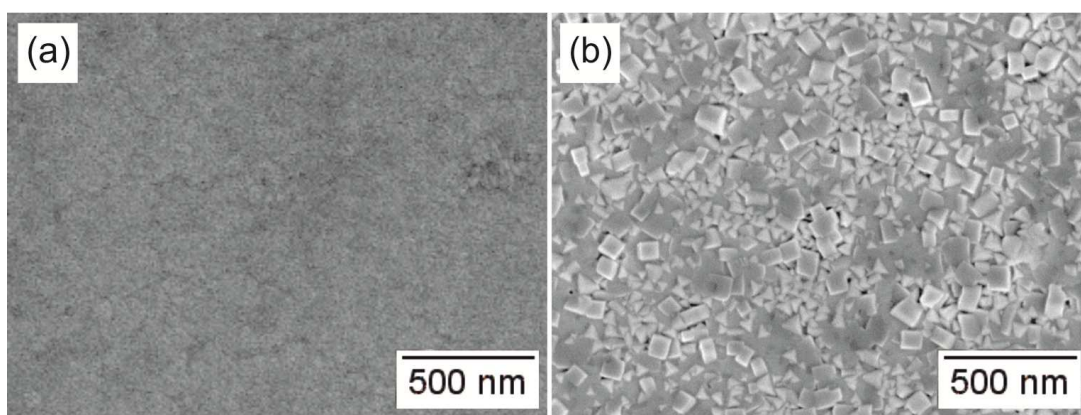

Fig. 4.17. SEM images of the surface of nominally 200 nm thin films of (a) pure $Bi_{0.5}Sr_{0.5}FeO_{3-\delta}$ deposited at 650°C and a background oxygen pressure of 0.01 mbar onto a (100)-oriented YSZ single crystal substrate and (b) $Bi_{0.5}Sr_{0.5}FeO_{3-\delta}$ containing 20 mol% of Co_3O_4 deposited under standard conditions onto a (100)-oriented YSZ single crystal substrate.

4.2.3 Quantitative Composition

The actual cation stoichiometry of BiSCF thin films was studied by ICP-OES, EDX, and XPS. From ICP-OES measurements, cation stoichiometries were determined for films of the two compositions with intermediate and low Bi content (Table 4.3) in good agreement with those of the as-prepared powders. The results from ICP-OES revealed that neither during the powder preparation nor during the film deposition, a significant loss of Bi due to evaporation had occurred. Therefore, the application of an excess of Bi in the synthesis of Bi-containing powders and targets for PLD reported by some authors (e.g., ref. [151-153]) appears not to be necessary. However, ICP-OES measurements require a relatively large amount of sample to obtain a sufficient signal intensity and thus could not be performed routinely. In Table 4.3, the results of EDX analyses are shown which yielded reasonable values

for the cation stoichiometry of thin films. Furthermore, the data from XPS measurements on as-prepared thin films are given indicating that the cationic composition on the film surface is close to that in the bulk of the films. No clear indications for an enrichment of Sr or the presence of Si impurities on the film surface were found observed previously for $(La,Sr)(Mn,Co,Fe)O_{3-\delta}$[154-157] and expected to be responsible for the degradation of the oxygen exchange performance (chapter 4.3.1). For a $BiFeO_{3-\delta}$ thin-film sample prepared under the conditions listed in Table 3.2, also peaks attributable to the YSZ substrate were detected by XPS signifying that full densification of the film had not been achieved.

Table 4.3. Quantitative (surface) composition of as-prepared thin films of BiSCF on (100)-oriented YSZ single crystal substrates from ICP-OES, EDX, and XPS.

Targeted composition	Actual composition according to ICP-OES[*]
$Bi_{0.5}Sr_{0.5}FeO_{3-\delta}$	$(Bi_{0.48}Sr_{0.52})_{1.01(1)}FeO_{3-\delta}$
	$((Bi_{0.50}Sr_{0.50})_{1.03}FeO_{3-\delta})$
$Bi_{0.2}Sr_{0.8}FeO_{3-\delta}$	$(Bi_{0.18}Sr_{0.82})_{1.00(2)}FeO_{3-\delta}$
	$((Bi_{0.19}Sr_{0.81})_{1.00(1)}FeO_{3-\delta})$
Targeted composition	**Actual composition according to EDX**
$BiFeO_{3-\delta}$	$Bi_{0.93(7)}FeO_{3-\delta}$
$Bi_{0.8}Sr_{0.2}FeO_{3-\delta}$	$(Bi_{0.80(3)}Sr_{0.20(3)})_{1.04(4)}FeO_{3-\delta}$
$Bi_{0.5}Sr_{0.5}FeO_{3-\delta}$	$(Bi_{0.47}Sr_{0.53})_{0.98(1)}FeO_{3-\delta}$
$Bi_{0.2}Sr_{0.8}FeO_{3-\delta}$	$(Bi_{0.23}Sr_{0.77})_{1.12(1)}FeO_{3-\delta}$
$Bi_{0.2}Sr_{0.8}CoO_{3-\delta}$	$(Bi_{0.19(2)}Sr_{0.81(2)})_{1.03(6)}CoO_{3-\delta}$
Targeted composition	**Actual (surface) composition according to XPS[**]**
$BiFeO_{3-\delta}$	$BiFeO_{3-\delta}$
$Bi_{0.8}Sr_{0.2}FeO_{3-\delta}$	$Bi_{0.76}Sr_{0.24}FeO_{3-\delta}$
$Bi_{0.5}Sr_{0.5}FeO_{3-\delta}$	$Bi_{0.48}Sr_{0.52}FeO_{3-\delta}^{***}$
$Bi_{0.2}Sr_{0.8}FeO_{3-\delta}$	$Bi_{0.27}Sr_{0.73}FeO_{3-\delta}$
$Bi_{0.5}Sr_{0.5}Co_{0.2}Fe_{0.8}^{o}{}_{3-\delta}$	$Bi_{0.48}Sr_{0.52}Co_{0.19}Fe_{0.81}^{o}{}_{3-\delta}$

[*]results for powders given in parentheses

[**]normalized to a 1:1 ratio of A and B cations, errors not known

[***]additionally normalized to the composition of the powder from XPS

4.3 EIS Measurements on Thin-Film Microelectrodes

4.3.1 Interpretation of Microelectrode Impedance Spectra

A typical impedance spectrum measured on a BiSCF microelectrode is shown in Fig. 4.18. The spectrum exhibits an axis intercept at high frequencies and two semicircles at intermediate and low frequencies. BiSCF microelectrode spectra, therefore, qualitatively agree with typical impedance spectra recorded on LSCF and BaSCF microelectrodes.[10, 14] The equivalent circuit used to evaluate LSCF and BaSCF microelectrode spectra is depicted in Fig. 4.18 as well. It was derived from a physical model for charge carrier transport in mixed-conducting electrodes[158] assuming that the electrode material has a high ionic and electronic conductivity and that the overall transport is limited by interfacial processes.[34] The high-frequency axis intercept R_{HF} was attributed to the ion transport resistance of the electrolyte. The resistance R_{IF} and the capacitance C_{IF} (related to the constant phase element Q_{IF} in Fig. 4.18 according to equation (3.4)) associated with the intermediate-frequency semicircle were ascribed to oxide ion transfer across the electrode-electrolyte boundary. The strongly $p(O_2)$-dependent resistance R_{LF} corresponding to the diameter of the low-frequency semicircle was assigned to the oxygen exchange reaction at the electrode surface, and the respective large capacitance C_{LF} was interpreted as a so-called "chemical capacitance" arising from oxygen stoichiometry gradients due to readjustment of the oxygen content in the electrode bulk.
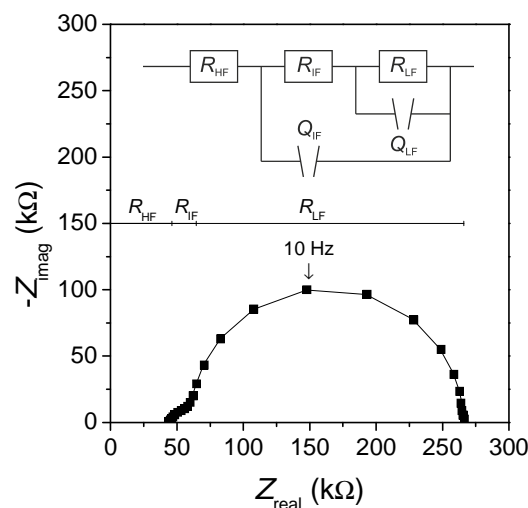

Fig. 4.18. Typical impedance spectrum of a 150 nm thin $Bi_{0.5}Sr_{0.5}FeO_{3-\delta}$ microelectrode with 60 μm in diameter on a YSZ single crystal substrate at 750°C and $p(O_2)$ = 0.2 bar. The solid line represents the best fit obtained with the equivalent circuit shown in the inset.[34]

Applying the equivalent circuit in Fig. 4.18, the resistance and capacitance values listed in Table 4.4 were deduced from BiSCF microelectrode spectra measured at 750°C and a $p(O_2)$ of 0.2 bar. The results for $Bi_{0.5}Sr_{0.5}FeO_{3-\delta}$ were acquired from films produced under standard PLD conditions unless indicated otherwise. Unfortunately, microelectrode preparation proved not to be successful for $Bi_{0.2}Sr_{0.8}CoO_{3-\delta}$ as the high surface roughness of the films (chapter 4.2.2) did not allow for the application of a dense photoresist layer. The low-frequency/surface resistance values in Table 4.4 were found to decrease with increasing Sr and Co content. The surface resistance of BiSCF is by a factor of 2-3 higher than that extracted from microelectrode measurements on BaSCF perovskites with identical Sr and Co content,[56] but by a factor of 2-3 lower than that obtained on microelectrodes of the related LSCF members.[10] This implies an improvement of the oxygen exchange kinetics if La^{3+} is substituted by Bi^{3+}, although the excellent oxygen exchange performance of Ba-containing perovskites can not be achieved.

Table 4.4. Average resistances and capacitances measured on 150 nm thin BiSCF microelectrodes with 60 μm in diameter on YSZ single crystal substrates at 750°C and $p(O_2)$ = 0.2 bar. For each composition, EIS measurements were conducted on each 10 microelectrodes on 5 ($Bi_{0.5}Sr_{0.5}FeO_{3-\delta}$) or 2 (other compositions) different samples.

	R_{HF}	R_{IF}	C_{IF}	R_{LF}	C_{LF}
	(kΩ)	(Ω cm²)	(10^{-5} F cm⁻²)	(Ω cm²)	(F cm⁻³)
$Bi_{0.2}Sr_{0.8}FeO_{3-\delta}$	18 ± 1	-	-	3.8 ± 0.5	$(1.0 \pm 0.1) \times 10^3$
$Bi_{0.5}Sr_{0.5}FeO_{3-\delta}$	42 ± 3	0.91 ± 0.13	41 ± 9	3.5 ± 0.9	$(1.1 \pm 0.1) \times 10^2$
$Bi_{0.8}Sr_{0.2}FeO_{3-\delta}$	77 ± 3	6.5 ± 0.6	1.6 ± 0.3	9.7 ± 0.3	1.5×10^1
$Bi_{0.5}Sr_{0.5}Co_{0.2}Fe_{0.8}O_{3-\delta}$	14 ± 4	-	-	1.3 ± 0.3	$(6.0 \pm 1.3) \times 10^2$
$Bi_{0.5}Sr_{0.5}Co_{0.4}Fe_{0.6}O_{3-\delta}$	7.1 ± 0.2	-	-	1.5 ± 0.5	$(1.5 \pm 0.2) \times 10^3$

The low-frequency (chemical) capacitance from microelectrode measurements appears to be smaller for BiSCF than for LSCF ($C_{LF} = 1.3 \times 10^3$ F cm⁻³ for $La_{0.6}Sr_{0.4}FeO_{3-\delta}$ and 1.1×10^3 F cm⁻³ for $La_{0.6}Sr_{0.4}Co_{0.2}Fe_{0.8}O_{3-\delta}$ at 750°C in air)[10] and BaSCF ($C_{LF} = 1.8 \times 10^3$ F cm⁻³ for $Ba_{0.5}Sr_{0.5}FeO_{3-\delta}$ and 1.9×10^3 F cm⁻³ for $Ba_{0.5}Sr_{0.5}Co_{0.4}Fe_{0.6}O_{3-\delta}$ at 750°C and $p(O_2)$ = 0.2 bar)[56] if compositions with similar Sr and Co content are considered. In addition, the chemical capacitance of BiSCF microelectrodes exhibits a particularly strong dependence on the electrode composition, that is, increases by one to two orders of magnitude with increasing amount of Sr and Co, respectively. The chemical capacitance of thin-film microelectrodes can be compared to the chemical capacitance C^{δ} determined from TG measurements on bulk samples (chapter 4.1.3) using

$$C^{\delta} = \frac{4F^2}{V_m} \frac{\partial c_0}{\partial \mu_0} = \frac{4F^2 c_0}{V_m RT \omega_0} \tag{4.4}$$

(V_m: molar volume). For bulk BiSCF, C^δ was calculated to 2.8×10^3 F cm^{-3} for Bi$_{0.2}$Sr$_{0.8}$FeO$_{3-\delta}$, 4.3×10^2 F cm^{-3} for Bi$_{0.5}$Sr$_{0.5}$FeO$_{3-\delta}$ and 1.8×10^2 F cm^{-3} for Bi$_{0.8}$Sr$_{0.2}$FeO$_{3-\delta}$ at 750°C and a $p(O_2)$ of 0.2 bar. Thus, the chemical capacitance of the bulk materials is by a factor of 3-12 larger than that of thin films. As mentioned in literature, a similar discrepancy exists between the bulk and thin-film chemical capacitance of La$_{0.6}$Sr$_{0.4}$CoO$_{3-\delta}$[4] La$_{0.6}$Sr$_{0.4}$Co$_{0.8}$Fe$_{0.2}$O$_{3-\delta}$[34] and SrTi$_{1-x}$Fe$_x$O$_{3-\delta}$ (x = 0.35 and 0.5)[159] the former being by a factor of up to 7 higher. Possible reasons were suggested to be modifications of the defect chemistry due to mechanical stress in the film or deviations in the cation stoichiometry, charge displacement at the film surface or the film-substrate interface or problems with current collection.[4] A good agreement between bulk and thin-film chemical capacitance, in contrast, was reported for (Ba$_{0.5}$Sr$_{0.5}$)$_{1.04}$Co$_{0.8}$Fe$_{0.2}$O$_{3-\delta}$[56] The possible influence of ineffective current collection/sheet resistance in thin-film electrodes on the chemical capacitance will be discussed further in chapter 4.3.2.

For some of the compositions, a distinct intermediate-frequency semicircle was solely visible in impedance spectra measured at a $p(O_2)$ lower than 0.2 bar (chapter 4.3.6). Instead, the only semicircle detected at ambient $p(O_2)$ appeared to be slightly distorted on the high-frequency side. The intermediate-frequency capacitance of Bi$_{0.5}$Sr$_{0.5}$FeO$_{3-\delta}$ was found to be more than one order of magnitude higher than the interfacial capacitance of La$_{0.6}$Sr$_{0.4}$FeO$_{3-\delta}$ (2.0×10^{-5} F cm^{-2} at 750°C and $p(O_2)$ = 0.2 bar as extrapolated from 650°C)[10] and Ba$_{0.5}$Sr$_{0.5}$FeO$_{3-\delta}$ (4.0×10^{-5} F cm^{-2} at 750°C and ambient $p(O_2)$).[14] Also, the electrode diameter, temperature, and $p(O_2)$ dependence of R_{IF} and C_{IF} showed a strong deviation from that expected for an interfacial process (chapter 4.3.4 to chapter 4.3.6). The chemical stability of Co-free BiSCF towards YSZ is higher than that of LSCF and BaSCF (chapter 4.1.2), which makes the formation of an insulating interlayer less probable. Finally, the introduction of a nominally 100 nm thin interlayer of 10 mol% CGO between YSZ and Bi$_{0.5}$Sr$_{0.5}$FeO$_{3-\delta}$ microelectrodes did not modify the impedance (Fig. 4.19) in contrast to what has been reported for LSCF.[34] All the above-mentioned observations indicate that the physical origin of the intermediate-frequency semicircle in BiSCF microelectrode spectra is different from an interfacial process.

Furthermore, the high-frequency axis intercept measured on BiSCF microelectrodes is up to more than one order of magnitude larger than that obtained for the La- and Ba-containing perovskites (3.3 kΩ for La$_{0.6}$Sr$_{0.4}$Co$_{0.8}$Fe$_{0.2}$O$_{3-\delta}$ microelectrodes with 60 μm in diameter[34] or 2.3 kΩ extrapolated from 700°C for a Ba$_{0.25}$Sr$_{0.75}$Co$_{0.8}$Fe$_{0.2}$O$_{3-\delta}$ microelectrode with 100 μm in diameter[56] at 750°C and $p(O_2)$ = 0.2 bar). From electrical conductivity measurements on two different bare YSZ substrates, the ionic conductivity σ_{YSZ} of YSZ was determined to $(1.7 \pm 0.1) \times 10^{-2}$ S cm^{-1} at 750°C. Using the spreading resistance formula[160]
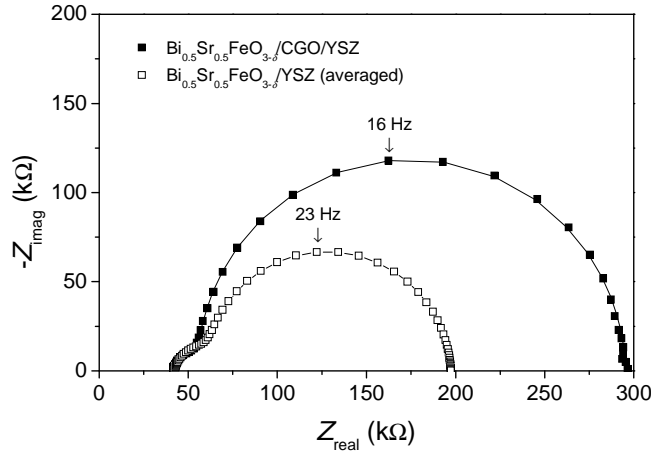
Fig. 4.19. Impedance spectrum of a 150 nm thin $Bi_{0.5}Sr_{0.5}FeO_{3-\delta}$ microelectrode with 60 µm in diameter with CGO interlayer between the electrode and the YSZ single crystal substrate at 750°C and $p(O_2)$ = 0.2 bar. The solid line represents the best fit obtained with the equivalent circuit in Fig. 4.18. For comparison, the averaged impedance spectrum of a $Bi_{0.5}Sr_{0.5}FeO_{3-\delta}$ microelectrode with the same dimensions without interlayer (simulated with the equivalent circuit in Fig. 4.18 and the experimental values in Table 4.4 using ZView) is shown.

$$\sigma_{YSZ} = \frac{1}{2R_{HF}d_{el}} \qquad (4.5)$$

(d_{el}: electrode diameter), a resistance of the YSZ electrolyte of 5 kΩ can be calculated for the experimental conditions given in Table 4.4 in fair agreement with R_{HF} for LSCF and BaSCF, but (significantly) lower than the high-frequency intercept of BiSCF microelectrodes. This, as well as the unusual electrode diameter, temperature, and $p(O_2)$ dependence of R_{HF} (chapter 4.3.4 to chapter 4.3.6), suggests that further processes come into play in BiSCF microelectrode impedance measurements both giving rise to the intermediate-frequency semicircle and increasing the high-frequency axis intercept.

EIS measurements on LSM microelectrodes yielded an intermediate-frequency semicircle due to slow transport of oxide ions through the electrode bulk,[11] but the ionic conductivity of BiSCF (chapter 4.4.4) is considerably higher than that of LSM ($\sim 3 \times 10^{-8}$ S cm^{-1} at 800°C in air)[11] making the appearance of such a semicircle rather unlikely in the present case. The electronic conductivity of BiSCF, in contrast, is comparatively low (chapter 4.1.5). A low electronic conductivity can lead to significant sheet resistance in thin-film electrodes, for example, cause a laterally nonuniform electrical potential distribution within the electrode. The conductivity threshold below which sheet resistance becomes significant depends on the electrode thickness, the current-collector geometry, and the kinetic parameters of other processes involved, for instance, the surface oxygen exchange.

A modification of the apparent surface oxygen exchange resistance owing to sheet resistance has been reported for linear patterned electrode films of $La_{0.8}Sr_{0.2}MnO_{3\pm\delta}$[7] and continuous electrode layers of $La_{0.6}Sr_{0.4}Co_{0.2}Fe_{0.8}O_{3-\delta}$[44] Recently, Lynch et al. developed a two-dimensional empirical numerical model to simulate the effect of sheet resistance in thin-film mixed-conducting electrodes.[107] According to their simulations, an increased high-frequency axis intercept as well as an additional semicircle at intermediate frequencies can emerge as a consequence of high sheet resistance.

From the thin-film electrical conductivity in Fig. 4.10, the electronic transport resistance of a 150 nm thin stripe of $Bi_{0.5}Sr_{0.5}FeO_{3-\delta}$ with 30 μm in length and width was estimated to 50 kΩ at 750°C in good agreement with R_{IF} of a $Bi_{0.5}Sr_{0.5}FeO_{3-\delta}$ microelectrode with 60 μm in diameter at the same temperature. Within the series of BiSCF perovskites with identical occupation of A and B site, respectively, all three resistive contributions to the microelectrode impedance spectra mostly decrease with increasing electrical conductivity. Furthermore, R_{IF} exhibits an activation energy of the inverse quantity (Table 4.7) and a $p(O_2)$ dependence (Table 4.8) comparable to the activation energy and $p(O_2)$ dependence of the electrical conductivity (chapter 4.1.5). All these observations suggest that sheet resistance exerts a significant influence on BiSCF microelectrode impedance measurements. To verify this hypothesis, the numerical model of Lynch et al.[107] was applied to the present system of BiSCF microelectrodes, and the results are given in the following chapter.

A final comment has to be made regarding degradation during EIS measurements on BiSCF microelectrodes. Degradation refers to a continuous increase in the surface resistance upon increasing duration of annealing at elevated temperature and was observed previously for related perovskite-type SOFC cathode materials (e.g., ref. [10, 14]). Possible reasons were suggested to be Sr[154, 157] or La[161] enrichment on the cathode surface or Si poisoning,[155-157] but the actual origin of the degradation phenomena could not be identified so far. To ensure comparability of the results as well as to account for any degradation, the same measuring routine was applied in the present study that had been used in previous investigations on LSCF and BaSCF microelectrodes.[10, 14] For the determination of the absolute values of resistances and capacitances given in Table 4.4, measurements were conducted on 10 different microelectrodes of each newly prepared microelectrode sample. Scattering of the values from different microelectrodes of the same sample was typically small compared to the scattering of the values from different microelectrode samples (and ignored in the calculation of the error bars in Table 4.4). Therefore, the absolute values in Table 4.4 are considered not to be influenced significantly by degradation effects. The degradation rate of the surface resistance during the determination of absolute values, increasing with increasing Bi and Fe content, was in most cases lower than the degradation rate of 0.75 Ω cm² h⁻¹ or 47% h⁻¹ relative to the initial value

measured on a $La_{0.6}Sr_{0.4}CoO_{3-\delta}$ thin film on YSZ in a dry oxygen atmosphere at a much lower temperature of 600°C.[161]

4.3.2   Numerical Simulations of Microelectrode Impedance Spectra

The impedance spectrum of a $Bi_{0.5}Sr_{0.5}FeO_{3-\delta}$ microelectrode simulated using the numerical model of Lynch et al.[107] is displayed in Fig. 4.20. Experimentally derived values for the low-frequency resistance and capacitance (Table 4.5) were used as initial guess for the surface resistance and chemical capacitance, respectively. In addition, the electrical conductivities from the present measurements on BiSCF thin films (Fig. 4.10) and bare YSZ substrates (chapter 4.3.1) were inserted as initial parameter values, and the actual tip radius of the probe needle was assumed to correspond to the nominal radius of 2.5 µm. The simulated impedance spectrum qualitatively agrees with the (averaged) experimental spectrum (Fig. 4.20) showing a, compared to LSCF and BaSCF microelectrode impedance spectra, increased high-frequency axis intercept and a small intermediate-frequency semicircle. As mentioned in chapter 4.3.1, these two features are typical indications for a significant impact of sheet resistance on the EIS measurements. The consideration of rate-limiting electrode-electrolyte interfacial processes is not required to qualitatively reproduce the experimentally obtained impedance spectrum.
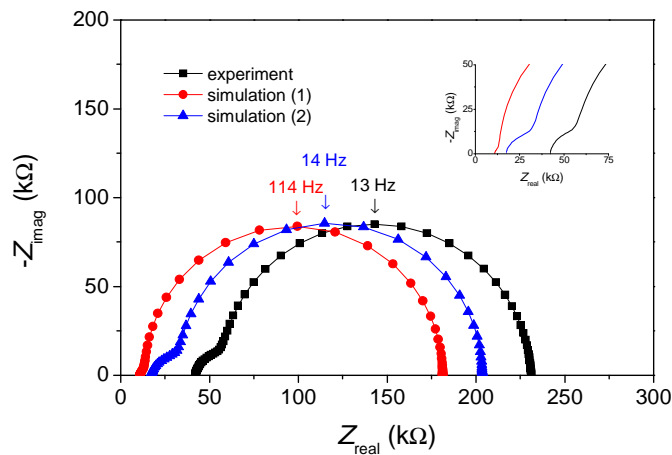

Fig. 4.20. Comparison of the impedance spectra of a 150 nm thin $Bi_{0.5}Sr_{0.5}FeO_{3-\delta}$ microelectrode with 60 µm in diameter on a YSZ single crystal substrate at 750°C and $p(O_2) = 0.2$ bar: the averaged experimental impedance spectrum (simulated with the equivalent circuit in Fig. 4.18 and the experimental values in Table 4.5 using ZView) and the impedance spectra simulated applying the model from ref. [107] with the material parameters derived from experiment (1) and refined via modeling (Table 4.5; (2)). The inset shows a magnification of the high-frequency part of the spectra.

In spite of the good qualitative agreement between experimental and simulated impedance spectrum, further adjustments proved to be necessary to achieve

Table 4.5. Material properties of BiSCF at 750°C and p(O₂) = 0.2 bar obtained from experiment (microelectrode EIS, (thin-film) electrical conductivity measurements, and TG experiments on bulk samples) and FEM simulations with a tip radius of 4.1 μm as described in the text.

| | R_s | | C^δ | | | σ_{el} | |
| | (Ω cm²) | | (kF cm⁻³) | | | (S cm⁻¹) | |
	exp.	sim.	exp.	bulk	sim.	exp.	sim.
$Bi_{0.2}Sr_{0.8}FeO_{3-\delta}$	3.8	3.8	1.0	2.8	12	12	-**
$Bi_{0.5}Sr_{0.5}FeO_{3-\delta}$	4.6*	4.7	0.12*	0.43	1.0	1.3	0.46
$Bi_{0.8}Sr_{0.2}FeO_{3-\delta}$	9.7	11.2	0.015	0.18	0.10	0.71	0.07

*The values were acquired on a smaller number of samples than those in Table 4.4 and are exclusively used in this chapter. Furthermore, R_{HF} = 42 kΩ, R_{IF} = 0.76 Ω cm², and C_{IF} = 54 × 10⁻⁵ F cm⁻² was used.
**The value could not be adjusted due to the absence of an intermediate-frequency semicircle in the experimental impedance spectra.

quantitative agreement. Particularly the low-frequency (apparent chemical) capacitance deduced from the simulated spectrum of 11 F cm⁻³ differs by about one order of magnitude from the low-frequency capacitance of 120 F cm⁻³ from the experimental spectrum used as input estimate for the simulation. In order for C_{LF} (or the peak frequency of the low-frequency semicircle) from experiment and simulation to agree, the input chemical capacitance has to be increased to 1.3 kF cm⁻³. The input chemical capacitance, however, represents the true chemical capacitance of the electrode material (provided that the numerical model is correct). Hence, the true chemical capacitance of $Bi_{0.5}Sr_{0.5}FeO_{3-\delta}$ is by about one order of magnitude higher than the apparent chemical capacitance derived from the experimental microelectrode impedance spectrum.

To adjust the intermediate-frequency semicircle of the simulated impedance spectrum, the input values for the electrical conductivity of the electrode material and the tip radius of the probe needle were varied. As evident from Fig. 4.21a, the intermediate-frequency resistance mainly depends on the electrical conductivity. The intermediate-frequency capacitance, in contrast, is determined by both electrical conductivity and tip radius (Fig. 4.21b). The optimum input values for the two quantities taken from Fig. 4.21 are given in Table 4.5 together with the optimum input values for the surface resistance and chemical capacitance (slightly changed from the above-mentioned values after adjustment of the intermediate-frequency semicircle). From the final microelectrode impedance spectrum simulated using these values (Fig. 4.20), R_{IF} and C_{IF} were estimated to 0.74 Ω cm² and 4.2 × 10⁻⁴ F cm⁻² corresponding to 97% and 78% of the results from experiment. The exact reproduction of the experimental intermediate-frequency semicircle would require simultaneous optimization of all input parameter values which is, however, beyond the scope of this study. Furthermore, the high-frequency axis intercepts of simulated and experimental impedance spectrum do
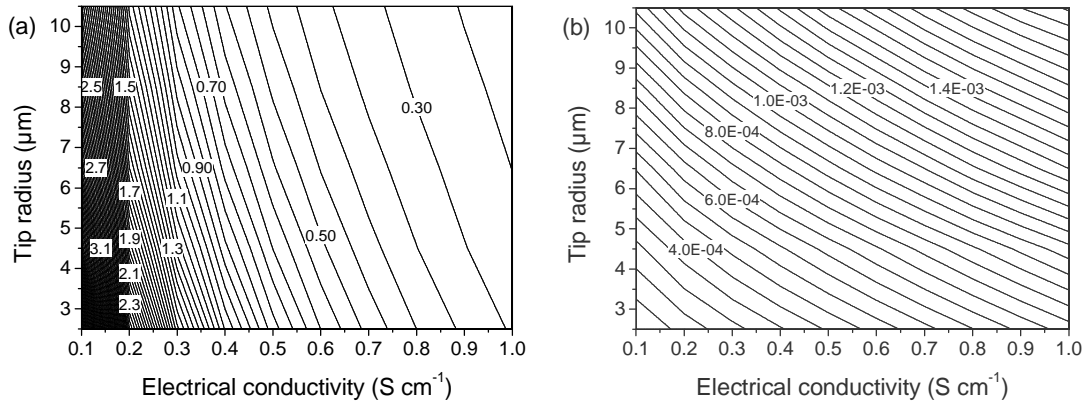
Fig. 4.21. Dependence of (a) intermediate-frequency resistance (in Ω cm^2) and (b) intermediate-frequency capacitance (in F cm^{-2}) on the electrical conductivity and tip radius simulated for a Bi$_{0.5}$Sr$_{0.5}$FeO$_{3-\delta}$ microelectrode with 60 μm in diameter on a YSZ single crystal substrate at 750°C and p(O$_2$) = 0.2 bar.

not completely coincide (Fig. 4.20) possibly due to significant contact resistance between electrode and probe needle not accounted for in the simulation. The simulated electrical potential within a Bi$_{0.5}$Sr$_{0.5}$FeO$_{3-\delta}$ microelectrode is displayed in Fig. 4.22 and shows lateral nonuniformity in particular in the high-frequency regime.

Microelectrode impedance spectra of the other Co-free BiSCF compositions were modeled according to the procedure depicted for Bi$_{0.5}$Sr$_{0.5}$FeO$_{3-\delta}$ that is, by separate adjustment of the different input parameters (but with the tip radius fixed at 4.1 μm) starting from the values in Table 4.4 and Fig. 4.10. The reconciliation of the intermediate-frequency semicircle was, however, omitted for most of the compositions except Bi$_{0.8}$Sr$_{0.2}$FeO$_{3-\delta}$ since the very small semicircle obtained via simulation was not clearly visible in the experimental spectra owing

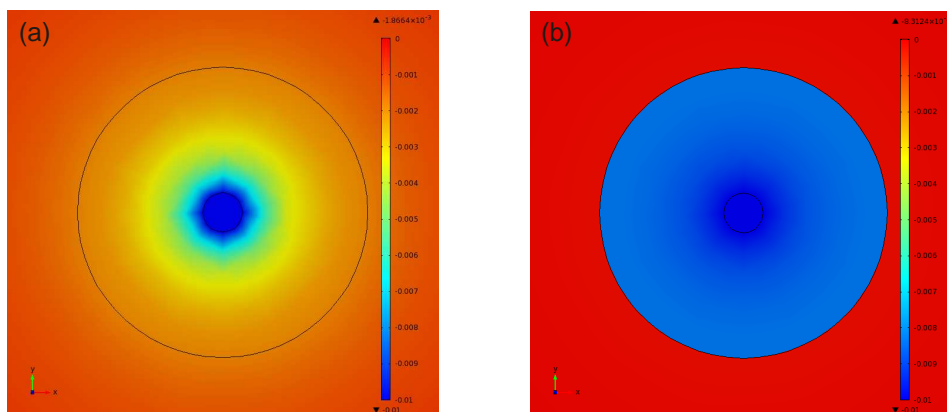*Fig. 4.22. Electrical potential distribution (in V) at (a) 2 × 10^4 Hz and (b) 1 × 10^{-2} Hz simulated for a Bi$_{0.5}$Sr$_{0.5}$FeO$_{3-\delta}$ microelectrode with 60 μm in diameter on a YSZ single crystal substrate with a tip radius of 4.1 μm at 750°C and p(O$_2$) = 0.2 bar.*

to the poor data quality in the respective frequency range. Most strikingly, the apparent chemical capacitances from the experimental impedance spectra are substantially smaller than the true chemical capacitances used to reproduce these spectra (Table 4.5), in accordance with the observations for $Bi_{0.5}Sr_{0.5}FeO_{3-\delta}$. The true chemical capacitances, on the other hand, in most cases even exceed the values extracted for bulk samples from TG measurements. The reason for these discrepancies is not yet clear. The true surface resistance of $Bi_{0.8}Sr_{0.2}FeO_{3-\delta}$ was found to be by 15% higher than the apparent surface resistance or low-frequency resistance from experiment and might, therefore, partially be covered by the intermediate-frequency resistance. A strong deviation of the thin-film electrical conductivity of $Bi_{0.8}Sr_{0.2}FeO_{3-\delta}$ determined in the course of the simulations from the value from electrical conductivity measurements was noticed (which could not be reduced significantly by decreasing the tip radius), but the electrical conductivity of BiSCF thin films on YSZ might be different from that on MgO due to differences in the film microstructure (chapter 4.2.1).

To summarize, all features observed in BiSCF microelectrode impedance spectra could be reproduced qualitatively and, with the exception of the high-frequency axis intercept, nearly quantitatively using the numerical model of Lynch et al..[107] This model does not take into account rate-limiting electrode-electrolyte interfacial processes. The good agreement between experimental and simulated spectra hence implies that these interfacial processes do not need to be considered in the interpretation of the experimental impedance spectra. The increased high-frequency axis intercept and the intermediate-frequency semicircle are most likely caused by high sheet resistance resulting from the exceptionally low electronic conductivity of BiSCF. Further experimental findings supporting this interpretation will be presented in the following chapters. The simulations revealed that the true chemical capacitance of an electrode material can not directly be extracted from experimental microelectrode impedance spectra with the equivalent circuit in Fig. 4.18 in the presence of significant sheet resistance. The apparent chemical capacitance deduced from such spectra is considerably smaller than the true chemical capacitance of the electrode material. The true surface resistance, on the other hand, is only slightly modified by sheet resistance for the materials under investigation.

From the simulations it also becomes evident that the equivalent circuit in Fig. 4.18 is actually not appropriate to evaluate BiSCF microelectrode impedance spectra. This equivalent circuit is based on a one-dimensional physical model.[158] The resistance and capacitance values extracted with it can strictly speaking not be correlated directly to physical properties of the BiSCF electrode. To account for sheet resistance effects, a two-dimensional model has to be applied, which can not simply be represented by an electrical circuit. The evaluation of impedance spectra as described above using the model of Lynch et al.[107] is, however, time-consuming and not suited to be done routinely. Therefore, the equivalent circuit in Fig. 4.18

was used, nevertheless, in this study for the evaluation of microelectrode impedance spectra on a more or less phenomenological basis. This approach seems to be justified, since the quantity of interest, the surface resistance of oxygen exchange, is in most cases still represented reasonably well by the low-frequency resistive element of the equivalent circuit.

4.3.3   EIS Measurements on Macroscopic Thin-Film Samples

In order to cross-check on the results from microelectrode impedance measurements, additional EIS measurements were conducted on "macroscopic samples" of $Bi_{1-x}Sr_xFeO_{3-\delta}$ with x = 0.5 and 0.8 (consisting of two continuous electrode thin films deposited by PLD on both sides of a YSZ substrate; for more details, see chapter 3.4.3). A typical impedance spectrum of a macroscopic sample shows an inductive contribution at high frequencies (possibly due to the lead wires) terminated by a high-frequency axis intercept and one semicircle slightly distorted on the high-frequency side (Fig. 4.23). Moreover, a very small semicircle at intermediate frequencies was observed in impedance spectra of $Bi_{0.5}Sr_{0.5}FeO_{3-\delta}$. Fitting of the impedance spectra with the equivalent circuit in Fig. 4.18 with an inductive element added in series yielded the values given in Table 4.6. The increased high-frequency axis intercepts (a resistive contribution of 11 Ω would be expected owing to the YSZ substrate) and the intermediate-frequency semicircle might be caused by residual sheet resistance. The agreement of the surface resistances from microelectrode and macroscopic measurements is acceptable considering the error bars of the method. This also demonstrates that neither the
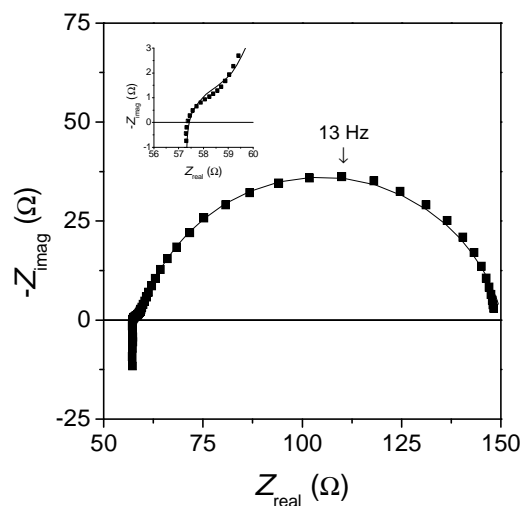

Fig. 4.23. Typical impedance spectrum of a macroscopic sample consisting of two 150 nm thin $Bi_{0.5}Sr_{0.5}FeO_{3-\delta}$ films deposited onto both sides of a YSZ single crystal substrate at 750°C and $p(O_2)$ = 0.2 bar. The solid line represents the best fit obtained with the equivalent circuit in Fig. 4.18. The inset shows a magnification of the high-frequency part of the spectrum.

Table 4.6. Average resistances and capacitances measured on two different macroscopic samples of each composition with a thickness of the BiSCF films of 150 nm at 750°C and p(O₂) = 0.2 bar.

	R_{HF}	R_{IF}	C_{IF}	R_{LF}	C_{LF}
	(Ω)	(Ω cm^2)	(10^{-5} F cm^{-2})	(Ω cm^2)	(F cm^{-3})
$Bi_{0.2}Sr_{0.8}FeO_{3-\delta}$	38 ± 2	-	-	1.8 ± 0.5	$(6.8 \pm 0.5) \times 10^2$
$Bi_{0.5}Sr_{0.5}FeO_{3-\delta}$	69 ± 12	0.41^*	10^*	6.1 ± 0.4	$(4.0 \pm 0.8) \times 10^1$

*The intermediate-frequency semicircle could be fitted reasonably well only for one sample.

Au mesh attached as current collector to the surfaces of macroscopic samples nor the Pt/Ir probe needle exhibit a strong catalytic effect on the oxygen exchange.

4.3.4   Geometry Dependence of the Microelectrode Impedance

EIS measurements have been carried out routinely on microelectrodes of different size following the acquisition of absolute values to reveal possible insufficient sample etching leading to a slight to substantial lowering of the impedance. The dependence of the individual contributions to the microelectrode impedance on the microelectrode diameter is shown in Fig. 4.24 for $Bi_{0.5}Sr_{0.5}FeO_{3-\delta}$ The low-frequency resistance and capacitance are approximately indirectly and directly proportional to the square of the microelectrode diameter or microelectrode area as indicated by a slope close to (-)2 in the log-log plot, in agreement with the diameter dependence anticipated for the surface resistance and chemical capacitance, respectively. R_{HF}, R_{IF}, and C_{IF}, in contrast, exhibit only weak dependence on the electrode diameter. This supports the interpretation that the intermediate-frequency semicircle is not due to an interfacial charge transfer
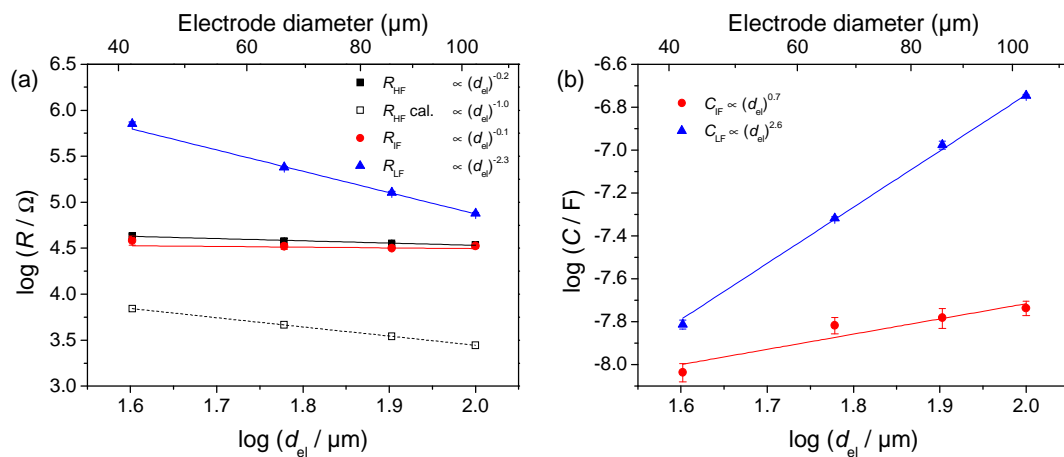

Fig. 4.24. Electrode diameter dependence of the (a) resistances and (b) capacitances measured on 150 nm thin Bi₀.₅Sr₀.₅FeO₃₋ₛ microelectrodes on a YSZ single crystal substrate at 750°C and p(O₂) = 0.2 bar (average values from each two different microelectrodes on the same sample). Open symbols indicate values calculated using the spreading resistance formula.[160]

process, for which $R \propto (d_{el})^{-2}$ and $C \propto (d_{el})^2$ would be expected (and is, indeed, observed for $La_{0.6}Sr_{0.4}FeO_{3-\delta}$ at 500°C).[162] Also, R_{HF} apparently contains contributions other than the electrolyte resistance, for which $R \propto (d_{el})^{-1}$.[160] According to the simulations, $R_{HF} \propto (d_{el})^0$, $R_{IF} \propto (d_{el})^{0.6}$, and $C_{IF} \propto (d_{el})^{0.7}$ results for an intermediate-frequency semicircle and axis intercept caused or influenced by sheet resistance, which is in acceptable to perfect agreement with the experimental findings. The electrode diameter dependences obtained for other BiSCF compositions are comparable to those for $Bi_{0.5}Sr_{0.5}FeO_{3-\delta}$

Increasing the microelectrode thickness is supposed to decrease sheet resistance due to the increased specific electrical conductivity in the electrode film plane. Indeed, impedance spectra measured on $Bi_{0.5}Sr_{0.5}FeO_{3-\delta}$ microelectrodes with 450 nm in thickness under the conditions depicted in Table 4.4 showed a decreased high-frequency axis intercept of (16 ± 2) kΩ (average value from two microelectrode samples) and no intermediate-frequency semicircle. The surface resistance of (2.2 ± 0.7) Ω cm² was found to be slightly lower which might at least partly result from the somewhat higher surface roughness of the thicker films noticed via SEM. The low-frequency capacitance increases only moderately to $(1.8 \pm 0.1) \times 10^2$ F cm⁻³ when increasing the electrode thickness to 450 nm, although C_{LF} is assumed to strongly increase with decreasing sheet resistance. However, sheet resistance might still influence the microelectrode impedance even if not indicated by a specific spectral feature.

4.3.5   Temperature Dependence of the Microelectrode Impedance

The temperature dependence of the resistances and capacitances obtained from a microelectrode sample of $Bi_{0.5}Sr_{0.5}FeO_{3-\delta}$ is displayed in Fig. 4.25. An approximately linear relationship was found for each of the quantities to be measured between the logarithm of the quantity and the inverse temperature, which can be expressed analogously to the Arrhenius equation, that is, $R \propto$ exp(-E_a'/RT) and $C \propto$ exp(-E_a'/RT). For the resistive quantities, the parameter E_a' can be correlated to the activation energy E_a of the rate constant of the corresponding process (which is proportional to the inverse resistance or conductance) according to $E_a = -E_a'$. For the capacitive quantities, E_a has to be regarded as a formal activation energy rather. The temperature dependences observed for other BiSCF compositions and macroscopic samples qualitatively agree with those from $Bi_{0.5}Sr_{0.5}FeO_{3-\delta}$ microelectrodes. The (formal) activation energies of the inverse resistances and capacitances extracted for $Bi_{0.5}Sr_{0.5}FeO_{3-\delta}$ and other BiSCF perovskites are listed in Table 4.7.

The activation energy of the inverse low-frequency or surface resistance shows no clear dependence on the electrode composition. A significant discrepancy was found between the activation energies of $(R_{LF})^{-1}$ from microelectrode and macroscopic samples, respectively, as illustrated in Fig. 4.26. $E_a((R_{LF})^{-1})$ measured

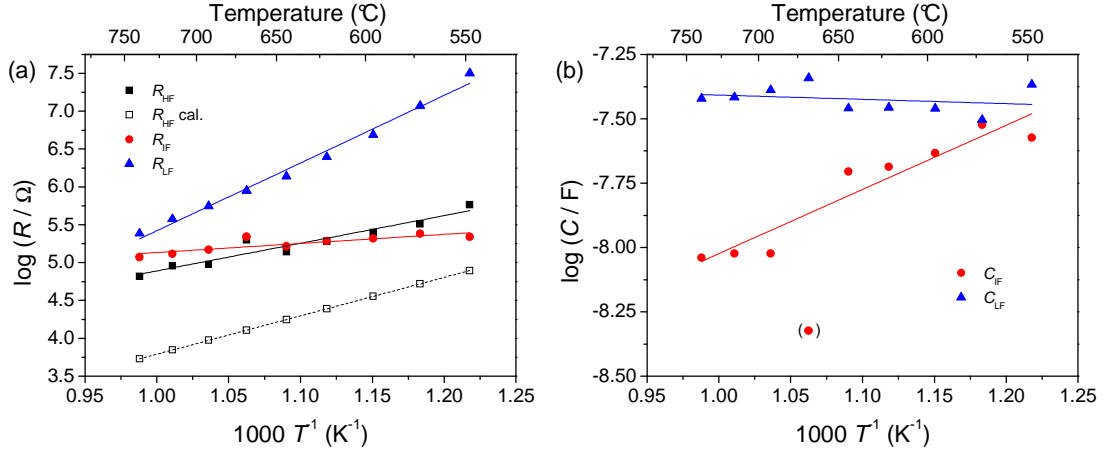*Fig. 4.25. Temperature dependence of the (a) resistances and (b) capacitances measured on a 150 nm thin Bi$_{0.5}$Sr$_{0.5}$FeO$_{3-\delta}$ microelectrode with 60 μm in diameter on a YSZ single crystal substrate at p(O$_2$) = 0.2 bar. Open symbols indicate values calculated using the spreading resistance formula.[160]*

on a macroscopic sample of Bi$_{0.5}$Sr$_{0.5}$FeO$_{3-\delta}$ agrees well with the activation energy of the inverse area-specific resistance determined for porous Bi$_{0.5}$Sr$_{0.5}$FeO$_{3-\delta}$ electrodes of 1.2 eV between 450°C and 750°C.[100] $E_a((R_{LF})^{-1})$ from BiSCF microelectrode samples, on the other hand, appears to increase with decreasing temperature. Therefore, $E_a((R_{LF})^{-1})$ from Bi$_{0.5}$Sr$_{0.5}$FeO$_{3-\delta}$ microelectrodes averaged over the investigated temperature range is considerably higher than the activation energy of the inverse area-specific resistance derived from porous electrodes. A similar inconsistency has been mentioned for Ba$_{0.5}$Sr$_{0.5}$Co$_{0.8}$Fe$_{0.2}$O$_{3-\delta}$[14] Apparently, it is not primarily a consequence of morphological differences or differences in the electrode surface composition resulting from different processing temperatures, since the activation energies of the inverse surface or area-specific resistance from macroscopic samples and porous electrodes exhibit comparable values.

Table 4.7. Average (formal) activation energies of the inverse resistances and capacitances measured on two 150 nm thin microelectrodes with 60 μm in diameter from two different microelectrode samples of each BiSCF composition (and one macroscopic sample, values given in brackets) between 550°C and 750°C at p(O$_2$) = 0.2 bar. Scattering ranges refer to statistical errors, the error in $E_a((R_{LF})^{-1})$ due to sample degradation was estimated to -0.1 eV.

	$E_a((R_{HF})^{-1})$ (eV)	$E_a((R_{IF})^{-1})$ (eV)	$E_a((C_{IF})^{-1})$ (eV)	$E_a((R_{LF})^{-1})$ (eV)	$E_a((C_{LF})^{-1})$ (eV)
Bi$_{0.2}$Sr$_{0.8}$FeO$_{3-\delta}$	0.63 ± 0.05 (0.73)	-	-	2.4 ± 0 (1.2)	0.17 ± 0.01 (0.46)
Bi$_{0.5}$Sr$_{0.5}$FeO$_{3-\delta}$	0.65 ± 0.11 (0.80)	0.28 ± 0.02 (0.24)	0.66 ± 0.17 (0.04)	2.1 ± 0.3 (1.1)	0.16 ± 0.19 (0.60)
Bi$_{0.8}$Sr$_{0.2}$FeO$_{3-\delta}$	0.78 ± 0.06	0.31 ± 0.23	0.46 ± 0.04	2.3 ± 0	-0.12 ± 0.04
Bi$_{0.5}$Sr$_{0.5}$Co$_{0.2}$Fe$_{0.8}$O$_{3-\delta}$	0.68 ± 0.01	-	-	2.1 ± 0.1	0.17 ± 0.01
Bi$_{0.5}$Sr$_{0.5}$Co$_{0.4}$Fe$_{0.6}$O$_{3-\delta}$	0.78 ± 0.06	-	-	2.4 ± 0.1	0.17 ± 0.01

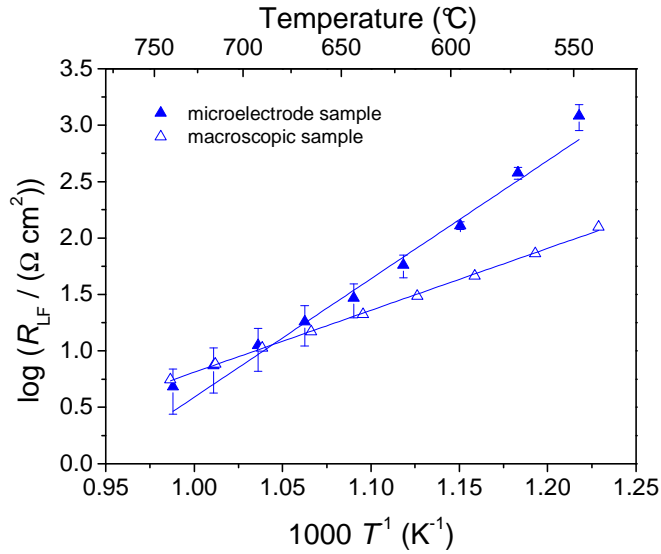*Fig. 4.26. Comparison of the temperature dependence of the low-frequency resistance of $Bi_{0.5}Sr_{0.5}FeO_{3-\delta}$ measured on 150 nm thin microelectrodes with 60 μm in diameter (average values from two microelectrodes on two different samples) and a macroscopic sample with a thickness of the electrode films of 150 nm at $p(O_2) = 0.2$ bar.*

The impedance of microelectrodes might be influenced by a thermovoltage in particular at high temperatures.[163] Such a thermovoltage arises from a temperature gradient caused by the asymmetric sample heating and local cooling of microelectrodes via the probe needle. A thermovoltage of 54 mV was measured at 650°C under open circuit conditions on a $Bi_{0.5}Sr_{0.5}FeO_{3-\delta}$ microelectrode of 60 μm in diameter, which corresponds to an anodic bias increasing the low-frequency resistance by about 40% (chapter 4.3.7). This resistance increase at high temperature can not explain the observed modification of the activation energy of microelectrode $(R_{LF})^{-1}$. Measurements of $E_a((R_{LF})^{-1})$ on $Bi_{0.5}Sr_{0.5}FeO_{3-\delta}$ microelectrodes with a larger diameter of 100 μm yielded a value of 2.0 eV (average value from two microelectrode samples), which is comparable to that obtained on microelectrodes with 60 μm in diameter (Table 4.7), although local cooling is expected to be less relevant on the larger electrodes. Furthermore, the good agreement of the low-frequency resistances from microelectrode and macroscopic samples at high temperatures to some extent contradicts the assumption of a considerable impact of a thermovoltage on the microelectrode impedance. From the presented results, it is not possible to conclude on the origin of the different activation energies of $(R_{LF})^{-1}$ from microelectrode and macroscopic samples, respectively.

The activation energy of $(R_{HF})^{-1}$ is typically lower than the activation energy of the YSZ ionic conductivity of (1.0 ± 0) eV between 400°C and 700°C from electrical conductivity measurements on two bare YSZ substrates. This most likely results from the contributions of sheet resistance and contact resistance to the high-frequency axis intercept. The E_a values determined for the inverse intermediate-

frequency resistance and capacitance, respectively, are mostly in fair to good agreement with the activation energies of the electronic conductivity (0.11 eV and 0.45 eV for thin-film $Bi_{0.5}Sr_{0.5}FeO_{3-\delta}$ and $Bi_{0.8}Sr_{0.2}FeO_{3-\delta}$ between 550°C and 750°C at $p(O_2)$ = 0.2 bar, chapter 4.1.5), but significantly different from E_a found for the inverse interfacial contributions in LSCF (e.g., $E_a((R_{IF})^{-1})$ = 1.4 eV and $E_a((C_{IF})^{-1})$ = 0 eV for $La_{0.6}Sr_{0.4}FeO_{3-\delta}$ in air)[10] and BaSCF (e.g., $E_a((R_{IF})^{-1})$ = 1.2 eV and $E_a((C_{IF})^{-1})$ = -0.02 eV for $Ba_{0.25}Sr_{0.75}Co_{0.8}Fe_{0.2}O_{3-\delta}$ at $p(O_2)$ = 0.2 bar).[48] The low-frequency capacitance shows only little dependence on the temperature in accordance with the small changes of the chemical capacitance upon changing temperature observed by thermogravimetry on bulk samples (chapter 4.1.3). For example, the chemical capacitance of bulk $Bi_{0.2}Sr_{0.8}FeO_{3-\delta}$ calculated using equation (4.4) increases from 2.8 kF cm^{-3} at 750°C to 4.8 kF cm^{-3} at 550°C and a $p(O_2)$ of 0.2 bar corresponding to a formal activation energy of the inverse quantity of 0.19 eV.

Temperature-dependent measurements on both microelectrode and macroscopic samples were routinely conducted directly after determination of the absolute values (and diameter dependence) starting from 750°C in the direction of decreasing temperature. To estimate the influence of degradation on the (formal) activation energies, further measurements were subsequently carried out in the direction of increasing temperature. The activation energy of the inverse low-frequency resistance from the second measurement series was typically 0.1 eV lower than that from the first measurement series indicating negligible degradation of the sample over the whole measuring time.

4.3.6 Oxygen Partial Pressure Dependence of the Microelectrode Impedance

Fig. 4.27 shows the $p(O_2)$ dependence of resistances and capacitances from a microelectrode sample of $Bi_{0.5}Sr_{0.5}FeO_{3-\delta}$. For each of the measured quantities, a linear relationship was observed between the logarithm of the quantity and the logarithm of the $p(O_2)$. Therefore, $R \propto (p(O_2))^{-n}$ and $C \propto (p(O_2))^{-n}$ applies, and the exponent n can be extracted from the slope of the log-log plot. A qualitatively identical behavior was found for the other BiSCF compositions and macroscopic samples. Table 4.8 depicts the exponents deduced for the different BiSCF perovskites.

The $p(O_2)$ dependence of the low-frequency/surface resistance can give information on the rate-determining step of the surface oxygen exchange reaction, since k^q is proportional to the equilibrium exchange rate $\Re_0$ (equation (2.9)). Reformulating equation (2.10), $\Re_0$ might be related to the equilibrium reaction rate $\vec{\Re}_0$ of the forward reaction (or $\overleftarrow{\Re}_0$ of the backward reaction) yielding

$$\Re_0 = \sqrt{\vec{\Re}\,\overleftarrow{\Re}} = \bar{\Re}_0 \propto (p(O_2))^a [\widehat{e^-}]^b [\widehat{V_O^{\bullet\bullet}}]^c \qquad (4.6)$$
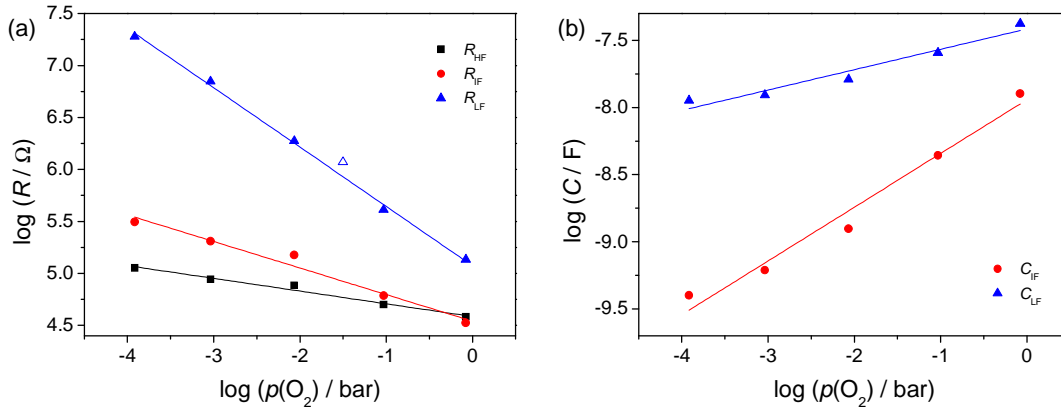
Fig. 4.27. Oxygen partial pressure dependence of the (a) resistances and (b) capacitances measured on a 150 nm thin $Bi_{0.5}Sr_{0.5}FeO_{3-\delta}$ microelectrode with 60 µm in diameter on a YSZ single crystal substrate at 750°C. The open symbol indicates the low-frequency resistance recorded at the end of the measurement series.

where, for the sake of simplicity, electrons are presumed to be the relevant electronic defects. The reaction order a of gaseous oxygen molecules is 1 if molecular oxygen species are involved in the rds and 0.5 if only atomic oxygen species participate in the rds.[42] The exponent n describing the overall $p(O_2)$ dependence of $\tilde{\Re}_0$ is, however, smaller than 1 and 0.5, respectively, as the concentrations of the point defects in equation (4.6) exhibit a negative $p(O_2)$ dependence. The exponents n for the surface resistance in Table 4.8 are, except for $Bi_{0.8}Sr_{0.2}FeO_{3-\delta}$ always larger than 0.5. This implies that molecular oxygen species are involved in the rds. To explain the large deviation of the n values from 1, an effective reaction order b of electrons of 2 rather than 1 has to be assumed. The $p(O_2)$ dependence of the oxygen vacancy concentration (and mobility) is typically too small to draw reliable conclusions on the role of oxygen vacancies in the rate-determining (diffusion) step from $p(O_2)$-dependent impedance measurements.

Table 4.8. Average exponents n in R,C $\propto (p(O_2))^{-n}$ measured on two 150 nm thin microelectrodes with 60 µm in diameter from two different microelectrode samples of each BiSCF composition (and one macroscopic sample, values given in brackets) at 750°C. Scattering ranges refer to statistical errors, the error in n(R_{LF}) due to sample degradation was estimated to +0.02.

	$n(R_{HF})$	$n(R_{IF})$	$n(C_{IF})$	$n(R_{LF})$	$n(C_{LF})$
$Bi_{0.2}Sr_{0.8}FeO_{3-\delta}$	0.15 ± 0.04	0.29 ± 0.04	-0.33 ± 0.01	0.59 ± 0.03	-0.10 ± 0.04
	(0.03)			(0.71)	(-0.07)
$Bi_{0.5}Sr_{0.5}FeO_{3-\delta}$	0.10 ± 0.03	0.20 ± 0.06	-0.37 ± 0.04	0.58 ± 0.01	-0.15
	(0)	(0.11)	(-0.04)	(0.52)	(-0.20)
$Bi_{0.8}Sr_{0.2}FeO_{3-\delta}$	0.04 ± 0.04	0.13 ± 0.06	-0.14 ± 0.04	0.52 ± 0.05	-0.09 ± 0.02
$Bi_{0.5}Sr_{0.5}Co_{0.2}Fe_{0.8}O_{3-\delta}$	0.17 ± 0.02	0.19 ± 0.01	-0.34 ± 0.04	0.63	-0.01 ± 0.02
$Bi_{0.5}Sr_{0.5}Co_{0.4}Fe_{0.6}O_{3-\delta}$	0.17 ± 0.02	0.15 ± 0.01	-0.33 ± 0.08	0.61 ± 0.06	-0.08 ± 0.05

A systematic difference between the exponents n for R_{LF} from microelectrode and macroscopic samples or a systematic dependence of $n(R_{LF})$ on the electrode composition could not be revealed. The $p(O_2)$ dependence of R_{HF} is small compared to that of R_{LF} in accordance with the low $p(O_2)$ dependence expected for a resistive contribution dominated by the ion transport resistance of YSZ. The $p(O_2)$ dependence of R_{IF} and C_{IF}, respectively, is higher than that reported for the interfacial resistances and capacitances of LSCF (e.g., $n(R_{IF})$ = -0.08 and $n(C_{IF})$ = -0.08 for $La_{0.6}Sr_{0.4}Co_{0.8}Fe_{0.2}O_{3-\delta}$ at 680°C)[72] and BaSCF (e.g., $n(R_{IF})$ = 0.02 and $n(C_{IF})$ = 0.03 for $Ba_{0.25}Sr_{0.75}Co_{0.8}Fe_{0.2}O_{3-\delta}$ at 700°C).[48] The exponent n for the intermediate-frequency resistance agrees well with the exponent n in $\sigma_{el} \propto (p(O_2))^n$ (chapter 4.1.5). Finally, the $p(O_2)$ dependence of C_{LF} is negligible and thus consistent with the low $p(O_2)$ dependence of the chemical capacitance observed by thermogravimetry on the bulk materials (chapter 4.1.3). For instance, the chemical capacitance of bulk $Bi_{0.2}Sr_{0.8}FeO_{3-\delta}$ calculated via equation (4.4) increases from 1.7 kF cm^{-3} at a $p(O_2)$ of 10^{-3} bar to 2.7 kF cm^{-3} at a $p(O_2)$ of 0.8 bar and 750°C resulting in a n value of -0.07.

To account for any sample degradation, $p(O_2)$-dependent measurements were conducted again following a procedure similar to that described in ref. [14] after determination of the temperature dependence. EIS measurements were first carried out in the direction of increasing $p(O_2)$. Then, a final measurement was performed again at a lower $p(O_2)$ of about 0.01 bar (e.g., Fig. 4.27, open symbol). From the last three measurements (at $p(O_2)$ = 0.1 bar, 0.85 bar, and 0.01 bar), an exponent n for the low-frequency resistance was obtained by 0.03 on average higher than n deduced from all measurements except the last one (at $p(O_2)$ = 0.01 bar). The real n value is expected to lie between the n value from the first measurements (underestimated due to degradation) and that from the last measurements (overestimated due to degradation). Therefore, $n(R_{LF})$ is assumed to be underestimated by roughly 0.03/2 due to degradation, which is considered negligible and does not change the interpretation presented above. However, degradation at the lowest $p(O_2)$ of about 10^{-4} bar seemed to proceed comparatively fast, for example, with a degradation rate of the low-frequency resistance of approximately 360% h^{-1} relative to the initial value calculated from 4 subsequent measurements on a $Bi_{0.5}Sr_{0.5}FeO_{3-\delta}$ microelectrode sample. Thus, depending on the time required to record a reasonable impedance spectrum at the lowest $p(O_2)$, the samples might already be degraded to some extent during measurement of the $p(O_2)$ dependence.

4.3.7 DC-Bias Dependence of the Microelectrode Impedance

The effect of a small DC bias on the different resistive and capacitive contributions to the microelectrode impedance was studied on a $Bi_{0.5}Sr_{0.5}FeO_{3-\delta}$ sample (Fig. 4.28). In accordance with the observations made for LSCF[34] and BaSCF,[48] the low-frequency or surface resistance roughly decreases with increasing

magnitude of both anodic and cathodic bias. However, the maximum of the surface resistance is shifted to an anodic bias value of 60 mV. A thermovoltage of 54 mV was measured on a microelectrode on which DC-bias-dependent measurements were conducted (chapter 4.3.5) corresponding to an additional superimposed anodic bias. Hence, the shift of the maximum surface resistance can not be explained by a compensation of the applied DC bias by a thermovoltage with opposite polarity. On the other hand, the onset of the surface resistance decrease under anodic DC bias coincides with the disappearance of the intermediate-frequency semicircle. A quantitative description of the DC bias dependence of the surface resistance is not trivial, since the overall oxygen exchange rate is determined by the electrostatic surface potential step.[164] This potential step arises from the coverage of the electrode surface with negatively charged adsorbed oxygen species. Any change of the DC bias modifies not only the concentration of adsorbed oxygen species, but also the rate of individual reaction steps they are involved in. Therefore, changes in the surface potential step do not necessarily depend linearly on the applied DC bias.
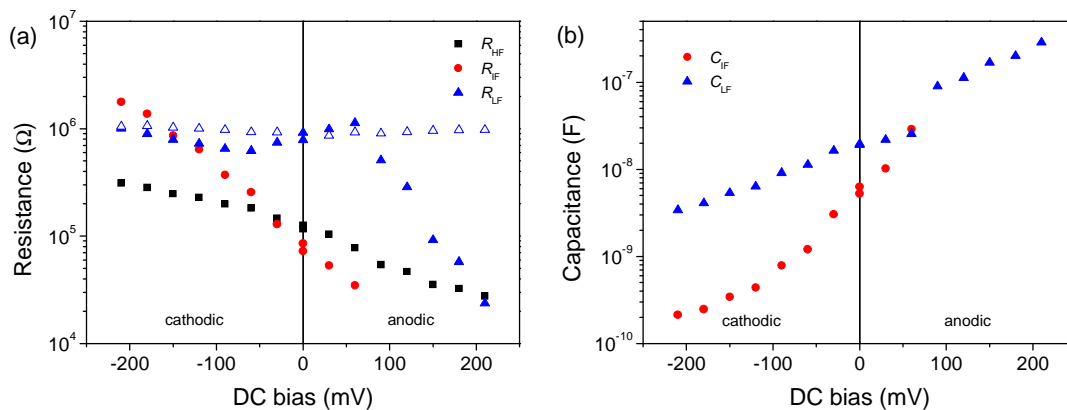

Fig. 4.28. DC-bias dependence of the (a) resistances and (b) capacitances measured on a 150 nm thin Bi$_{0.5}$Sr$_{0.5}$FeO$_{3-\delta}$ microelectrode with 60 μm in diameter on a YSZ single crystal substrate at 650°C and p(O$_2$) = 0.2 bar. Open symbols indicate the low-frequency resistances recorded 2 min after switching off the bias.

In the region of high absolute values of cathodic bias (where a net incorporation of oxygen into the microelectrode occurs), the surface resistance starts to increase with increasing bias value most probably due to the increasing impact of sheet resistance. The increase in sheet resistance also causes the monotonic increase of R_{HF} and R_{IF} from the maximum anodic to the maximum cathodic bias value. A large cathodic bias corresponds to a low $p(O_2)$ and hence a low concentration of electron holes in the electrode resulting in high sheet resistance and high values of R_{HF}, R_{IF}, and probably R_{LF}. In contrast, an axis intercept dominated by the ohmic resistance of the electrolyte was expected to remain unaffected by a DC bias, whereas for an

interfacial resistance, a trend opposite to that observed for R_{IF} or no change upon changing DC bias was reported for LSCF[34] and BaSCF,[48] respectively. Both C_{IF} and C_{LF} were found to increase with increasing DC bias. The bias dependence of C_{LF} is in accordance with the chemical capacitance from thermogravimetry on bulk samples being higher at high $p(O_2)$ (e.g., $C^\delta = 4.3 \times 10^2$ F cm^{-3} at a $p(O_2)$ of 0.2 bar versus $C^\delta = 1.3 \times 10^2$ F cm^{-3} at a $p(O_2)$ of 10^{-3} bar and 750°C as calculated using equation (4.4)). The DC bias dependence of resistances and capacitances obtained from a second $Bi_{0.5}Sr_{0.5}FeO_{3-\delta}$ microelectrode sample qualitatively agrees with that described above.

DC-bias-dependent measurements were carried out on newly prepared microelectrode samples after determination of the absolute values at 750°C. Impedance spectra were typically recorded after the sample being exposed to the respective DC bias for two minutes. The bias dependence was determined first on one microelectrode in the direction of increasing anodic bias, then on another microelectrode in the direction of increasing magnitude of cathodic bias. Each time after switching off the bias, the electrode was allowed to "regenerate" for two minutes and another impedance spectrum was recorded in the absence of a bias to reveal possible irreversible changes of the surface resistance. Severe degradation or an irreversible decrease of the surface resistance reported, for example, for LSCF[31] and BaSCF[56] microelectrodes exposed to a high cathodic bias was, however, not observed. The surface resistances measured after each measurement under anodic or cathodic bias are included in Fig. 4.28 and show only little difference.

4.3.8 EIS Measurements on Modified Thin-Film Microelectrodes

As mentioned in chapter 4.2.2, $Bi_{0.5}Sr_{0.5}FeO_{3-\delta}$ films with smooth surface were obtained at a deposition $p(O_2)$ lower than the standard $p(O_2)$. EIS measurements on microelectrodes made from these films can give information on the influence of steps and kinks on the oxygen exchange kinetics. Average surface resistance values of 4.4 Ω cm^2 (film deposition temperature 650°C) and 4.5 Ω cm^2 (film deposition temperature 700°C) were acquired under the conditions listed in Table 4.4 on two "smooth" microelectrode samples in good agreement with the surface resistance from rough $Bi_{0.5}Sr_{0.5}FeO_{3-\delta}$ films deposited under standard conditions (Table 4.4). Considering the differences in surface area, one might assume steps and kinks to exhibit a slight decelerating effect as suggested previously.[150] On the other hand, the experimental results, that is, the less pronounced intermediate-frequency semicircle and the low axis intercept of 16 kΩ from both samples, indicate a higher electrical conductivity of the smooth films possibly accelerating oxygen exchange. A higher electrical conductivity might result from the epitaxial nature of these films (chapter 4.2.1) or from changes of the cation stoichiometry due to the modified deposition conditions. To reliably estimate the influence of the surface morphology on the oxygen exchange kinetics, further experiments are required.

The results of temperature and $p(O_2)$-dependent measurements on smooth microelectrode samples are largely consistent with those from rough $Bi_{0.5}Sr_{0.5}FeO_{3-\delta}$ samples.

The average surface resistance from a microelectrode sample of $Bi_{0.5}Sr_{0.5}FeO_{3-\delta}$ deliberately produced to contain 20 mol% of Co_3O_4 as second phase was determined to 1.3 Ω cm^2 under the conditions depicted in Table 4.4, which is lower than the average surface resistance from a number of microelectrode samples of pure $Bi_{0.5}Sr_{0.5}FeO_{3-\delta}$ (Table 4.4). One might, therefore, state that the addition of Co_3O_4 leads to an acceleration of the oxygen exchange and that the low surface resistance obtained for Co-containing BiSCF perovskites possibly results from the presence of small amounts of Co_3O_4 not detectable by XRD. The addition of a certain amount of the oxidation catalyst Co_3O_4 was reported previously to decrease the polarization resistance of perovskite-type SOFC cathodes.[144-146] However, all previous studies have been conducted on porous electrodes. From the published data, it is often not possible to estimate whether the resistance decrease might be related to morphological changes. Furthermore, to definitely approve an accelerating effect of Co_3O_4 on the oxygen exchange kinetics in the present case, the phase composition of the electrode surface needs to be elucidated, which is not a trivial task though.

The preparation of microelectrodes via photolithography and inert gas ion beam etching proved to be a rather time-consuming and not always straightforward method. Therefore, an attempt was made to produce microelectrodes in a simpler way requiring less processing steps. The YSZ substrates were covered by a shadow mask during PLD to directly obtain the desired cylindrical shapes. This shadow mask consisted of an approximately 250 µm thin piece of sapphire into which small holes were cut by a laser. However, for the microelectrodes to reach a thickness sufficient to make them visible under the optical microscope attached to our measuring setup, these holes had to be relatively large leading to a minimum microelectrode diameter of about 180 µm. Impedance spectra recorded on such microelectrodes of $Bi_{0.2}Sr_{0.8}FeO_{3-\delta}$ and $Bi_{0.5}Sr_{0.5}FeO_{3-\delta}$ typically showed a huge intermediate-frequency semicircle with an associated resistance higher than the low-frequency resistance, which, in turn, exhibited exceptionally high and strongly scattering values. Furthermore, the microelectrodes fabricated by this one-step method displayed a rather ill-defined shape with a high surface roughness as evident from SEM and profilometric measurements. Due to these drawbacks, the approach was not pursued further.

4.4   Thin-Film Electrochemical Polarization Measurements

In the present study, it was attempted to determine the ionic conductivity of both BiSCF thin films and bulk samples via electrochemical polarization measurements. Previously, electrical conductivity relaxation and isotope exchange experiments had been carried out to measure the ionic conductivity of BaSCF.[14, 56, 147] However, the methods had been found to exhibit several shortcomings, in particular the necessity to produce a large number of samples (one sample for each combination of temperature and $p(O_2)$) with a density of approximately 100%, on which a large number of secondary-ion mass spectrometry (SIMS) scans need to be performed. The densities obtained for BiSCF pellets by SPS and conventional sintering are typically below the required value (chapter 3.1). Unfortunately, electrochemical polarization measurements on bulk samples turned out to be not straightforward to realize. The investigated $Bi_{0.5}Sr_{0.5}FeO_{3-\delta}$ pellet covered by an electron-blocking YSZ layer deposited by PLD strongly reacted with the commercially available sealing glass powders under the conditions applied to achieve sealing of the sample edges; the electrical conductivity measured without sealing was strongly $p(O_2)$-dependent indicating significant oxygen exchange to occur at the sample edges. Therefore, the main emphasis here lies on ionic conductivity measurements on electrochemical polarization cells in thin-film configuration. In addition, ionic conductivity data from electrical conductivity measurements on bulk samples of selected compositions at low $p(O_2)$ will be shown.

4.4.1   Electrochemical Polarization Cell Setup

To perform electrochemical polarization measurements on BiSCF thin films, asymmetric electrochemical polarization cells were set up according to

$$O_2,Pt|ScSZ|BiSCF|Pt,O_2 \qquad\qquad (4.7)$$

Here, the flux of electrons is blocked by the ion-conducting ScSZ electrode (t_{eon} = 10^{-9} for 16 mol% Sc_2O_3-doped ZrO_2 at 700°C and a $p(O_2)$ of 1 bar),[165] whereas the Pt electrode on the other side of the cell allows for the reversible exchange of both electrons and oxide ions. Fig. 4.29 shows a photograph of a thin-film electrochemical polarization cell together with a schematic representation of a longitudinal section of the cell.

A MgO single crystal was used as substrate for the overall cell due to its negligible electronic and ionic conductivity (the electrical conductivity of a bare MgO substrate amounts to 1.4×10^{-9} S cm^{-1} at 650°C[106] leading to a resistive contribution of about 20 GΩ in the present case at least two orders of magnitude

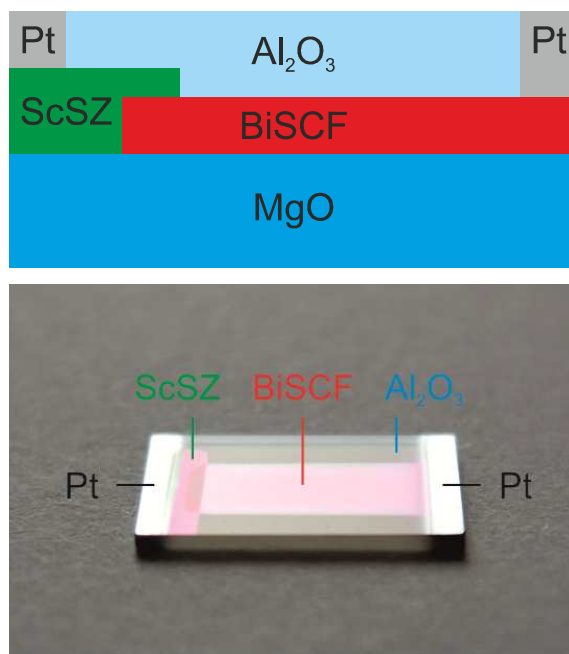*Fig. 4.29. Photograph of a Bi$_{0.5}$Sr$_{0.5}$FeO$_{3-\delta}$ thin-film electrochemical polarization cell with schematic depiction of the cell setup. The colors in the photograph correspond to the interference colors of the nominally 200-1000 nm thin films.*

higher than the resistances expected for the other cell components). Onto the MgO substrate, a 80-170 nm thin stripe of BiSCF was deposited by PLD with the help of a sapphire shadow mask, and the electron-blocking electrode was grown on one end of the BiSCF stripe again by PLD using another shadow mask. ScSZ was chosen as electrode material since it exhibits a higher ionic conductivity (σ_{ion} = 6.7×10^{-3} S cm^{-1} at 650°C for a ScSZ thin film deposited by PLD onto a MgO substrate) than YSZ (σ_{ion} = 2.5×10^{-3} S cm^{-1} at 650°C from a YSZ thin film on MgO produced by PLD) resulting in a smaller contribution of the electrode resistance to the overall cell resistance. The ScSZ electrode was deposited to a nominal thickness as high as 1000 nm to further minimize its resistance.

As pointed out in chapter 2.2, sealing of the BiSCF film against the surrounding gas atmosphere is crucial to avoid any electronic leakage current originating from oxygen exchange on the film surface. Several oxide materials with low electronic and ionic conductivity were taken into consideration as sealants and deposited by electron beam evaporation each to a nominal thickness of 300 nm onto the BiSCF layers:

(i)   SiO$_2$ proved not to be suitable as sealant material due to its high reactivity towards BiSCF. A mixture of equal volume fractions of powder Bi$_{0.5}$Sr$_{0.5}$FeO$_{3-\delta}$ and SiO$_2$ nanopowder heated to 700°C for 24 h did not undergo a formation of new compounds or a change in the perovskite lattice constant according to XRD. However, X-ray diffractograms of a Bi$_{0.5}$Sr$_{0.5}$FeO$_{3-\delta}$ thin-film cell sealed with SiO$_2$ and a bare Bi$_{0.5}$Sr$_{0.5}$FeO$_{3-\delta}$

film on MgO covered with a SiO_2 layer, both heated to 700°C, showed a strongly decreased intensity of the perovskite peaks or even their complete absence indicating severe decomposition of the BiSCF.

(ii)   Polarization measurements on a $Bi_{0.5}Sr_{0.5}Co_{0.2}Fe_{0.8}O_{3-\delta}$ cell covered with a MgO layer yielded a comparatively high and strongly $p(O_2)$-dependent apparent ionic conductivity of the perovskite phase suggesting that sufficient sealing could not be achieved. The same effect was observed for a $SrFeO_{3-\delta}$ cell with an additional SiO_2 layer evaporated on top of the MgO layer. XRD on both cells after the measurements did not provide evidence for a decomposition of the cell constituents. From SEM investigations, the MgO and SiO_2 surface, respectively, appeared to be free of cracks.

(iii)   The best results were achieved with an Al_2O_3 sealing layer. According to XRD measurements including lattice constant analyses of powder mixtures of the investigated BiSCF compositions with nanosized Al_2O_3 heated to 700°C for 24 h, the compounds are chemically stable towards each other. Furthermore, XRD on the samples covered with Al_2O_3 after the polarization measurements did not give any notice of decomposition. The obtained ionic conductivity of BiSCF in most cases did not exhibit a significant $p(O_2)$ dependence.

To complete the cell setup for polarization measurements, 200 nm thin Pt electrodes were sputtered onto both ends of the sample providing the reversible electrode and the electrical connection to the ScSZ electrode, respectively. The whole cell was arranged in a way that the Pt electrode on the electron-blocking side was not allowed to vertically overlap with the BiSCF film. This arrangement was chosen in order to prevent a significant electronic leakage current from the Pt electrode through the ScSZ thickness into the BiSCF. Using literature data for the ionic conductivity of $Bi_{0.5}Sr_{0.5}FeO_{3-\delta}$[100] and the electronic conductivity of 16 mol% Sc_2O_3-doped ZrO_2 extrapolated from 900°C,[165] the ratio $R_{ion}^{BiSCF} / R_{eon}^{ScSZ}$ for a lateral gap between the Pt electrode and the BiSCF film of 1 mm was estimated to about $10^{-7} \ll 1$ at 700°C and a $p(O_2)$ of 1 bar. Therefore, the condition for sufficient blocking of electronic charge carriers is fulfilled.

4.4.2   DC Measurements on Thin-Film Electrochemical Polarization Cells

Fig. 4.30 displays the typical current response of a BiSCF thin-film polarization cell to a stepwise change of the applied DC voltage U from 0 mV to 100 mV and back to 0 mV. When the voltage is switched to 100 mV, a stepwise increase of the current occurs followed by a current decrease, which is caused by the stoichiometry polarization in the sample and might be fitted at long times ($t \gtrsim 15$ min for the current curve in Fig. 4.30) with an exponential decay function in accordance with equation (2.13). From the steady-state polarization current, the DC resistance of

the cell can be calculated yielding, after subtraction of additional resistive contributions, for example, due to electrode overpotentials or interfacial processes (chapter 4.4.3), the ionic conductivity of the BiSCF film. When the applied voltage is switched off again, a stepwise increase of the current in the opposite direction results followed by a current decrease which, as well, obeys an exponential decay law at long times in agreement with equation (2.14).
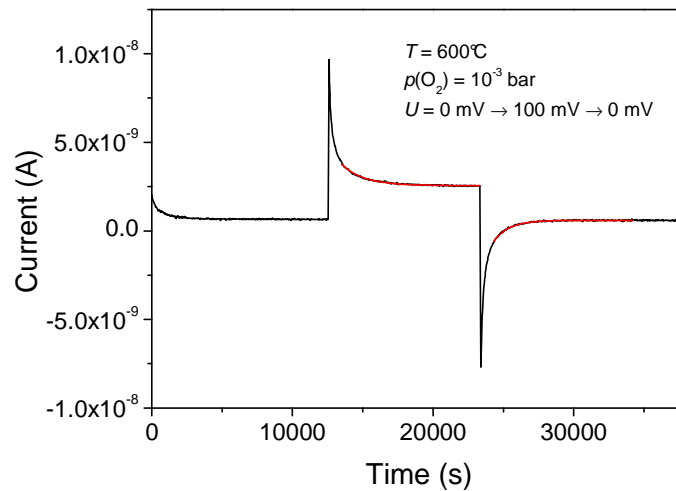

Fig. 4.30. Polarization and depolarization current measured on a $Bi_{0.5}Sr_{0.5}FeO_{3-\delta}$ thin-film electrochemical polarization cell upon stepwise changing the applied DC voltage from 0 mV to 100 mV and back to 0 mV. The red lines represent the best fits of equation (2.13)-(2.14) to the measured data.

In the present case, the polarization measurements were conducted at a $p(O_2)$ as low as 10^{-3} bar to suppress any leakage current caused by oxygen exchange on the BiSCF surface. The polarization direction of the DC voltage was chosen such that the electron-blocking electrode corresponded to the negatively charged electrode exposed to an effective $p(O_2)$ of 0.2 bar at 650°C and the standard applied voltage of 100 mV according to the Nernst equation. Thus, an extremely low effective $p(O_2)$ at the ScSZ electrode, for example, in the order of 10^{-6} bar at 650°C and a voltage of -100 mV was avoided, which could result in a decomposition of the perovskite phase. Measurements with positive polarization of the electron-blocking electrode carried out for each composition did not reveal a clear dependence of the results on the polarization direction though. Measurements at a higher applied voltage of 150 mV performed at the end of each measurement series typically yielded an increase of the steady-state polarization current consistent with ohmic behavior of the cell indicating contributions from the voltage-dependent electrode reactions to be negligible.

The current curve in Fig. 4.30 shows a small constant baseline current prior to switching on the voltage and no significant drift of the steady-state current

reached after each voltage change. Such a nearly ideal behavior of the measured current was typically observed at a temperature of 600°C and below. The only correction made before data evaluation in such cases consisted in shifting the curve vertically in order to set the baseline or steady-state depolarization current to 0 A. On the other hand, a certain linear drift of the baseline and "steady-state" polarization current prevailed at the maximum measuring temperature of 650°C even after equilibration of the samples at 0 V for about 4 h (for $Bi_{0.5}Sr_{0.5}FeO_{3-\delta}$ thin-film cells, the linear drift appeared to be even increased after switching on the voltage and was also discernible in the steady-state depolarization current). For data evaluation, the process provoking the current drift was considered to be independent of the polarization/depolarization of the BiSCF film. The drift effect was corrected for by subtraction of a straight line fitted to the baseline current or, for $Bi_{0.5}Sr_{0.5}FeO_{3-\delta}$ samples, the steady-state polarization and depolarization current, respectively.

The absence of strong drift effects at 600°C and below was taken as an indication that no significant long-term degradation of the BiSCF film occurred affecting ion transport at these temperatures. At 650°C, degradation might be more prominent, but a lowering of the maximum measuring temperature is not advisable if σ_{ion} and k^q are to be correlated due to the uncertainty in the activation energy of the inverse surface oxygen exchange resistance (chapter 4.3.5) and hence k^q. To estimate the impact of degradation, electrochemical polarization measurements were conducted following the measuring routine described in chapter 3.4.4. That is, a final DC measurement was performed after the temperature series at a temperature close to the initial temperature on one sample of each composition. The results are discussed in chapter 4.4.4.

In Fig. 4.31, the current data from Fig. 4.30 are represented in a $\ln((I_p - I_{p,inf})/A)$-versus-time (polarization current) and $\ln(I_d/A)$-versus-time (depolarization current) plot, respectively. At long times after a voltage change, the data can be
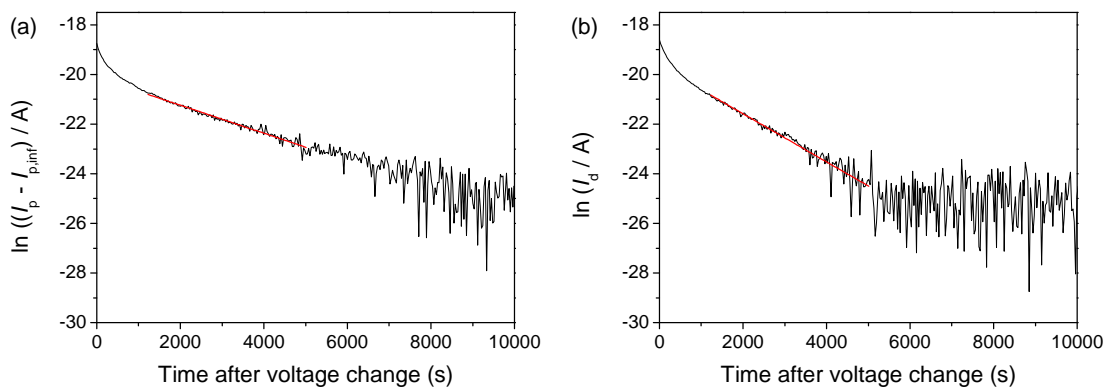

Fig. 4.31. Alternative representation of the (a) polarization and (b) depolarization current in Fig. 4.30. The red lines represent the best fits used to determine the chemical diffusion coefficient.

fitted with a straight line. From the slope of the line of best fit, the chemical diffusion coefficient is calculated using equation (2.15).

4.4.3   EIS Measurements on Thin-Film Electrochemical Polarization Cells

To identify contributions to the DC resistance other than the ion transport resistance of the BiSCF film, EIS measurements were carried out before and after each DC measurement. Fig. 4.32 shows a typical impedance spectrum obtained for a BiSCF polarization cell together with the equivalent circuit used for the evaluation. It was adapted from the equivalent circuit derived previously from a physical model for the electrochemical polarization of mixed conductors applying one or two blocking electrodes.[166]
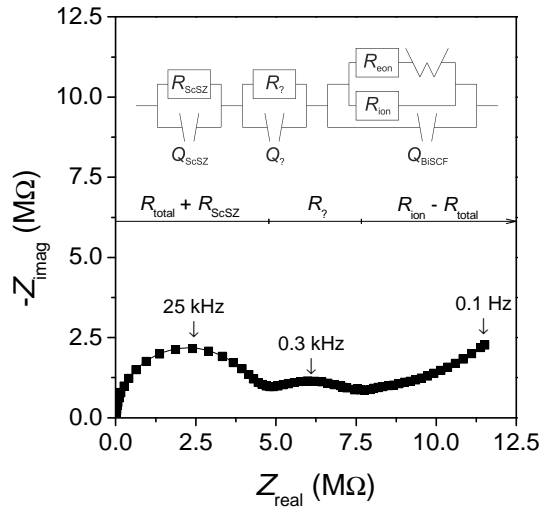

Fig. 4.32. Impedance spectrum of a $SrFeO_{3-\delta}$ thin-film electrochemical polarization cell at 600°C and $p(O_2)$ = 1 bar. The solid line represents the best fit obtained with the equivalent circuit shown in the inset (adapted from ref. [166]). For comparison, a DC resistance of 87 MΩ was received from a DC measurement performed before on the same sample under the same conditions.

The semicircle at high frequencies can be represented by a parallel RQ circuit. The high-frequency resistance R_{HF} is mainly attributed to the resistance of ion transport through the ScSZ electrode. From the results of electrical conductivity measurements on thin-film ScSZ, an ion transport resistance of about 0.8 MΩ under the conditions given in Fig. 4.32 is calculated in rather poor agreement with R_{HF}. However, the morphology of the nominally 1000 nm thin ScSZ electrodes might differ from that of the nominally 300 nm thin films used for electrical conductivity measurements, for example, exhibit a different grain size and/or a higher porosity. The activation energy of $(R_{HF})^{-1}$ of (1.22 ± 0.07) eV on average extracted from the temperature dependence of the impedance (e.g., Fig. 4.33), on the other hand, agrees well with the activation energy of the electrical conductivity of thin-film ScSZ of 1.16 eV between 500°C and 700°C. Furthermore, the high-

frequency resistance is nearly independent of the $p(O_2)$ or an applied DC bias as expected for the ScSZ resistance. The high-frequency resistance might additionally contain a contribution from the total electrical resistance of the BiSCF film, which is, however, lower than 1 MΩ for the compositions/conditions studied here and, therefore, negligible compared to the ScSZ contribution. The high-frequency capacitance typically exhibits a value of 1 pF much higher than the capacitance values anticipated for the dielectric relaxation in ScSZ and BiSCF (assuming a typical value for the capacitance due to dielectric relaxation of 2-20 pF cm^{-2} for a film with a thickness of 1 cm)[167] and grain boundary polarization in BiSCF (presuming a typical capacitance value of 1-10 nF cm^{-2} for a 1 cm thick film),[167] but might be assigned to grain boundary polarization in ScSZ. Alternatively, the high-frequency capacitance can be interpreted as a stray capacitance short-circuiting the other capacitive branches.
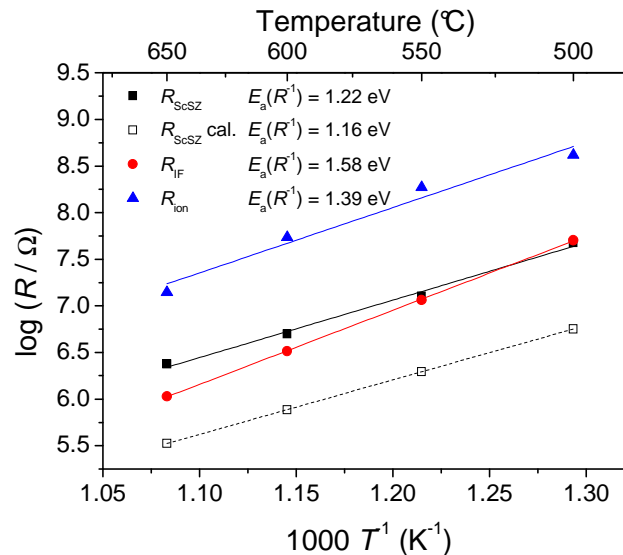

Fig. 4.33. Temperature dependence of the resistances measured by EIS and the ion transport resistance R_{ion} derived from DC measurements on a SrFeO$_{3-\delta}$ thin-film electrochemical polarization cell at $p(O_2) = 10^{-3}$ bar. Open symbols indicate the ion transport resistance of the ScSZ electrode calculated from the electrical ($\approx$ ionic) conductivity from thin-film measurements.

The semicircle at intermediate frequencies visible in Fig. 4.32 was not obtained for all samples. The resistance R_{IF} of the associated parallel RQ circuit exhibits an activation energy of the inverse quantity in the range of 1.05-1.58 eV and is nearly $p(O_2)$-independent. The intermediate-frequency semicircle might originate from slow transfer of oxide ions across the BiSCF-ScSZ interface. Due to the very small interfacial area between BiSCF and ScSZ, though, an interfacial capacitance much smaller than the capacitance deduced from the intermediate-frequency semicircle (0.1-10 nF, basically temperature- and $p(O_2)$-independent) would be expected based on standard values for the electrical double layer capacitance at the

interface between two solids (0.1-10 μF cm^{-2}).[167] Impedance contributions attributable to oxygen exchange at the reversible electrode or the Pt/ScSZ triple phase boundary are not likely to be noticed owing to the low surface oxygen exchange resistance of BiSCF (Table 4.4) and the absence of an electrode semicircle in impedance spectra recorded to determine the electrical conductivity of YSZ thin films. At low frequencies, the impedance shows a Warburg-type behavior, that is, a straight line at a phase angle of 45° merging into a semicircle, representing the stoichiometry polarization of the BiSCF by chemical diffusion.

4.4.4   Temperature Dependence of the Ionic Conductivity

The temperature dependence of the ionic conductivity from thin-film polarization measurements on some selected BiSCF compositions is displayed in Fig. 4.34a. Ionic conductivity values were derived from the DC resistance obtained from DC measurements (chapter 4.4.2) after subtraction of the ScSZ and, if necessary, intermediate-frequency resistance determined by EIS (chapter 4.4.3). For comparison, ionic conductivity data from literature and electrical conductivity measurements on bulk samples at low $p(O_2)$ (chapter 4.1.5) are shown as well.

Thin-film polarization measurements were carried out on SrFeO$_{3-\delta}$ as reference material since its ionic transport properties (and oxygen exchange kinetics) are already well investigated. Good agreement was found between the received ionic conductivity values for SrFeO$_{3-\delta}$ and those calculated via equation (2.16) and equation (2.17) from the chemical diffusion coefficients of Yoo et al.[168] and oxygen vacancy diffusion coefficients of Wang et al.[14] (using stoichiometry data from ref. [168] and in-house thermogravimetric measurements[169]) confirming the validity of the method (literature σ_{ion} values from electrical conductivity measurements at low $p(O_2)$[61, 170] might be overestimated owing to the absence of a clear ionic conductivity plateau). For Bi$_{0.5}$Sr$_{0.5}$FeO$_{3-\delta}$ fair agreement was observed between the ionic conductivity from thin-film and bulk measurements, respectively, at 600°C, but a higher activation energy was obtained from thin-film samples (Table 4.9) possibly due to a certain degree of film degradation (see below). The ionic conductivity of Bi$_{0.5}$Sr$_{0.5}$FeO$_{3-\delta}$ from the present measurements is higher than that reported by Niu et al. for Bi$_{0.5}$Sr$_{0.5}$FeO$_{3-\delta}$[100] and Brinkman et al. for Bi$_{0.4}$Sr$_{0.6}$FeO$_{3-\delta}$[88] from oxygen permeation experiments on bulk samples, but agrees reasonably well with that deduced from the chemical diffusion coefficients given by Niu et al. from electrical conductivity relaxation measurements on bulk Bi$_{0.5}$Sr$_{0.5}$FeO$_{3-\delta}$[100]

Brinkman et al. noticed an increase in the ionic conductivity from 3.7×10^{-3} S cm^{-1} for Bi$_{0.95}$Sr$_{0.05}$FeO$_{3-\delta}$ to 3.5×10^{-2} S cm^{-1} for Bi$_{0.2}$Sr$_{0.8}$FeO$_{3-\delta}$ at 800°C (which is close to the value derived from ref. [168] for SrFeO$_{3-\delta}$), that is, with increasing Sr content, and a drop of the conductivity to 5.1×10^{-3} S cm^{-1} for the intermediate composition Bi$_{0.4}$Sr$_{0.6}$FeO$_{3-\delta}$[88] The conductivity increase most
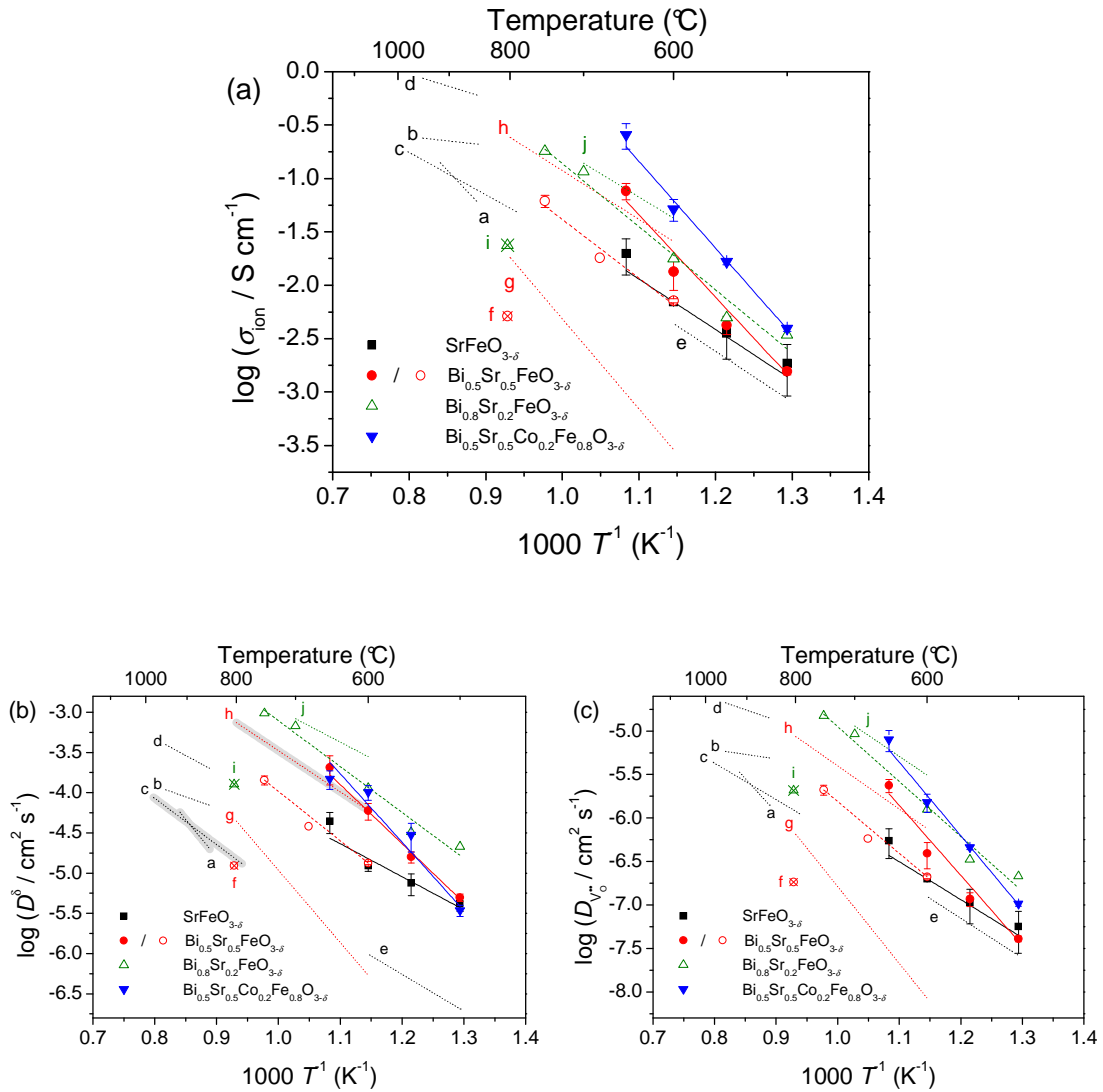
Fig. 4.34. Temperature dependence of (a) the ionic conductivity, (b) the chemical diffusion coefficient calculated via equation (2.15), and (c) the oxygen vacancy diffusion coefficient determined via equation (2.16) from electrochemical polarization measurements on two different thin-film samples at $p(O_2) = 10^{-3}$ bar (closed symbols/solid line of best fit) and 1-2 electrical conductivity measurements on bulk samples at low $p(O_2)$ (open symbols/dashed line of best fit). For comparison, literature data are shown for bulk samples (no symbol/dotted line of best fit) of $SrFeO_{3-\delta}$ (a:[171] from electrochemical polarization measurements, b[61] and d:[170] from electrical conductivity measurements at low $p(O_2)$, c:[168] from electrical conductivity relaxation measurements, and e:[14] from isotope exchange experiments on thin films), $Bi_{0.4}Sr_{0.6}FeO_{3-\delta}$ (f:[88] from oxygen permeation measurements), $Bi_{0.5}Sr_{0.5}FeO_{3-\delta}$ (g:[100] from oxygen permeation and h:[100] from electrical conductivity relaxation), $Bi_{0.7}Sr_{0.3}FeO_{3-\delta}$ (i:[88] from oxygen permeation), and $Bi_{0.95}Sr_{0.05}FeO_{3-\delta}$ (j:[88] from electrical conductivity measurements at low $p(O_2)$) measured directly (for D^δ indicated by gray bars) or converted using the oxygen nonstoichiometry data from TG analyses.

probably results from an increase in the oxygen vacancy concentration with increasing Sr content, and the conductivity drop was suggested to be a consequence of oxygen vacancy ordering in the intermediate composition. High-

Table 4.9. Average activation energies of the ionic conductivity, the chemical diffusion coefficient calculated via equation (2.15), and the oxygen vacancy diffusion coefficient determined via equation (2.16) from electrochemical polarization measurements on two different thin-film samples at $p(O_2) = 10^{-3}$ bar and 1-2 electrical conductivity measurements on pellets at low $p(O_2)$. Scattering ranges refer to fitting ($Bi_{0.8}Sr_{0.2}FeO_{3-\delta}$) or statistical errors (others), the values measured on degraded thin films were typically by about 40% smaller.

		$E_a(\sigma_{ion})$ (eV)	$E_a(D^\delta)$ (eV)	$E_a(D_{V_O^{\bullet\bullet}})$ (eV)
$SrFeO_{3-\delta}$	thin film	0.99 ± 0.40	0.91 ± 0.20	0.95 ± 0.40
$Bi_{0.5}Sr_{0.5}FeO_{3-\delta}$	thin film	1.55 ± 0.06	1.45 ± 0.12	1.62 ± 0.06
$Bi_{0.5}Sr_{0.5}FeO_{3-\delta}$	pellet	1.09 ± 0.05	1.21 ± 0.05	1.17 ± 0.05
$Bi_{0.8}Sr_{0.2}FeO_{3-\delta}$	pellet	1.17 ± 0.10	1.13 ± 0.09	1.25 ± 0.10
$Bi_{0.5}Sr_{0.5}Co_{0.2}Fe_{0.8}O_{3-\delta}$	thin film	1.66 ± 0.10	1.67 ± 0.18	1.73 ± 0.10

temperature neutron diffraction experiments on $Bi_{0.5}Sr_{0.5}FeO_{3-\delta}$ powder (chapter 4.1.1), however, did not yield evidence for the formation of an ordered arrangement of oxygen vacancies in agreement with the conductivity values received for $Bi_{0.5}Sr_{0.5}FeO_{3-\delta}$ being comparable to or even higher than those for $SrFeO_{3-\delta}$

The reports of Brinkman et al. on the ionic conductivity of the composition $Bi_{0.95}Sr_{0.05}FeO_{3-\delta}$ with high Bi content are, nevertheless, contradictory. The ionic conductivity of bulk $Bi_{0.95}Sr_{0.05}FeO_{3-\delta}$ from electrical conductivity measurements at low $p(O_2)$ was shown to be significantly higher than that from oxygen permeation experiments on $Bi_{0.95}Sr_{0.05}FeO_{3-\delta}$ or $Bi_{0.7}Sr_{0.3}FeO_{3-\delta}$[88] but agrees well with the results from the present measurements on bulk $Bi_{0.8}Sr_{0.2}FeO_{3-\delta}$ suggesting some error in the derivation of σ_{ion} from the oxygen permeation flux. Finally, the ionic conductivity of thin films appears to increase when a small amount of Co is introduced on the perovskite B site in accordance with the trend reported previously for the oxygen permeation flux of $Bi_{0.3}Sr_{0.7}Co_{1-y}Fe_yO_{3-\delta}$ ($y = 0.8$ and 1).[99] However, a slight overestimation of the conductivity values for the Co-containing composition due to leakage can not be excluded as pointed out in chapter 4.4.5.

The ionic conductivity values obtained for thin-film samples from the second DC measurement at 600°C, performed to estimate the influence of degradation (chapter 4.4.2), were typically by about 40% smaller than those from the first measurement indicating a moderate modification of the absolute values in Fig. 4.34a due to degradation. Accordingly, the activation energies calculated from σ_{ion} at 550°C and 500°C and the value deduced from the final measurement at 600°C were by about 40% lower than the activation energies from all measurements except the last one. The activation energies of the ionic conductivity from thin-film electrochemical polarization measurements appear to be influenced stronger by degradation effects than those of the inverse surface resistance from EIS measurements on thin-film microelectrodes (chapter 4.3.5) possibly due to the longer overall measurement duration. Furthermore, a certain degree of reactivity

between the different components of the electrochemical polarization cells, not detectable by the available analytical methods, might contribute to the observed conductivity changes as well.

Fig. 4.35 shows the temperature dependence of the different diffusion coefficients derived for a $SrFeO_{3-\delta}$ and a $Bi_{0.5}Sr_{0.5}FeO_{3-\delta}$ sample from thin-film polarization measurements: (i) the chemical diffusion coefficient calculated via equation (2.15) from the slope of the straight line fitted to the $\ln((I_p - I_{p,inf})/A)$-versus-time and $\ln(I_d/A)$-versus-time plot (e.g., Fig. 4.31), respectively; (ii) the oxygen vacancy diffusion coefficient determined applying the Nernst-Einstein equation (equation (2.16)) from σ_{ion} and the oxygen vacancy concentration at a $p(O_2)$ of 0.1 bar (the average oxygen partial pressure in the whole film arrangement at an applied voltage of 100 mV) from thermogravimetric measurements (chapter 4.1.3); (iii) the chemical and oxygen vacancy diffusion coefficient obtained by conversion of the diffusion coefficients (i) and (ii) according to equation (2.17) using $c_{V_O^{\cdot\cdot}}$ at a $p(O_2)$ of 0.1 bar and the average thermodynamic factor ω_0 from thermogravimetric measurements at high and low oxygen partial pressures. For $Bi_{0.5}Sr_{0.5}Co_{0.2}Fe_{0.8}O_{3-\delta}$ for which TG data are not available, the calculations were performed based on the oxygen nonstoichiometry of $Bi_{0.5}Sr_{0.5}FeO_{3-\delta}$
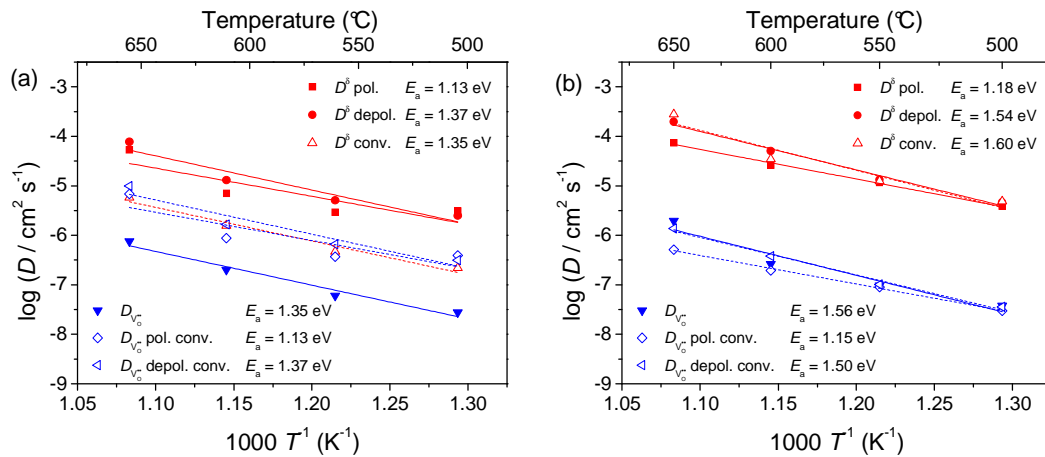

Fig. 4.35. Temperature dependence of the chemical diffusion coefficients and oxygen vacancy diffusion coefficients measured directly on a thin-film electrochemical polarization cell of (a) $SrFeO_{3-\delta}$ and (b) $Bi_{0.5}Sr_{0.5}FeO_{3-\delta}$ and converted via the thermodynamic factor from the measured diffusion coefficients at $p(O_2) = 10^{-3}$ bar.

A difference of about one order of magnitude was found between the diffusion coefficients (i) and (ii) and those assessed by use of equation (2.17) for $SrFeO_{3-\delta}$ However, the thermodynamic factors in the thin films might deviate from the values extracted from thermogravimetric measurements on bulk samples used for the conversion, for example, due to changes in the defect chemistry resulting from

mechanical stress (see also the discrepancy in C^δ of bulk and thin-film samples of up to a factor of 12, chapter 4.3.1). The presence of significant mechanical stress in SrFeO$_{3-\delta}$ films seems probable considering the proneness of films of the related composition Bi$_{0.2}$Sr$_{0.8}$FeO$_{3-\delta}$ to form cracks (chapter 4.2.2). For the other investigated compositions, the discrepancy between "original" and converted diffusion coefficients is negligible.

The chemical diffusion coefficients (Fig. 4.34b) deduced from the slope of the line of best fit/relaxation time attributable to the current decay are large in particular compared to the values from literature for SrFeO$_{3-\delta}$ (regardless of the method applied) and the present measurements on bulk Bi$_{0.5}$Sr$_{0.5}$FeO$_{3-\delta}$. Thus, it can not be excluded that the relaxation of the oxygen stoichiometry particularly in the SrFeO$_{3-\delta}$ thin films is accelerated, for example, by leakage. This might also be an explanation for the discrepancy between original and converted diffusion coefficients discussed above. A clear dependence of D^δ from thin-film polarization measurements on the cation composition was not revealed. The trends observed for the oxygen vacancy diffusion coefficient calculated via equation (2.16) (Fig. 4.34c) reflect the trends depicted before for the ionic conductivity: $D_{V_O^{\bullet\bullet}}$ from thin-film measurements in most cases agrees well with the results from literature and investigations on bulk samples, and the oxygen vacancy diffusion coefficient and thus the oxygen vacancy mobility increases upon introduction of Bi and Co.

4.4.5   Oxygen Partial Pressure Dependence of the Ionic Conductivity

To examine the $p(O_2)$ dependence of the ionic conductivity, a polarization measurement was conducted at 600°C and a $p(O_2)$ of 1 bar after acquisition of each temperature series. In agreement with the behavior revealed for the oxygen vacancy concentration (Fig. 4.6), the ionic conductivity of Co-free thin films shows only weak dependence on the $p(O_2)$ (Fig. 4.36a). The exponent n in $\sigma_{ion} \propto (p(O_2))^n$ amounts to -0.05 for SrFeO$_{3-\delta}$ (corresponding nearly to the exponent for the oxygen vacancy concentration) and 0.03 ± 0.01 for Bi$_{0.5}$Sr$_{0.5}$FeO$_{3-\delta}$. The low $p(O_2)$ dependence of the ionic conductivity also indicates good sealing of the electrochemical cell, as a stronger variation with the $p(O_2)$ was expected in the presence of significant oxygen exchange on the BiSCF surface. Only for Bi$_{0.5}$Sr$_{0.5}$Co$_{0.2}$Fe$_{0.8}$O$_{3-\delta}$ thin films, a considerable $p(O_2)$ dependence of the ionic conductivity is observed possibly resulting from insufficient sealing yielding a n value of 0.18 ± 0.02. SEM analyses evidenced the presence of slight cracks on the surface of the Al$_2$O$_3$ sealing layers of the Bi$_{0.5}$Sr$_{0.5}$Co$_{0.2}$Fe$_{0.8}$O$_{3-\delta}$ samples not detected on the sealing layer, for example, of a Bi$_{0.5}$Sr$_{0.5}$FeO$_{3-\delta}$ sample. From the SEM images it is not possible to decide whether these cracks extend to the BiSCF film and, therefore, enable oxygen exchange on the BiSCF surface. Nevertheless, it has to be kept in mind that the σ_{ion} values for Bi$_{0.5}$Sr$_{0.5}$Co$_{0.2}$Fe$_{0.8}$O$_{3-\delta}$ in Fig. 4.34 might be overestimated due to leakage.
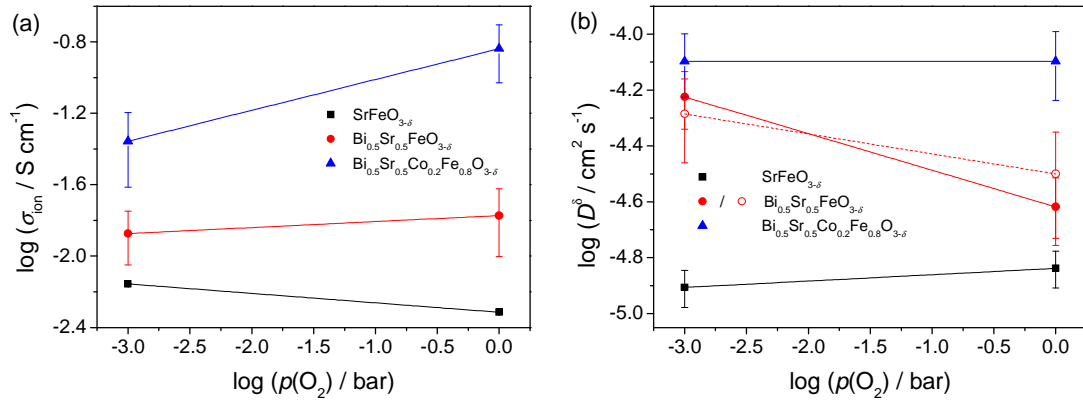
Fig. 4.36. Oxygen partial pressure dependence of (a) the ionic conductivity and (b) the chemical diffusion coefficient calculated via equation (2.15) measured on two different thin-film electrochemical polarization cells of each composition at 600°C. Open symbols indicate the chemical diffusion coefficients determined from the ionic conductivity via the thermodynamic factor (equation (2.16)-(2.17)).

The chemical diffusion coefficients extracted from the current relaxation time exhibit a weak or no dependence on the $p(O_2)$ for $SrFeO_{3-\delta}$ ($n = 0.02 \pm 0.02$ in $D^\delta \propto (p(O_2))^n$) and $Bi_{0.5}Sr_{0.5}Co_{0.2}Fe_{0.8}O_{3-\delta}$ ($n = 0 \pm 0.01$), whereas D^δ of $Bi_{0.5}Sr_{0.5}FeO_{3-\delta}$ ($n = -0.14 \pm 0.02$) is more strongly $p(O_2)$-dependent (Fig. 4.36b). The reason for this effect might be the significant $p(O_2)$ dependence of the thermodynamic factor of $Bi_{0.5}Sr_{0.5}FeO_{3-\delta}$ (chapter 4.1.3). The D^δ values calculated from the ionic conductivity via the thermodynamic factor display a comparably strong $p(O_2)$ dependence ($n = -0.08 \pm 0.01$) supporting this hypothesis.

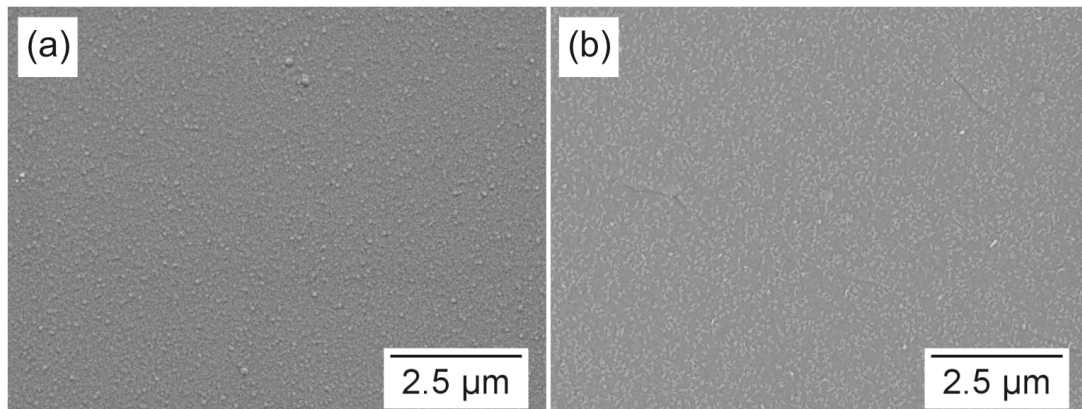*Fig. 4.37. SEM images of the surface of the nominally 300 nm thin Al_2O_3 sealing layers of a (a) $Bi_{0.5}Sr_{0.5}FeO_{3-\delta}$ and (b) $Bi_{0.5}Sr_{0.5}Co_{0.2}Fe_{0.8}O_{3-\delta}$ thin-film electrochemical polarization cell recorded after the polarization measurements.*

4.5   Concluding Discussion

In the following sections, the oxygen exchange performance, quantified by the effective surface oxygen exchange rate constant k^q, is compared for different BiSCF compositions. The exchange rate constants were calculated via equation (2.8) from the surface resistance from EIS measurements on microelectrode and, where available, macroscopic samples (Table 4.4 and Table 4.6). For the Co-containing BiSCF members, for which TG data are not available, the oxide ion concentration was estimated based on the oxygen nonstoichiometry δ of $Bi_{0.5}Sr_{0.5}FeO_{3-\delta}$ Furthermore, the interrelation between the oxygen exchange performance and selected bulk properties is studied. Since the bulk properties are intimately connected with the respective surface properties, such a study is expected to provide insight into the oxygen exchange mechanism. Literature data acquired on related perovskites in a similar way are also included in the discussion. A brief assessment of the suitability of BiSCF perovskites as SOFC cathode materials is given at the end of the chapter.

4.5.1   The Effective Surface Oxygen Exchange Rate Constants of BiSCF

Fig. 4.38 shows the effective surface oxygen exchange rate constants k^q obtained for the different BiSCF compositions. Evidently, the exchange rate constant of BiSCF increases noticeably with increasing fraction of Sr on the perovskite A site, but a particularly strong increase in k^q by about a factor of 3 is achieved upon introduction of Co on the B site of the perovskite. The performance enhancement due to Co introduction is more pronounced than for the corresponding La-
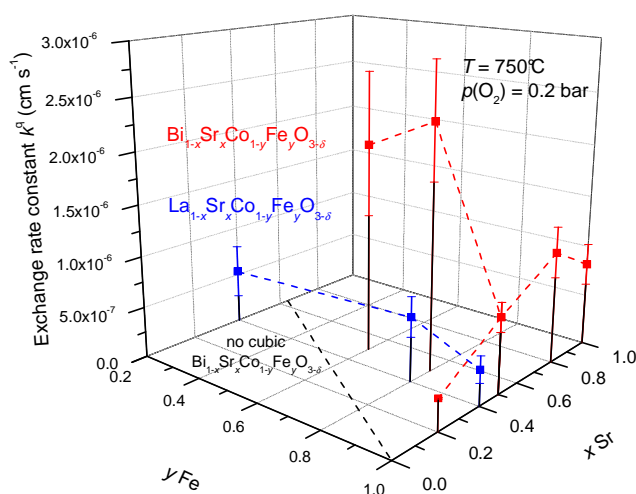

Fig. 4.38. Effective surface oxygen exchange rate constants k^q of BiSCF perovskites plotted versus the Sr and Fe content, respectively. For comparison, literature data for $SrFeO_{3-\delta}$[14] and LSCF[10] are shown.

containing compositions and results in a better oxygen exchange performance in particular of Co-containing BiSCF compared to the respective LSCF members. However, as mentioned in chapter 4.2.1, the presence and catalytic activity of Co_3O_4 impurities can not be excluded for $Bi_{0.5}Sr_{0.5}Co_{0.4}Fe_{0.6}O_{3-\delta}$ thin films deposited at low $p(O_2)$. On the other hand, no indications for the presence of Co_3O_4 were found in any of the $Bi_{0.5}Sr_{0.5}Co_{0.2}Fe_{0.8}O_{3-\delta}$ thin-film samples deposited at the standard $p(O_2)$ and exhibiting a comparably high oxygen exchange rate constant, suggesting that the measured k^q values in most cases reflect the true properties of the perovskite materials. Therefore, it can be concluded that the substitution of La^{3+} by Bi^{3+} leads to an improvement of the oxygen exchange kinetics, although the excellent performance of Ba-containing perovskites could not be achieved.

4.5.2   Interrelation Between the Exchange Rate Constant and the Electronic Conductivity

The impact of the electronic conductivity on the catalytic surface oxygen exchange can be estimated from the plot of k^q versus σ_{eon} (Fig. 4.39). A linear correlation between the exchange rate constant and the electronic conductivity is found for $(Ba,Bi,Sr)(Co,Fe)O_{3-\delta}$ perovskites indicated by a slope of the line of best fit to the data in log-log representation of 0.95. In the region of higher electronic conductivities, that is, for the La-containing compositions, this correlation appears to be no longer valid, and the exchange rate constant is governed by other factors instead. The linear correlation revealed for $(Ba,Bi,Sr)(Co,Fe)O_{3-\delta}$ can be interpreted in two ways: (i) The availability of electronic charge carriers, indeed, determines the oxygen exchange rate, since the respective species are involved either directly in the rate-determining step or in preceding reaction steps. As the observed
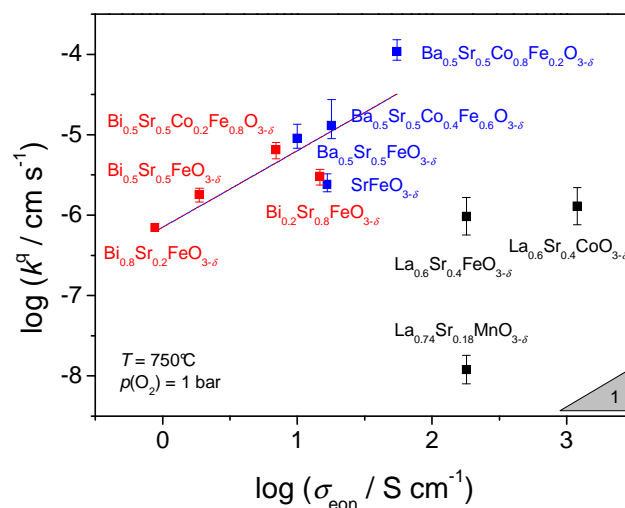

Fig. 4.39. *Effective surface oxygen exchange rate constants k^q of BiSCF perovskites plotted versus the electronic conductivity of the bulk sample ($Bi_{0.2}Sr_{0.8}FeO_{3-\delta}$) or thin films (others). For comparison, literature data for LSM,[11, 172] LSCF,[10, 173-174] and BaSCF[14, 61, 175] are shown.*

correlation is linear, a reaction order of electronic charge carriers of 1 rather than 2 has to be assumed pointing towards superoxide formation (equation (2.1)) as the rds. However, in previous investigations on BaSCF, this reaction step was ruled out to be rate-determining since it could not explain the strong dependence of the oxygen exchange rate on the oxygen vacancy migration rate.[14, 68] Alternatively, the approach of an oxygen vacancy to adsorbed superoxide comes into question as rate-determining step concluded before to be rate-determining for BaSCF perovskites.[56] (ii) Both k^q and σ_{eon} are influenced independently, but in a similar way by another factor, for example, the fraction of Co on the perovskite B site. Based on the experimental results, it is not possible to decide which of the two interpretations is correct in the present case.

4.5.3   Interrelation Between the Exchange Rate Constant and the Oxidation Enthalpy

The oxidation enthalpy exerts influence on the concentration of several species involved in the oxygen exchange reaction, namely, oxygen vacancies and adsorbed oxygen species. In Fig. 4.40, the effective surface oxygen exchange rate constants k^q are plotted versus ΔH_{ox}^0. Similar to the behavior found for BaSCF perovskites, a clear correlation between k^q and the oxidation enthalpy is not discernible for the investigated BiSCF compositions. However, the ΔH_{ox}^0 values vary only by 1.2 eV within the $(Ba,Bi,Sr)(Co,Fe)O_{3-\delta}$ family. This variation is smaller than the variation reported for $(La,Sr)(Mn,Co,Fe)O_{3-\delta}$ perovskites, the oxidation enthalpies of which range from -0.6 eV to -2.8 eV.[69] As a consequence, the oxygen nonstoichiometry δ of the La-containing compositions varies by several orders of magnitude giving
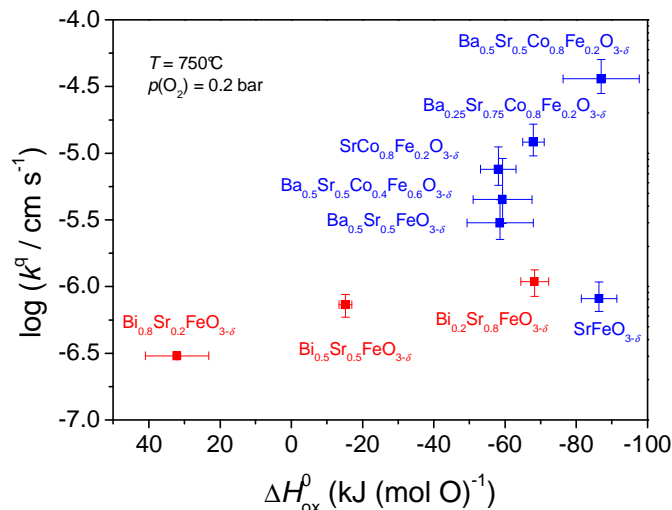

Fig. 4.40. Effective surface oxygen exchange rate constants k^q of BiSCF perovskites plotted versus the oxidation enthalpy from DSC measurements at 750°C (for $Bi_{0.8}Sr_{0.2}FeO_{3-\delta}$ the oxidation enthalpy at 600°C is given). Literature data for BaSCF[14, 129] are shown for comparison.

rise to a clear correlation between k^q and ΔH_{ox}^0.[69] Compared to (La,Sr)(Mn,Co,Fe)O$_{3-\delta}$ perovskites, the oxidation enthalpy of (Ba,Bi,Sr)(Co,Fe)O$_{3-\delta}$ might rather be considered constant and hence can not be expected to exhibit a correlation with the oxygen exchange rate constant.

4.5.4 Interrelation Between the Exchange Rate Constant and the Ionic Conductivity

Fig. 4.41 displays the relationship between the ionic conductivity and the effective rate constant of surface oxygen exchange for BiSCF and some of the compositions studied previously. For BaSCF perovskites, the reported linear correlation between σ_{ion} and the exchange rate constant[14] is reflected by a slope of the line of best fit in Fig. 4.41 of 1.44. Regarding BiSCF, both σ_{ion} and k^q appear to increase when moving from the Co-free compositions to Co-containing BiSCF. The data set for the Bi-containing perovskites might be fitted in log-log representation with a straight line with a slope of 1.24 suggesting a linear correlation between the ionic conductivity and the exchange rate constant. Similar as for BaSCF, the relationship between these two quantities is not influenced by changes in the oxidation enthalpy (chapter 4.5.3) and hence the adsorbate coverage decreasing the slope to about 0.5 in the case of (Ln,Sr)(Mn,Co,Fe)O$_{3-\delta}$ (Ln = La and Sm) perovskites.[67, 69] The present results imply that not only for the Ba-containing compositions, but also for BiSCF, the high oxygen exchange rate can directly be related to the high diffusivity of oxygen vacancies, and that the diffusion of oxygen vacancies is involved in the rate-determining step of the surface oxygen exchange reaction also for BiSCF
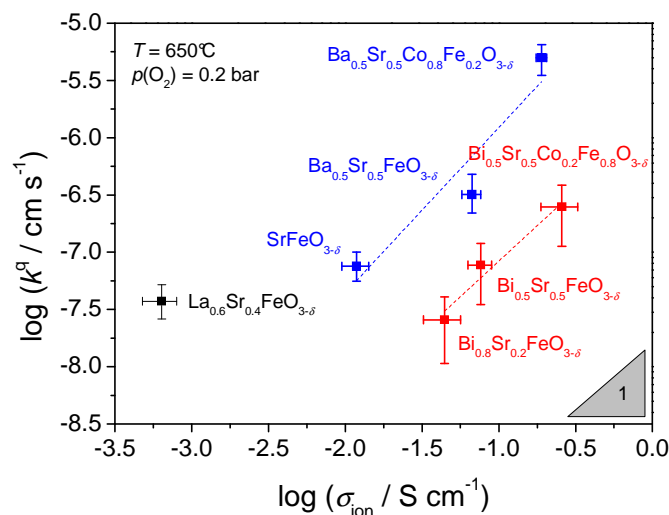

Fig. 4.41. Effective surface oxygen exchange rate constants k^q of BiSCF perovskites plotted versus the ionic conductivity from electrical conductivity measurements on bulk samples at low $p(O_2)$ (Bi$_{0.8}$Sr$_{0.2}$FeO$_{3-\delta}$) and thin-film electrochemical polarization measurements (other Bi-containing compositions). For comparison, literature data for LSCF[10, 100] and BaSCF[14] are shown.

perovskites. However, these conclusions have to be taken with caution, since the σ_{ion} value obtained for $Bi_{0.5}Sr_{0.5}Co_{0.2}Fe_{0.8}O_{3-\delta}$ from electrochemical polarization measurements might still be overestimated due to leakage (chapter 4.4.5).

4.5.5   BiSCF Perovskites as SOFC Cathode Materials

From the present study, it becomes apparent that BiSCF perovskites offer a number of advantages making them promising candidates for applications as SOFC cathode materials. They exhibit:

(i)   a high catalytic activity for surface oxygen exchange, higher than that of the La-containing compositions and only surpassed by BaSCF;

(ii)   a high ionic conductivity, comparable to that of BaSCF perovskites and apparently accelerating the surface oxygen exchange reaction;

(iii)   a high chemical stability of the Co-free compositions towards YSZ as a common SOFC electrolyte, higher than that of LSCF and BaSCF;

(iv)   a low tendency towards carbonate formation, distinctly lower than that of BaSCF;

(v)   a low thermochemical expansion coefficient of the composition with not too high Sr content, lower than that of BaSCF and comparable to that of LSCF;

(vi)   no structural phase transformations of the Co-free compositions at typical SOFC operating temperatures; for Co-containing BiSCF, low-temperature phase transitions can not be excluded.

On the other hand, the comparatively low electronic conductivity of BiSCF perovskites proved to interfere with the present measurements, that is, lead to the appearance of additional features in microelectrode impedance spectra. The complications are to some extent due to the extreme aspect ratio of the investigated thin-film samples chosen to address the interfacial properties of the materials. However, in a conventional thick film cathode with higher aspect ratio, the low electronic conductivity might affect the electrode performance to a lesser degree. Alternatively, admixing of electron-conducting perovskite or metallic phases might help to overcome possible limitations. Furthermore, it needs to be clarified if the evaporation of Bi, observed in the present study upon heating of $Bi_{0.5}Sr_{0.5}FeO_{3-\delta}$ to 700°C under vacuum, is significant under SOFC operating conditions. Considerable Bi evaporation is, however, not expected to occur at the relatively high oxygen partial pressure prevailing at the cathode side of a SOFC.

    In view of the large number of advantages listed above, it appears very worthwhile to consider BiSCF perovskites for applications as cathode materials in future high-performance SOFCs.

Acknowledgments

I thank my fellow PhD representatives from the two Max Planck Institutes in Stuttgart for the great time we spent together, as well as all other PhD representatives for informative lectures, helpful seminars, and unforgettable excursions.

I thank all current and former colleagues from the department of Professor Maier for assisting me with experiments, sacrificing their time for insightful discussions or otherwise contributing to a very pleasant working atmosphere.

I am grateful to my grandparents for their loving support and constant encouragement.

My dearest thanks go to Adarsh Sagar for his understanding and patience defying all adversities in the past years.

And finally I would like to thank my parents, who contributed more to the completion of this work than I ever could.

References

[1]   Bundesministerium für Wirtschaft und Technologie, Bundesministerium für Umwelt, Naturschutz und Reaktorsicherheit, "Energiekonzept für eine umweltschonende, zuverlässige und bezahlbare Energieversorgung 28. September 2010" to be found under http://www.bmu.de/files/pdfs/allgemein/application/pdf/energiekonzept _bundesregierung.pdf, **2010**.

[2]   W. R. Grove, *London Edinburgh Philos. Mag. J. Sci.* **1839**, *14*, 127-130.

[3]   T. Horita, K. Yamaji, N. Sakai, H. Yokokawa, T. Kawada, T. Kato, *Solid State Ionics* **2000**, *127*, 55-65.

[4]   T. Kawada, J. Suzuki, M. Sase, A. Kaimai, K. Yashiro, Y. Nigara, J. Mizusaki, K. Kawamura, H. Yugami, *J. Electrochem. Soc.* **2002**, *149*, E252-E259.

[5]   L. M. van der Haar, M. W. den Otter, M. Morskate, H. J. M. Bouwmeester, H. Verweij, *J. Electrochem. Soc.* **2002**, *149*, J41-J46.

[6]   H. J. M. Bouwmeester, M. W. Den Otter, B. A. Boukamp, *J. Solid State Electrochem.* **2004**, *8*, 599-605.

[7]   E. Koep, D. S. Mebane, R. Das, C. Compson, M. Liu, *Electrochem. Solid-State Lett.* **2005**, *8*, A592-A595.

[8]   A. Bieberle-Huetter, M. Sogaard, H. L. Tuller, *Solid State Ionics* **2006**, *177*, 1969-1975.

[9]   S. B. Adler, X. Y. Chen, J. R. Wilson, *J. Catal.* **2007**, *245*, 91-109.

[10]   F. S. Baumann, J. Fleig, G. Cristiani, B. Stuhlhofer, H.-U. Habermeier, J. Maier, *J. Electrochem. Soc.* **2007**, *154*, B931-B941.

[11]   J. Fleig, H. R. Kim, J. Jamnik, J. Maier, *Fuel Cells (Weinheim, Ger.)* **2008**, *8*, 330-337.

[12]   M. Mosleh, M. Sogaard, P. V. Hendriksen, *J. Electrochem. Soc.* **2009**, *156*, B441-B457.

[13]   A. V. Berenov, A. Atkinson, J. A. Kilner, E. Bucher, W. Sitte, *Solid State Ionics* **2010**, *181*, 819-826.

[14]   L. Wang, R. Merkle, J. Maier, *J. Electrochem. Soc.* **2010**, *157*, B1802-B1808.

[15]   Y. Takeda, R. Kanno, M. Noda, Y. Tomida, O. Yamamoto, *J. Electrochem. Soc.* **1987**, *134*, 2656-2661.

[16]   O. Yamamoto, Y. Takeda, R. Kanno, M. Noda, *Solid State Ionics* **1987**, *22*, 241-246.

[17]   A. Endo, M. Ihara, H. Komiyama, K. Yamada, *Solid State Ionics* **1996**, *86-88*, 1191-1195.

[18]   J. Mizusaki, T. Saito, H. Tagawa, *J. Electrochem. Soc.* **1996**, *143*, 3065-3073.

[19]   T. Ioroi, T. Hara, Y. Uchimoto, Z. Ogumi, Z. Takehara, *J. Electrochem. Soc.* **1997**, *144*, 1362-1370.

[20]   A. Endo, S. Wada, C. J. Wen, H. Komiyama, K. Yamada, *J. Electrochem. Soc.* **1998**, *145*, L35-L37.

[21]   T. Ioroi, T. Hara, Y. Uchimoto, Z. Ogumi, Z. Takehara, *J. Electrochem. Soc.* **1998**, *145*, 1999-2004.

[22]   T. Kawada, K. Masuda, J. Suzuki, A. Kaimai, K. Kawamura, Y. Nigara, J. Mizusaki, H. Yugami, H. Arashi, N. Sakai, H. Yokokawa, *Solid State Ionics* **1999**, *121*, 271-279.

[23]   V. Brichzin, J. Fleig, H.-U. Habermeier, J. Maier, *Electrochem. Solid-State Lett.* **2000**, *3*, 403-406.

[24]   A. Endo, H. Fukunaga, C. Wen, K. Yamada, *Solid State Ionics* **2000**, *135*, 353-358.

[25]   C. A. Mims, N. I. Joos, P. A. W. van der Heide, A. J. Jacobson, C. Chen, C. W. Chu, B. I. Kim, S. S. Perry, *Electrochem. Solid-State Lett.* **2000**, *3*, 59-61.

[26]   Y. L. Yang, C. L. Chen, S. Y. Chen, C. W. Chu, A. J. Jacobson, *J. Electrochem. Soc.* **2000**, *147*, 4001-4007.

[27]   A. Ringuede, J. Fouletier, *Solid State Ionics* **2001**, *139*, 167-177.

[28]   Y. M. L. Yang, A. J. Jacobson, C. L. Chen, G. P. Luo, K. D. Ross, C. W. Chu, *Appl. Phys. Lett.* **2001**, *79*, 776-778.

[29]   V. Brichzin, J. Fleig, H.-U. Habermeier, G. Cristiani, J. Maier, *Solid State Ionics* **2002**, *152*, 499-507.

[30]   N. Imanishi, T. Matsumura, Y. Sumiya, K. Yoshimura, A. Hirano, Y. Takeda, D. Mori, R. Kanno, *Solid State Ionics* **2004**, *174*, 245-252.

[31]   F. S. Baumann, J. Fleig, M. Konuma, U. Starke, H.-U. Habermeier, J. Maier, *J. Electrochem. Soc.* **2005**, *152*, A2074-A2079.

[32]   E. Koep, C. Compson, M. L. Liu, Z. P. Zhou, *Solid State Ionics* **2005**, *176*, 1-8.

[33]   R. Radhakrishnan, A. V. Virkar, S. C. Singhal, *J. Electrochem. Soc.* **2005**, *152*, A210-A218.

[34]   F. S. Baumann, J. Fleig, H.-U. Habermeier, J. Maier, *Solid State Ionics* **2006**, *177*, 1071-1081.

[35]   J. Fleig, F. S. Baumann, V. Brichzin, H. R. Kim, J. Jamnik, G. Cristiani, H.-U. Habermeier, J. Maier, *Fuel Cells (Weinheim, Ger.)* **2006**, *6*, 284-292.

[36]   D. Mori, H. Oka, Y. Suzuki, N. Sonoyama, A. Yamada, R. Kanno, Y. Sumiya, N. Imanishi, Y. Takeda, *Solid State Ionics* **2006**, *177*, 535-540.

[37]   G. J. la O', B. Yildiz, S. McEuen, Y. Shao-Horn, *J. Electrochem. Soc.* **2007**, *154*, B427-B438.

[38]   M. Prestat, A. Infortuna, S. Korrodi, S. Rey-Mermet, P. Muralt, L. J. Gauckler, *J. Electroceram.* **2007**, *18*, 111-120.

[39]   J. Januschewsky, M. Ahrens, A. Opitz, F. Kubel, J. Fleig, *Adv. Funct. Mater.* **2009**, *19*, 3151-3156.

[40]   G. J. la O', Y. Shao-Horn, *J. Electrochem. Soc.* **2009**, *156*, B816-B824.

[41]   J. W. Lee, Z. Liu, L. Yang, H. Abernathy, S. H. Choi, H. E. Kim, M. L. Liu, *J. Power Sources* **2009**, *190*, 307-310.

[42]   R. Merkle, J. Maier, J. Fleig in *Handbook of Fuel Cells - Fundamentals, Technology and Applications, Vol. 5* (Eds.: W. Vielstich, H. Yokokawa, H. A. Gasteiger), John Wiley & Sons, New York, **2009**, pp. 425-440.

[43]   H. Xiong, B. K. Lai, A. C. Johnson, S. Ramanathan, *J. Power Sources* **2009**, *193*, 589-592.

[44]   B. A. Boukamp, N. Hildenbrand, P. Nammensma, D. H. A. Blank, *Solid State Ionics* **2011**, *192*, 404-408.

[45]   N. J. Simrick, A. Bieberle-Huetter, T. M. Ryll, J. A. Kilner, A. Atkinson, J. L. M. Rupp, *Solid State Ionics* **2012**, *206*, 7-16.

[46]   Z. P. Shao, S. M. Haile, *Nature* **2004**, *431*, 170-173.

[47]   F. S. Baumann, J. Fleig, H.-U. Habermeier, J. Maier, *Solid State Ionics* **2006**, *177*, 3187-3191.

[48]   L. Wang, R. Merkle, F. S. Baumann, J. Fleig, J. Maier, *ECS Trans.* **2007**, *7*, 1015-1024.

[49]   B. Liu, X. B. Chen, Y. L. Dong, S. S. Mao, M. J. Cheng, *Adv. Energy Mater.* **2011**, *1*, 343-346.

[50]   S. Svarcova, K. Wiik, J. Tolchard, H. J. M. Bouwmeester, T. Grande, *Solid State Ionics* **2008**, *178*, 1787-1791.

[51]   D. N. Mueller, R. A. De Souza, T. E. Weirich, D. Roehrens, J. Mayer, M. Martin, *Phys. Chem. Chem. Phys.* **2010**, *12*, 10320-10328.

[52]   Z. S. Duan, M. Yang, A. Yan, Z. F. Hou, Y. L. Dong, Y. Chong, M. J. Cheng, W. S. Yang, *J. Power Sources* **2006**, *160*, 57-64.

[53]   Q. Zhu, T. Jin, Y. Wang, *Solid State Ionics* **2006**, *177*, 1199-1204.

[54]   A. Yan, M. Cheng, Y. L. Dong, W. S. Yang, V. Maragou, S. Q. Song, P. Tsiakaras, *Appl. Catal., B* **2006**, *66*, 64-71.

[55]   M. Arnold, H. H. Wang, A. Feldhoff, *J. Membr. Sci.* **2007**, *293*, 44-52.

[56]   L. Wang, PhD thesis, University of Stuttgart (Germany), **2009**.

[57]   F. A. Kroeger, *The Chemistry of Imperfect Crystals 2nd ed.*, North-Holland, Amsterdam, **1974**.

[58]   J. Mizusaki, T. Sasamoto, W. R. Cannon, H. K. Bowen, *J. Am. Ceram. Soc.* **1983**, *66*, 247-252.

[59]   L. W. Tai, M. M. Nasrallah, H. U. Anderson, D. M. Sparlin, S. R. Sehlin, *Solid State Ionics* **1995**, *76*, 259-271.

[60]   J. W. Stevenson, T. R. Armstrong, R. D. Carneim, L. R. Pederson, W. J. Weber, *J. Electrochem. Soc.* **1996**, *143*, 2722-2729.

[61]   M. V. Patrakeev, I. A. Leonidov, V. L. Kozhevnikov, V. Kharton, *Solid State Sci.* **2004**, *6*, 907-913.

[62]   B. Wei, Z. Lu, S. Y. Li, Y. Q. Liu, K. Y. Liu, W. H. Su, *Electrochem. Solid-State Lett.* **2005**, *8*, A428-A431.

[63]   J. Maier, *Solid State Ionics* **1998**, *112*, 197-228.

[64]   J. Fleig, J. Maier, *J. Eur. Ceram. Soc.* **2004**, *24*, 1343-1347.

[65]   R. Merkle, J. Maier, *Phys. Chem. Chem. Phys.* **2002**, *4*, 4140-4148.

[66]   J. A. Kilner, R. A. De Souza, I. C. Fullarton, *Solid State Ionics* **1996**, *86-88*, 703-709.

[67]   R. A. De Souza, J. A. Kilner, *Solid State Ionics* **1999**, *126*, 153-161.

[68]   L. Wang, R. Merkle, Y. A. Mastrikov, E. A. Kotomin, J. Maier, *J. Mater. Res.* **2012**, *27*, 2000-2008.

[69]   R. Merkle, J. Maier, H. J. M. Bouwmeester, *Angew. Chem., Int. Ed.* **2004**, *43*, 5069-5073.

[70]   Y. M. Choi, M. E. Lynch, M. C. Lin, M. L. Liu, *J. Phys. Chem. C* **2009**, *113*, 7290-7297.

[71]   Y. A. Mastrikov, R. Merkle, E. Heifets, E. A. Kotomin, J. Maier, *J. Phys. Chem. C* **2010**, *114*, 3017-3027.

[72]   F. S. Baumann, PhD thesis, University of Stuttgart (Germany), **2006**.

[73]   T. Ishigaki, S. Yamauchi, K. Kishio, J. Mizusaki, K. Fueki, *J. Solid State Chem.* **1988**, *73*, 179-187.

[74]   R. A. De Souza, J. A. Kilner, *Solid State Ionics* **1998**, *106*, 175-187.

[75]   R. Merkle, Y. A. Mastrikov, E. A. Kotomin, M. M. Kuklja, J. Maier, *J. Electrochem. Soc.* **2012**, *159*, B219-B226.

[76]   W. Preis, *Ber. Bunsen-Ges.* **1997**, *101*, 50-58.

[77]   R. Merkle, to be submitted.

[78]   W. Nernst, *Z. Phys. Chem., Stoechiom. Verwandtschaftsl.* **1888**, *2*, 613.

[79]   J. Maier, *Festkörper - Fehler und Funktion*, Teubner, Stuttgart, **2000**.

[80]   I. Riess, *Solid State Ionics* **1996**, *91*, 221-232.

[81]   J. B. MacChesney, J. J. Jetzt, J. F. Potter, H. J. Williams, R. C. Sherwood, *J. Am. Ceram. Soc.* **1966**, *49*, 644-647.

[82]   J.-F. Huang, X. Ni, J.-C. Bao, J.-H. Wu, *Chin. J. Struct. Chem.* **1994**, *13*, 350-359.

[83]   G. Catalan, J. F. Scott, *Adv. Mater.* **2009**, *21*, 2463-2485.

[84]   Y. Takeda, K. Kanno, T. Takada, O. Yamamoto, M. Takano, N. Nakayama, Y. Bando, *J. Solid State Chem.* **1986**, *63*, 237-249.

[85]   J. Mizusaki, M. Okayasu, S. Yamauchi, K. Fueki, *J. Solid State Chem.* **1992**, *99*, 166-172.

[86]   J. P. Hodges, S. Short, J. D. Jorgensen, X. Xiong, B. Dabrowski, S. M. Mini, C. W. Kimball, *J. Solid State Chem.* **2000**, *151*, 190-209.

[87]   M. Schmidt, S. J. Campbell, *J. Solid State Chem.* **2001**, *156*, 292-304.

[88]   K. Brinkman, T. Iijima, H. Takamura, *Solid State Ionics* **2010**, *181*, 53-58.

[89]   E. Folcke, J. M. Le Breton, Y. Breard, A. Maignan, *Solid State Sci.* **2010**, *12*, 1387-1392.

[90]   S. B. Adler, *Chem. Rev. (Washington, DC, U. S.)* **2004**, *104*, 4791-4843.

[91]   E. V. Tsipis, V. V. Kharton, *J. Solid State Electrochem.* **2008**, *12*, 1367-1391.

[92]   C. W. Sun, R. Hui, J. Roller, *J. Solid State Electrochem.* **2010**, *14*, 1125-1144.

[93]   S. P. Tolochko, I. F. Kononyuk, L. S. Ivashkevich, A. S. Lyakhov, *Inorg. Mater.* **1993**, *29*, 1375-1379.

[94]   C. S. Knee, F. Lindberg, N. Khan, G. Svensson, P. Svedlindh, H. Rundlof, S. G. Eriksson, L. Borjesson, *Chem. Mater.* **2006**, *18*, 1354-1364.

[95]   A. K. Eriksson, F. Lindberg, G. Svensson, P. Svedlindh, P. F. Henry, S. G. Eriksson, C. S. Knee, *J. Solid State Chem.* **2008**, *181*, 2031-2040.

[96]   Teijin Ltd., Jpn. Kokai Tokkyo Koho 812404, **1981**.

[97]   S. W. Li, C. You, L. Q. Fang, W. S. Yang, L. W. Lin, J. A. Meng, Y. F. Ren, *Mater. Res. Bull.* **1998**, *33*, 183-188.

[98]   Z. P. Shao, Y. Cong, G. X. Xiong, S. S. Sheng, W. S. Yang, *Sci. China, Ser. B: Chem.* **2000**, *43*, 421-427.

[99]   Z. P. Shao, G. X. Xiong, Y. Cong, W. S. Yang, *J. Membr. Sci.* **2000**, *164*, 167-176.

[100] Y. J. Niu, W. Zhou, J. Sunarso, L. Ge, Z. H. Zhu, Z. P. Shao, *J. Mater. Chem.* **2010**, *20*, 9619-9622.

[101] A. Wedig, R. Merkle, J. Maier, poster presented at the E-MRS Spring Meeting Symposium O (Strasbourg, France) **2010**, to be found under abstract 5-14, http://www.emrs-strasbourg.com.

[102] Y. J. Niu, J. Sunarso, F. L. Liang, W. Zhou, Z. H. Zhu, Z. P. Shao, *J. Electrochem. Soc.* **2011**, *158*, B132-B138.

[103] Y. J. Niu, J. Sunarso, W. Zhou, F. L. Liang, L. Ge, Z. H. Zhu, Z. P. Shao, *Int. J. Hydrogen Energy* **2011**, *36*, 3179-3186.

[104] L. A. Chick, L. R. Pederson, G. D. Maupin, J. L. Bates, L. E. Thomas, G. J. Exarhos, *Mater. Lett.* **1990**, *10*, 6-12.

[105] J. Fleig, *Solid State Ionics* **2002**, *150*, 181-193.

[106] M. C. Goebel, PhD thesis, University of Stuttgart (Germany), **2012**.

[107] M. E. Lynch, M. L. Liu, *J. Power Sources* **2010**, *195*, 5155-5166.

[108] M. E. Lynch, M. L. Liu, personal communication.

[109] R. Shannon, *Acta Crystallogr., Sect. A: Cryst. Phys., Diffr., Theor. Gen. Crystallogr.* **1976**, *32*, 751-767. The ionic radius of Bi^{3+} with dominant lone-pair character in 12-fold coordination was extrapolated from the ionic radius of the cation in 8-fold coordination, and the ionic radius of Bi^{3+} with constrained lone-pair character was calculated from the ionic radius of La^{3+} using the average cell volume ratio deduced from Table 3a in ref. [109].

[110] J. A. M. van Roosmalen, E. H. P. Cordfunke, *J. Solid State Chem.* **1991**, *93*, 212-219.

[111] H. J. M. Bouwmeester, *Catal. Today* **2003**, *82*, 141-150.

[112] D. Samuelis, A. Wedig, R. Merkle, J. Maier, to be submitted.

[113] F. Giannici, M. Shirpour, A. Longo, A. Martorana, R. Merkle, J. Maier, *Chem. Mater.* **2011**, *23*, 2994-3002.

[114] J. Li, Y. Duan, H. He, D. Song, *J. Alloys Compd.* **2001**, *315*, 259-264.

[115] G. King, P. M. Woodward, *J. Mater. Chem.* **2010**, *20*, 5785-5796.

[116] S. M. Selbach, M. A. Einarsrud, T. Grande, *Chem. Mater.* **2009**, *21*, 169-173.

[117] G. L. Yuan, S. W. Or, Y. P. Wang, Z. G. Liu, J. M. Liu, *Solid State Commun.* **2006**, *138*, 76-81.

[118] B. Bhushan, A. Basumallick, S. K. Bandopadhyay, N. Y. Vasanthacharya, D. Das, *J. Phys. D: Appl. Phys.* **2009**, *42*, 065004.

[119] T. Liu, Y. B. Xu, S. S. Feng, J. Y. Zhao, *J. Am. Ceram. Soc.* **2011**, *94*, 3060-3063.

[120] J. M. Tarascon, R. Ramesh, P. Barboux, M. S. Hedge, G. W. Hull, L. H. Greene, M. Giroud, Y. LePage, W. R. McKinnon, J. V. Waszcak, L. F. Schneemeyer, *Solid State Commun.* **1989**, *71*, 663-668.

[121] J. C. Grenier, S. Ghodbane, G. Demazeau, M. Pouchard, P. Hagenmuller, *Mater. Res. Bull.* **1979**, *14*, 831-839.

[122] G. Mayer-von Kuerthy, T. Fries, A. Ehmann, S. Loesch, M. Schlichenmaier, S. Kemmler-Sack, F. Badel, D. Koelle, R. P. Huebener, *J. Less-Common Met.* **1989**, *153*, L43-L48.

[123] A. Gualtieri, P. Norby, J. Hanson, J. Hriljac, *J. Appl. Crystallogr.* **1996**, *29*, 707-713.

[124] A. Hoffmann, *Naturwissenschaften* **1933**, *21*, 676.

[125] *National Bureau of Standards Monograph 25 - Section 18*, Washington, D.C., **1981**, p. 69.

[126] W. T. A. Harrison, S. L. Hegwood, A. J. Jacobson, *J. Chem. Soc., Chem. Commun.* **1995**, 1953-1954.

[127] A. K. Eriksson, S. G. Eriksson, L. C. Chapon, C. S. Knee, *Mater. Res. Bull.* **2010**, *45*, 1875-1882.

[128] V. M. Cherepanov, V. S. Pokatilov in *Solid State Phenomena, Vol. 152-153* (Ed.: N. Perov), Trans Tech, Staefa-Zuerich, **2009**, pp. 89-92.

[129] L. Wang, R. Merkle, G. Cristiani, B. Stuhlhofer, H.-U. Habermeier, J. Maier, *ECS Trans.* **2008**, *13*, 85-95.

[130] Y. M. Choi, M. C. Lin, M. L. Liu, *J. Power Sources* **2010**, *195*, 1441-1445.

[131] J. Mizusaki, M. Yoshihiro, S. Yamauchi, K. Fueki, *J. Solid State Chem.* **1987**, *67*, 1-8.

[132] M. C. Goebel, G. Gregori, X. X. Guo, J. Maier, *Phys. Chem. Chem. Phys.* **2010**, *12*, 14351-14361.

[133] V. V. Vashuk, L. V. Kokhanovskii, Yushkevich, II, *Inorg. Mater.* **2000**, *36*, 79-83.

[134] M. Pissas, G. Kallias, E. Moraitakis, D. Niarchos, A. Simopoulos, *Phys. C (Amsterdam, Neth.)* **1994**, *234*, 127-136.

[135] A. J. Jacobson, *Chem. Mater.* **2010**, *22*, 660-674.

[136] U. F. Vogt, P. Holtappels, J. Sfeir, J. Richter, S. Duval, D. Wiedenmann, A. Zuettel, *Fuel Cells (Weinheim, Ger.)* **2009**, *9*, 899-906.

[137] J. C. Waerenborgh, D. P. Rojas, A. L. Shaula, G. C. Mather, M. V. Patrakeev, V. V. Kharton, J. R. Frade, *Mater. Lett.* **2005**, *59*, 1644-1648. The mean TEC of $SrFe_{0.9}Al_{0.1}O_{3-\delta}$ is given corresponding to the weighted average of the values for the two different temperature regimes denoted in ref. [137].

[138] A. Feldhoff, J. Martynczuk, M. Arnold, M. Myndyk, I. Bergmann, V. Sepelak, W. Gruner, U. Vogt, A. Haehnel, J. Woltersdorf, *J. Solid State Chem.* **2009**, *182*, 2961-2971. The mean TEC of $Ba_{0.5}Sr_{0.5}Fe_{0.8}Zn_{0.2}O_{3-\delta}$ is given.

[139] C. L. Yaws, *Chemical Properties Handbook*, McGraw-Hill, New York, **1999**.

[140] H. Bea, M. Bibes, A. Barthelemy, K. Bouzehouane, E. Jacquet, A. Khodan, J. P. Contour, S. Fusil, F. Wyczisk, A. Forget, D. Lebeugle, D. Colson, M. Viret, *Appl. Phys. Lett.* **2005**, *87*, 072508.

[141] S. Havelia, S. Wang, M. Skowronski, P. A. Salvador, *J. Appl. Phys.* **2009**, *106*, 123509.

[142] E. I. Speranskaya, V. M. Skorikov, E. Y. Rode, V. A. Terekhova, *Bull. Acad. Sci. USSR, Div. Chem. Sci. (Engl. Transl.)* **1965**, *14*, 873-874.

[143] R. Palai, R. S. Katiyar, H. Schmid, P. Tissot, S. J. Clark, J. Robertson, S. A. T. Redfern, G. Catalan, J. F. Scott, *Phys. Rev. B: Condens. Matter Mater. Phys.* **2008**, *77*, 014110.

[144] H. Z. Zhang, H. Y. Liu, Y. Cong, W. S. Yang, *J. Power Sources* **2008**, *185*, 129-135.

[145] D. J. Chen, C. Huang, R. Ran, H. J. Park, C. Kwak, Z. P. Shao, *Electrochem. Commun.* **2011**, *13*, 197-199.

[146] D. J. Chen, F. C. Wang, Z. P. Shao, *Int. J. Hydrogen Energy* **2012**, *37*, 11946-11954.

[147] L. Wang, R. Merkle, J. Maier, T. Acartuerk, U. Starke, *Appl. Phys. Lett.* **2009**, *94*, 071908.

[148] N. G. Schmahl, G. F. Eikerling, *Z. Phys. Chem. (Muenchen, Ger.)* **1968**, *62*, 268-279.

[149] P. Plonczak, A. Bieberle-Huetter, M. Sogaard, T. Ryll, J. Martynczuk, P. V. Hendriksen, L. J. Gauckler, *Adv. Funct. Mater.* **2011**, *21*, 2764-2775.

[150] L. Vattuone, L. Savio, M. Rocca, *Surf. Sci. Rep.* **2008**, *63*, 101-168.

[151] K. Balamurugan, N. H. Kumar, P. N. Santhosh, *J. Appl. Phys.* **2009**, *105*, 07D909.

[152] I. O. Troyanchuk, O. S. Mantytskaya, A. N. Chobot, N. V. Tereshko, *Phys. Solid State* **2009**, *51*, 2105-2108.

[153]   P. Singh, Y. A. Park, K. D. Sung, N. Hur, J. H. Jung, W. S. Noh, J. Y. Kim, J. Yoon, Y. Jo, *Solid State Commun.* **2010**, *150*, 431-434.

[154]   S. P. Simner, M. D. Anderson, M. H. Engelhard, J. W. Stevenson, *Electrochem. Solid-State Lett.* **2006**, *9*, A478-A481.

[155]   M. Backhaus-Ricoult, *Solid State Sci.* **2008**, *10*, 670-688.

[156]   T. Horita, H. Kishimoto, K. Yamaji, M. E. Brito, Y. P. Xiong, H. Yokokawa, Y. Hori, I. Miyachi, *J. Power Sources* **2009**, *193*, 194-198.

[157]   E. Bucher, W. Sitte, F. Klauser, E. Bertel, *Solid State Ionics* **2012**, *208*, 43-51.

[158]   J. Jamnik, J. Maier, *Phys. Chem. Chem. Phys.* **2001**, *3*, 1668-1678.

[159]   W. Jung, H. L. Tuller, *J. Electrochem. Soc.* **2008**, *155*, B1194-B1201.

[160]   F. L. Jones, *The Physics of Electrical Contacts*, Clarendon, Oxford, **1957**.

[161]   J. H. Joo, R. Merkle, J. Maier, *J. Power Sources* **2011**, *196*, 7495-7499.

[162]   A. Wedig, unpublished work.

[163]   A. K. Opitz, J. Fleig, *Solid State Ionics* **2010**, *181*, 684-693.

[164]   J. Fleig, *Phys. Chem. Chem. Phys.* **2005**, *7*, 2027-2037.

[165]   I. Kosacki, H. U. Anderson, Y. Mizutani, K. Ukai, *Solid State Ionics* **2002**, *152*, 431-438.

[166]   J. Maier, *Z. Phys. Chem. (Muenchen, Ger.)* **1984**, *140*, 191-215.

[167]   B. A. Boukamp, *Introduction to Impedance Spectroscopy*, workshop held at the 18th International Conference on Solid State Ionics (Warsaw, Poland) **2011**.

[168]   J. Yoo, A. Verma, S. Y. Wang, A. J. Jacobson, *J. Electrochem. Soc.* **2005**, *152*, A497-A505.

[169]   R. Merkle, personal communication.

[170]   A. Rothschild, W. Menesklou, H. L. Tuller, E. Ivers-Tiffee, *Chem. Mater.* **2006**, *18*, 3651-3659.

[171]   S. Diethelm, A. Closset, J. van Herle, K. Nisancioglu, *Electrochemistry* **2000**, *68*, 444-450.

[172]   J. Mizusaki, Y. Yonemura, H. Kamata, K. Ohyama, N. Mori, H. Takai, H. Tagawa, M. Dokiya, K. Naraya, T. Sasamoto, H. Inaba, T. Hashimoto, *Solid State Ionics* **2000**, *132*, 167-180.

[173]   J. Mizusaki, J. Tabuchi, T. Matsuura, S. Yamauchi, K. Fueki, *J. Electrochem. Soc.* **1989**, *136*, 2082-2088.

[174]   E. V. Bongio, H. Black, F. C. Raszewski, D. Edwards, C. J. McConville, V. R. W. Amarakoon, *J. Electroceram.* **2005**, *14*, 193-198.

[175]   Z. H. Chen, R. Ran, W. Zhou, Z. P. Shao, S. M. Liu, *Electrochim. Acta* **2007**, *52*, 7343-7351.

Curriculum Vitae

Name:	Anja Wedig
Date of Birth:	November 6th, 1982
Place of Birth:	Stuttgart
Nationality:	German

02/2009 – today **PhD in Solid State Physical Chemistry**

Max Planck Institute for Solid State Research, Stuttgart

Supervisor: Prof. Dr. Joachim Maier

Title of the PhD Thesis: "Oxygen Exchange Kinetics of the Potential Solid Oxide Fuel Cell Cathode Material $(Bi,Sr)(Co,Fe)O_{3-\delta}$"

10/2003 – 12/2008 **Studies in Chemistry**

University of Stuttgart and Institute of Researches on Catalysis and Environment – CNRS, Lyon, France (03/2007 – 08/2007)

Leaving Certificate: Diplom

Title of the Diploma Thesis: "Untersuchung der Zeitabhängigkeit der Protonenleitfähigkeit einer Nafion-Brennstoffzellenmembran mittels elektrochemischer AFM"

10/2002 – 08/2003 **European Voluntary Service**

Moscow, Russia

08/1993 – 07/2002 **Secondary School**

St.-Agnes-Gymnasium, Stuttgart

Leaving Certificate: Abitur

Erklärung über die Eigenständigkeit der Dissertation

Ich versichere, dass ich die vorliegende Arbeit mit dem Titel „Oxygen Exchange Kinetics of the Potential Solid Oxide Fuel Cell Cathode Material (Bi,Sr)(Co,Fe)O$_{3-\delta}$" selbständig verfasst und keine anderen als die angegebenen Quellen und Hilfsmittel benutzt habe; aus fremden Quellen entnommene Passagen und Gedanken sind als solche kenntlich gemacht.

Stuttgart, den 9. April 2013   Anja Wedig

Declaration of Authorship

I hereby certify that the dissertation entitled "Oxygen Exchange Kinetics of the Potential Solid Oxide Fuel Cell Cathode Material (Bi,Sr)(Co,Fe)O$_{3-\delta}$" is entirely my own work except where otherwise indicated. Passages and ideas from other sources have been clearly indicated.

Stuttgart, April 9th, 2013   Anja Wedig